COMPUTATIONAL MODELING OF PHASE FRONTS, FREE SURFACES AND CONVECTIVE HEAT TRANSFER DURING SOLIDIFICATION PROCESSING

By

MADHUKAR M. RAO

A DISSERTATION PRESENTED TO THE GRADUATE SCHOOL
OF THE UNIVERSITY OF FLORIDA IN PARTIAL FULFILLMENT
OF THE REQUIREMENTS FOR THE DEGREE OF
DOCTOR OF PHILOSOPHY

UNIVERSITY OF FLORIDA

1996

ACKNOWLEDGEMENTS

I can only try to express my heartfelt thanks to Prof. Shyy for his guidance and friendship throughout the course of my graduate study. Without his help and patient guidance this work would not have been possible. His hard work and persistence have been a great source of inspiration to me.

I thank the other members of my committee, Dr. Fearn, Dr. Kurzweg, Dr. Lindgren and Dr. Goswami for their guidance and help during the course of this work.

I thank Dr.–Ing. T. K. Bose of IIT–Madras for initiating me into the science and art of computational aerodynamics and Mr. S. C. Rajan of IIT–Madras for his memorable lectures that attracted me to fluid dynamics.

To my colleagues and fellow researchers in the CFD group, Dr. Siddarth "ST" Thakur, Dr. Jeff Wright, Dr. Rick Smith, Dr. H. S. Udaykumar, Dr. Edwin Blosch, Jian "James" Liu, Venkat Krishnamurthy and Hong Ouyang, I express my heartfelt thanks for the memorable times and the many useful discussions and collaborative work that we have shared during the course of our graduate study.

Some of the computations carried out in this work were supported by a grant of computer time from the research computing initiative, NERDC, University of Florida and were done on their IBM SP2 cluster. Partial financial support from GE and AFOSR URI are gratefully acknowledged.

Special thanks are due to my wife, Vijayasri, for her encouragement and support that greatly assisted my studies in the last two years. My sister, Madhuri, has been a constant and lively source of encouragement and support which has made my life all the richer. I owe a special debt of gratitude to my parents which can never be fully repaid. Without their efforts and the emphasis that they placed on a good education, I would never have amounted to anything. To them, I dedicate this thesis.

TABLE OF CONTENTS

page

ACKNOWLEDGEMENTS ii

TABLE OF CONTENTS iii

ABSTRACT vi

CHAPTERS

1 INTRODUCTION 1
- 1.1 Motivation 1
- 1.2 Computational Methodology 2
- 1.3 Float Zone Crystal Growth 4

2 FORMULATION FOR CONVECTIVE HEAT TRANSFER AND FREE SURFACE FORMATION 9
- 2.1 Background 9
- 2.2 Sources of Convection 10
  - 2.2.1 Natural Convection 10
  - 2.2.2 Marangoni Convection 11
- 2.3 Nondimensionalization and Scaling Procedure 12
  - 2.3.1 Heat Conduction Scales 12
  - 2.3.2 Natural Convection Scales 12
  - 2.3.3 The Marangoni Number 13
  - 2.3.4 Marangoni Convection Scales 13
- 2.4 Governing Equations and Solution Procedure 14
- 2.5 Formulation and Methodology for Free Surface Computation 16
- 2.6 Results and Discussion 21
  - 2.6.1 Low Bond Number 21
  - 2.6.2 High Bond Number 28
  - 2.6.3 Determination of Pressurization Values 29
  - 2.6.4 Solutions for Aspect Ratio of Unity 31

2.7 Concluding Remarks 33

3 CONVECTIVE HEAT TRANSFER COMPUTATIONS 35

3.1 Background 35

3.2 Convection Treatment and Accuracy Assessment 35

3.2.1 Results and Discussion 39

3.3 Transient Natural Convection in an Enclosure 42

3.3.1 Formulation and Solution Procedure 49

3.3.2 Results and Discussion 52

3.4 Steady Thermocapillary Convection in a Liquid Bridge 63

3.4.1 Scaling, Nondimensionalization and Governing Equations 64

3.4.2 Heat Transfer Calculations 67

3.4.3 Numerical Procedure 67

3.4.4 Heat Conduction 69

3.4.5 Natural Convection 69

3.4.6 Interaction of Natural and Thermocapillary Convection 70

3.5 Effect of Convection on Meniscus Shape 77

3.6 Concluding Remarks 80

4 ENTHALPY BASED PHASE CHANGE MODELING 81

4.1 Background 81

4.2 Heat Conduction 82

4.3 Numerical Implementation 85

4.3.1 The T–Based Method 85

4.3.2 The H–Based Method 87

4.4 Results and Discussion 87

4.4.1 Accuracy Assessment 87

4.4.2 Performance Assessment 89

4.4.3 Summary 90

4.5 Convective Effects 95

4.5.1 Governing Equations 95

4.5.2 Source Terms in the Momentum Equations 96

4.5.3 Sources of Convection 97

4.5.4 Computational Procedure 98

4.6 Effect of Gravity Jitter 99

4.7 Float Zone Growth of NiAl 101

4.7.1 Calculation Procedure 104

4.7.2 Results and Discussion 107

4.7.3 Heat Conduction 108
4.7.4 Thermocapillary Convection 108
4.8 Concluding Remarks 112

5 MOVING BOUNDARY COMPUTATION OF FREE SURFACE FLOW AND SOLIDIFICATION IN FLOAT ZONE PROCESSING 115
5.1 Introduction 115
5.2 Governing Equations and Boundary Conditions 115
5.2.2.1 Thermal Boundary Conditions 117
5.2.2.2 Free Surface Treatment 117
5.2.2.3 Symmetry 118
5.3 Moving Grid Transformation 120
5.4 Computational Methodology 122
5.4.2.1 Convergence Criteria 128
5.4.2.2 Global Mass Conservation 128
5.4.2.3 Root Finding Procedure 129
5.4.2.4 Remeshing Procedure 129
5.5 Results and Discussion 131
5.5.3.1 Estimation of Meniscus Shape and P_L 133
5.5.3.2 Conduction–Capillarity Solution 135
5.6 Grid Refinement Study and Assessment 137
5.7 Thermocapillary Convection 149
5.7.1.1 Cylindrical meniscus 150
5.7.1.2 Deformed meniscus 151
5.7.1.4 Cylindrical meniscus 154
5.7.1.5 Deformed meniscus 156
5.8 Conclusion 159

6 CONCLUSION 164
6.1 Summary and Conclusions 164
6.2 Future Work 166
6.2.1 Node Jumping 166
6.2.2 Multi–Block Approach 167
6.2.3 Feed/Crystal Rotation 167
6.2.4 Dopant Transport 167
6.2.5 Electromagnetic Heating 167

REFERENCES 169

BIOGRAPHICAL SKETCH 177

Abstract of Dissertation Presented to the Graduate School
of the University of Florida in Partial Fulfillment of the
Requirements for the Degree of Doctor of Philosophy

COMPUTATIONAL MODELING OF PHASE FRONTS, FREE SURFACES AND CONVECTIVE HEAT TRANSFER DURING SOLIDIFICATION PROCESSING

By

Madhukar M. Rao

May 1996

Chairperson : Dr. Wei Shyy
Major Department : Aerospace Engineering, Mechanics and Engineering Science

A methodology has been developed to simulate fluid flow, heat transfer, free surface, and phase change dynamics in the context of solidification processing. Special attention has been given to float zone processing of single crystals due to its increasing technological importance in growing high quality single crystals and due to the complex physical phenomena involved – free surface flow, thermocapillary and buoyancy driven convection, phase change and the nonlinear coupling amongst these physical phenomena. The SIMPLE algorithm in body fitted coordinates has been chosen for fluid flow and heat transfer computations. Issues of accuracy and implementation of convection schemes have been addressed in the context of buoyancy driven convection. Accurate simulations of transient natural convection around an enclosed vertical channel have been conducted since it is an important heat transfer mechanism in solidification as well as a host of other applications such as electronics cooling. The issues of existence, multiplicity and non–uniqueness of float zone menisci have been dealt with in the context of a free energy minimization principle.

Steady, thermocapillary convection has been simulated in a liquid bridge which yields useful information on heat transfer characteristics in a float zone configuration. Both single phase flows and flows with phase change have been computed in this study. Alternative formulations of enthalpy porosity models have been developed and assessed for the computation of phase change dynamics in the presence of melt convection. These methods have been applied to compute and assess the impact of interacting natural and thermocapillary convection on solid–liquid interfaces during float zone growth. A moving boundary algorithm has been developed to simulate the nonlinear coupling between the unknown shape and location of the free surface, the unknown shape and location of the solid–liquid interfaces, and the convective heat transfer processes in the float zone. This computational model has also been applied to assess the impact of both, normal gravity as well as microgravity conditions, on the dynamics within the float zone. It has been found that whereas buoyancy induced convection is negligible under microgravity conditions, significant levels of thermocapillary convection exist and have a profound impact on the solid–liquid interface morphology at the macroscopic scales. It has also been found that under normal gravity conditions, the counteracting effect of natural and thermocapillary convection can actually result in reduced convection strength in the lower half of the zone and lead to a flatter solid–liquid interface shape. The calculation procedures developed in this study constitute a predictive capability for float zone single crystal growth.

CHAPTER 1
INTRODUCTION

1.1 Motivation

The goal of this research is to develop and employ computational tools to model phase change and convective heat transfer in materials processing applications. Special emphasis is placed on problems dealing with solidification and crystal growth. Typical applications include growth of optical and semiconductor crystals from the melt as well as intermetallics for high temperature structural applications. Solidification phenomena occurring during materials processing are dominated by convective heat and mass transport in the melt, and more importantly, are characterized by the presence of one or more moving interfaces constituting moving boundaries. These interfaces are discontinuities separating different flow regions; they may be phase change interfaces such as those between the melt and the solid or they may be free surfaces separating the melt and the ambient liquid or gas. The nonlinear coupling between these different phenomena is the major source of modeling and computational difficulties.

Modeling of fluid flow and heat transfer is a matter of particular interest in this study. These transport processes control the quality of the grown crystal or solidified product (Brown 1988, Huppert 1990, Davis 1990). For example, high thermal gradients in the growing crystal can lead to large thermoelastic stresses that can cause cracking or fracture (Viskanta 1990). Solute rejection at the growing interface can lead to constitutional undercooling giving rise to morphological instabilities of the interface (Mullins and Sekerka 1964, Glicksman et al. 1986).

1.2 Computational Methodology

Fluid convection can arise in solidification systems due to a variety of factors. Density differences in the melt caused by thermal and compositional inhomogeneities give rise to buoyancy induced convection (Langlois 1985). Marangoni convection arises out of shear stress induced by thermal and composition gradients along free surfaces. Density differences between the melt and the solid can also be an important source of convection depending on the growth configuration. In addition, forced convection can be present due to crystal and/or crucible rotation which is usually done in order to even out azimuthal inhomogeneities in the melt temperature and composition (Langlois 1985, Hurle 1993).

In this work, attention is focused on thermally induced buoyancy driven and thermocapillary convection, both, with and without the presence of phase change. Whereas a major interest is in problems dealing with crystal growth, natural and thermocapillary convection without phase change have been considered as a natural starting point to develop and assemble the necessary computational capabilities. The SIMPLE algorithm for incompressible flow computation (Patankar 1980) extended to treat complex geometry by using a body fitted coordinate system (Shyy 1994) is chosen as the underlying computational technique. It is a robust and proven method, and the sequential solution technique built into the method enables additional physics to be incorporated without the need for substantial modification to the algorithm. Thus, the computational technique can be extended in stages that include more complex physical phenomena which increases the level of confidence in the computational technique.

As a starting point and to develop the necessary numerical techniques, problems involving natural and thermocapillary convection, but without phase change, have been investigated. The SIMPLE algorithm has been implemented and tested against an available benchmark solution for natural convection of air in a square cavity. In chapter 3, this problem is also used to characterize the relative accuracy of various convection schemes such as the second order central difference scheme, the second order upwind scheme etc. for the momentum and energy equations. The computational technique has also been extended to handle the unsteady terms in the Navier–Stokes equations. The computational technique is then applied to model transient natural convection and heat transfer in a configuration used for electronics cooling. Chapter 3 also describes the extension of the computational procedure to simulate steady thermocapillary convection in a liquid bridge of molten NiAl – an intermetallic that is being considered for high temperature structural application in future generation of aircraft engines and other aerospace applications. The model is based on a float zone configuration currently in use for growing single crystals of NiAl.

In chapter 4, the computational technique is further extended to model phase change and solidification processes. The enthalpy method (Crank 1984, Shyy 1994, Shyy et. al. 1995) is particularly suitable for modeling phase change processes at macroscopic scales and is chosen for conducting the solidification simulations. The advantage of the enthalpy method is that it is a fixed grid technique which obviates the need for a moving grid and explicit interface tracking. However, the volume averaging procedure that is implicit in this technique smears out the interface information over a thin mushy zone implying that curvature dependent phenomena and interface microstructure cannot be captured. A one-dimensional heat conduction problem (Stefan problem) is chosen as the test bed to develop a particularly efficient implementation of the enthalpy method and to characterize its accuracy and performance. The enthalpy method is also applied to a two dimensional melting problem dominated by natural convection heat transfer and highly nonlinear interfacial dynamics. Qualitative agreement of the computed interface shapes with experimental data is established.

The enthalpy method is then applied to simulate practical crystal growth configurations. The float zone model considered in chapter 3 is extended, in chapter 4, to take into account the nonlinear coupling of interacting natural and thermocapillary convection with the melt/crystal and melt/feed interfaces. However, the free surface is held stationary in this study in order to clearly isolate the interaction of convection heat transfer and phase change dynamics. This restriction is removed in the studies taken up in Chapter 5.

1.3 Float Zone Crystal Growth

The rest of this work deals with the extension of the computational techniques developed, to compute the unknown shape and location of the free surface coupled with phase change and convective heat transfer. The float zone growth technique is taken as the prototype application. The float zone process consists of the growing crystal and the feed separated by a liquid bridge of the molten material as shown in Fig. 1.1. An adequate simulation involves consideration of the nonlinear coupling of the melt/crystal and feed/crystal interfaces, the shape and motion of the free surface (meniscus) between the melt and ambient gas or encapsulant, thermocapillary and buoyancy driven convection in the melt. In order to build an effective simulation capability, a moving grid technique similar to the one developed in Shyy et. al. (1995) is developed to track the motion of the free surface. The shape and location of the free surface are determined by integrating the dynamic

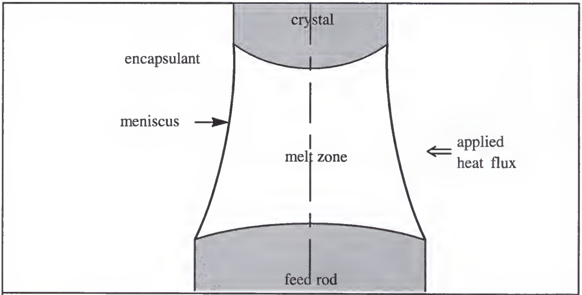

Figure 1.1. Schematic of the float zone process. The melt zone is sustained by the surface tension between the melt and the encapsulant. The heating profile is schematically illustrated in the right.

form of the Young–Laplace equation. The Young–Laplace equation describes the balance between the surface tension force and the pressure difference across the free surface.

The float zone technique is one of the candidate methods for growing single crystals. The main advantage of the float zone process is that it is a containerless process and thus one main source of contamination is removed. Another advantage is the reduction of thermal stresses which are caused by differential thermal expansion between the crystal and the crucible. On earth, it is mainly limited by the size of the melt zone that can be achieved, since the hydrostatic pressure of the melt zone is balanced by the surface tension between the melt and the ambient fluid. Another problem is the loss of volatile components from the melt, which can be circumvented by the use of encapsulating fluids. Liquid encapsulants can also increase the maximum size of the melt zone that can be achieved. The formation of the meniscus during the melting process is a major concern in the successful operation of the float zone technique and this aspect will be examined in detail in chapter 2.

Float zone simulations have been carried out by many researchers at different levels of complexity. Kobayashi (1984) computed thermocapillary convection under zero gravity conditions for two different Prandtl numbers, with and without crystal rotation while neglecting the deformation of the free surface. Kobayashi (1988) extended the study to include buoyancy induced convection. Young (1990) has presented asymptotic solutions for the temperature, concentration, and interface shapes in the limit of small aspect ratio and weak surface tension for a two dimensional float zone established in a vertical sheet. Neitzel et. al. (1990) have computed thermocapillary convection in a float zone with a computed free surface shape. Chen et. al. (1994) have carried out numerical simulation for low and high Prandtl number fluids to study melt convection and the power input required to form a molten zone. However, they have constrained the free surface to a cylindrical shape and have not considered the effect of free surface deformation and curvature. Chu and Chen (1995) have obtained numerical solutions for float zone growth of Molybdenum (Mo) crystals with an imposed heat input profile rather than an imposed temperature profile. Again, they imposed the constraint of a fixed cylindrical free surface and concentrated their efforts on the details of the flow structure. Duranceau and Brown (1986) developed a steady–state, thermal–capillary model where the free surface was computed as part of the solution. However, their model considered only heat conduction but not melt convection. Lan and Kou (1990a, 1990b) have carried out coupled calculations of steady thermocapillary flow and natural convection under normal and microgravity conditions for an $NaNO_3$ float zone. However, they too confined their calculations to an imposed cylindrical shape of the free surface.

Duranceau and Brown (1986) developed a steady–state, thermal–capillary model where the free surface was computed as part of the solution. However, their model considered only heat conduction but not melt convection. Lan and Kou (1991a, 1991b, 1992a) carried out computations of float zone growth of $NaNO_3$ crystals where the heater was in physical contact with the melt. Their intention was to grow crystals of uniform cross–section and improved surface smoothness as well as melt zone stability at the cost of increased risk of melt contamination. This arrangement prevented the deformation of the free surface and suppressed thermocapillary convection to a large extent. They also considered cases where the melt was partially exposed to the ambient gas thus permitting weak thermocapillary convection but not free surface deformation.

Lan and Kou (1991c, 1992b) have also carried out a series of studies on float zones with rotation and counterrotation of the feed and crystal. The have found that due to the resulting melt rotation the height of the zone can be reduced significantly by reducing the power input. The forced convection in the melt due to rotation helps to prevent freezing of the melt at the centerline. This is especially useful for non–electrically conducting materials such as $NaNO_3$ since electromagnetic levitation forces cannot be used to stabilize the zone.

Chan and Choi (1992) and Chan (1995) have modeled the convective heat transfer, solidification and free surface deformation during float zone growth of Titanium Carbide (TiC) by induction heating. Mühlbauer et. al. (1995) have simulated the growth of large

Silicon crystals by the needle–eye technique with the unknown interface shapes determined as a coupled thermal-electromagnetic-hydrodynamic problem. For their problem, buoyancy induced convection and forced convection due to crystal rotation dominated thermocapillary convection in the float zone. The effect of dopant segregation in float zone growth of KNO_3 doped $NaNO_3$ crystals has been considered by Lan and Kou (1993a) at zero gravity. Also, in a related work, Lan and Kou (1993b) have examined dopant segregation under microgravity and with crystal rotation. In these studies, both negative and positive segregation coefficients have been considered. The have found that the shape of the melt/crystal interface is significantly affected by the radial dopant segregation, especially at the centerline. Also, with increasing strength of thermocapillary convection, the segregation decreases. A similar result was obtained with fast counterrotation of the crystal. Lan (1994) computed steady, convective heat transfer and interface shapes in a float zone using Newton's iterations. This study employed a mass conservation scheme to determine the free surface shape as opposed to a fixed contact angle condition.

Transient computations of g–jitter induced convection in a Bismuth Silicate (BSO) float zone have been studied by Chen et. al. (1994). However, they constrained the free surface to a nondeformable cylindrical shape and imposed a fixed, parabolic temperature distribution on the free surface and did not consider phase change/solidification effects. Grugel et. al. (1994) have carried out experimental investigations of vibration on the solidification characteristics in a $NaNO_3$ float zone. They found that vibration suppressed thermocapillary convection resulting in flatter interfaces as evidenced by the improved uniformity of the microstructural morphology presumably due to the opposing effects of thermocapillary and buoyancy driven convection set up the by effect of body forces due to vibration. Hu et. al. (1994) have carried out experiments on the onset of oscillatory thermocapillary flow in a half zone to determine the relationship between the liquid bridge volume and the critical Marangoni number measured in terms of the critical temperature difference. Tang and Hu (1994) carried out corresponding numerical simulations on a two dimensional half zone. Lee et. al. (1995) have performed experiments to investigate oscillatory thermocapillary flow. They found that three dimensional oscillatory flow appears when the Marangoni number exceeds a critical value. The flow modes were found to be strongly dependent on the aspect ratio rather than on the Marangoni number. The flow oscillations, thermal oscillations and the free surface deformations had the same frequencies. Yeckel et. al. (1995) have simulated heat and momentum transport in the vertical float zone refinement of two dimensional silicon sheets. They found that thermocapillary convection dominates over buoyancy driven flow and the solid–liquid interfaces depart considerably from a planar shape. Levenstam et. al. (1996) have carried out experimental and theoretical studies to determine the critical Reynolds number for transition to oscillatory flow in a silicon float zone. They found that as the Reynolds number increases, the flow transitions from a steady two dimensional state to a three dimensional state and then to an unsteady flow.

Thus, many researchers have worked towards the goal of float zone simulations with varying degrees of numerical sophistication, physical complexity and simplifications regarding the free surface shape etc. The simulation capability developed in this work aims at a more complete level of modeling capability. A combination of higher grid resolution, second order convection schemes, strict convergence criteria, and moving grid capability are used in conjunction with the robust SIMPLE algorithm and the enthalpy formulation to faithfully simulate this complex process.

CHAPTER 2
FORMULATION FOR CONVECTIVE HEAT TRANSFER AND FREE SURFACE FORMATION

2.1 Background

In this chapter, a formulation is developed for convection heat transfer and free surface formation in float zones. Of particular interest is natural convection generated by density differences in the fluid, and thermocapillary convection caused by shear stress arising from thermal and composition gradients along a free surface separating a liquid and a gas. The interest in such flows arises from its prevalence in nature as well as in engineering applications and devices. For instance, natural convection is one of the important and commonly employed method to cool electronic devices. Thermocapillary convection becomes important in many crystal growth and solidification processes, notably, the float zone process for single crystal growth from the melt. The chapter starts with a description of the physical scales that characterize natural and thermocapillary convection, illustrating the nondimensional parameters that determine the strength and relative importance of these physical processes. Then the governing equations are transformed into a body–fitted coordinate system which is convenient for handling curved and complex geometry. In this work, the governing equations are solved by means of the popular and robust SIMPLE algorithm for incompressible flows. For convection dominated flows, the numerical treatment of the convection terms in the Navier–Stokes equations has a substantial impact on the robustness and accuracy as will be demonstrated in the next chapter. This chapter concludes with a formulation for the generation of meniscus shape for float zone configurations. The issues of existence, multiplicity and sensitivity of free surface shapes are discussed in the context of solutions to the Young–Laplace equations and a free energy concept originated by Shyy et. al. (1993).

2.2 Sources of Convection

2.2.1 Natural Convection

The strength of natural convection depends on the density differences caused by thermal and compositional inhomogeneities within the fluid. In two–dimensions, the source of buoyancy driven convection is the component of the local density gradient normal to the gravity vector. A temperature scale, ΔT, can be defined which, along with a characteristic length scale, d, characterizes the horizontal thermal gradient and consequently the horizontal density gradient. In addition, we can define a characteristic solute scale, $\Delta\phi$. The Boussinesq approximation is now invoked, which by linearization neglects the density variation in all the terms of the governing equations except the source term. The buoyancy source term then becomes

$$-\left(\varrho - \varrho_{ref}\right) g = \varrho\, g \left[\, \beta_T \left(T - T_{ref}\right) + \beta_\phi \left(\phi - \phi_{ref}\right)\right] \tag{2.1}$$

where β_T and β_ϕ are the coefficients of thermal expansion and solutal expansion, respectively, of the melt. The resulting nondimensional parameters are

Thermal Grashof number: $$Gr_T = \frac{g\, \beta_T\, \Delta T\, d^3}{\nu^2} \tag{2.2a}$$

Solutal Grashof number: $$Gr_\phi = \frac{g\, \beta_\phi\, \Delta\phi\, d^3}{\nu^2} \tag{2.2b}$$

Prandtl number: $$Pr = \frac{\mu}{k/C_p} \tag{2.2c}$$

Schmidt number: $$Sc = \frac{\nu}{D} \tag{2.2d}$$

where k is the thermal conductivity, ϱ is the density, C_p is the heat capacity, μ is the dynamic viscosity, ν is kinematic viscosity, and D is the mass diffusivity. The thermal and the solutal Rayleigh numbers can be defined as $Ra_T = Gr_T \cdot Pr$ and $Ra_\phi = Gr_\phi \cdot Sc$, respectively.

2.2.2 Marangoni Convection

For problems involving free or deformable interfaces between two liquids or between a liquid and a gas/vapor, temperature and composition inhomogeneities can result in a surface tension gradient along the interface. This exerts a shear stress on the fluid giving rise to thermocapillary convection also known as Marangoni convection. The float zone is an example of a configuration where Marangoni convection plays an important role in governing the solidification characteristics of the melt. General discussion of Marangoni convection can be found in Koschmieder (1993), Shyy (1994). We now briefly examine the case of thermally generated Marangoni convection.

For liquids bounded by a free or deformable boundary where a temperature gradient exists along the interface, a surface shear stress is generated by the surface tension gradient. Thus, the force balance can be written as

$$\mu \cdot \nabla\, (\vec{V} \cdot \vec{t}) \cdot \vec{n} = \frac{\partial \gamma}{\partial T}\, \nabla T \cdot \vec{t} \tag{2.3}$$

where the surface tension gradient is proportional to the temperature gradient and gives rise to the normal derivative of the tangential velocity at the free surface. γ is the surface tension, $\vec{V}$ is the velocity vector, $\vec{n}$ is the unit normal vector to the free surface, and $\vec{t}$ is the unit tangent vector to the free surface. The convection strength is described, in nondimensional terms, by the Marangoni number,

$$\mathrm{Ma} = \left|\frac{d\gamma}{dT}\right| \frac{\Delta T\, d}{\mu\, \alpha} \tag{2.4}$$

where α is the thermal diffusivity. The Marangoni number represents the balance between the shear stress and the surface tension gradient after the velocity and space variables have been nondimensionalized by the velocity scale based on heat conduction, as will be described in the next section.

2.3 Nondimensionalization and Scaling Procedure

The governing equations can be nondimensionalized with reference length, velocity and thermal scales. The choice of nondimensional parameters used to normalize the governing equations is not unique as will be apparent in the following.

The dimensionless variables can be defined as:

$$\begin{aligned} &\tau = t/t_r\ ,\ X = x/d\ ,\ Y = y/d \\ &\tilde{u} = u/U_r\ ,\ \tilde{v} = v/U_r \\ &P = p/(\varrho U_r^2) \text{ and } \Theta = (T - T_c)/(T_h - T_c) \end{aligned} \tag{2.5}$$

In equation (2.5), d is the reference length scale, U_r is the reference velocity scale, T_h and T_c are the maximum and minimum temperatures present in system, and the temperature is normalized by the reference temperature scale, $\Delta T = T_h - T_c$, such that the nondimensional temperature is between zero and unity. The reference time scale is defined as $t_r = d/U_r$. The reference velocity scale is determined by the dominant physical processes occurring in the system as described next.

2.3.1 Heat Conduction Scales

The reference velocity scale for heat conduction is

$$U_r = \frac{\alpha}{d} \tag{2.6}$$

where $\alpha = k/(\varrho C_p)$ is the thermal diffusivity of the fluid. Then, with the reference scales specified earlier, the non-dimensional equations become:

momentum: $$\frac{\partial \vec{V}}{\partial \tau} + \vec{V} \cdot \nabla(\vec{V}) = -\nabla P + \Pr \nabla^2 \vec{V} - \mathrm{Ra} \Pr \Theta \hat{g} \tag{2.7a}$$

energy: $$\frac{\partial \Theta}{\partial \tau} + \vec{V} \cdot \nabla \Theta = \nabla^2 \Theta \tag{2.7b}$$

where $\vec{V}$ is the nondimensional velocity vector, Pr is the Prandtl number, $\hat{g}$ is the unit vector in the direction of gravity, and Ra is the thermal Rayleigh number.

2.3.2 Natural Convection Scales

The reference velocity scale for natural convection is

$$U_r = \sqrt{g\ \beta\ d\ \Delta T} \tag{2.8}$$

and with the reference scales specified earlier, the nondimensional equations become

momentum: $$\frac{\partial \vec{V}}{\partial \tau} + \vec{V} \cdot \nabla(\vec{V}) = -\nabla P + \frac{1}{\sqrt{Gr_T}} \nabla^2 \vec{V} - \Theta \hat{g} \tag{2.9a}$$

energy: $$\frac{\partial \Theta}{\partial \tau} + \vec{V} \cdot \nabla \Theta = \frac{1}{Pr\sqrt{Gr_T}}\ \nabla^2 \Theta \tag{2.9b}$$

where Pr is the Prandtl number and Gr_T is the thermal Grashof number.

2.3.3 The Marangoni Number

If equation (2.3) is nondimensionalized with respect to the heat conduction scales (2.6), the Marangoni number defined by equation (2.4) occurs naturally in the dimensionless form

$$\nabla\ (\vec{V} \cdot \vec{t}) \cdot \vec{n} = Ma\ \nabla \Theta \cdot \vec{t} \tag{2.10}$$

Considering that the dimensionless temperature gradient is of order one, the above equation indicates that the strength of the shear stress in the free surface region is proportional to the Marangoni number; this shear stress, in turn, induces convection within the body of the fluid. Thus, the Marangoni number describes the strength of convection due to the surface tension gradient.

2.3.4 Marangoni Convection Scales

For a flow where viscous effects dominate, the reference velocity scale for thermocapillary convection is

$$U \sim \frac{(d\gamma/dT)\ \Delta T}{\mu} \tag{2.11}$$

whereas for a highly convective flow,

$$U \sim \left\{ \frac{(d\gamma/dT)^2 (\Delta T)^2}{\varrho \mu d} \right\}^{1/3} \tag{2.12}$$

2.4 Governing Equations and Solution Procedure

The governing equations in Cartesian coordinates for two-dimensional, incompressible flow can be written in dimensional form as:

continuity:

$$\frac{\partial \varrho}{\partial t} + \frac{\partial(\varrho u)}{\partial x} + \frac{\partial(\varrho v)}{\partial y} = 0 \tag{2.13a}$$

x-momentum:

$$\frac{\partial(\varrho u)}{\partial t} + \frac{\partial(\varrho uu)}{\partial x} + \frac{\partial(\varrho uv)}{\partial y} = -\frac{\partial p}{\partial x} + \left[\frac{\partial}{\partial x}\left(\mu\,\frac{\partial u}{\partial x}\right) + \frac{\partial}{\partial y}\left(\mu\,\frac{\partial u}{\partial y}\right)\right] + S_u(x,y) \tag{2.13b}$$

y-momentum:

$$\frac{\partial(\varrho v)}{\partial t} + \frac{\partial(\varrho uv)}{\partial x} + \frac{\partial(\varrho vv)}{\partial y} = -\frac{\partial p}{\partial y} + \left[\frac{\partial}{\partial x}\left(\mu\,\frac{\partial v}{\partial x}\right) + \frac{\partial}{\partial y}\left(\mu\,\frac{\partial v}{\partial y}\right)\right] - \left(\varrho - \varrho_{ref}\right) g + S_v(x,y) \tag{2.13c}$$

energy:

$$\frac{\partial(\varrho C_p T)}{\partial t} + \frac{\partial(\varrho u C_p T)}{\partial x} + \frac{\partial(\varrho v C_p T)}{\partial y} = \left[\frac{\partial}{\partial x}\left(k\,\frac{\partial T}{\partial x}\right) + \frac{\partial}{\partial y}\left(k\,\frac{\partial T}{\partial y}\right)\right] + S_T(x,y) \tag{2.13d}$$

In the above, the dimensional form has been chosen because it is convenient to represent variable physical properties such as ϱ, the density, μ, the viscosity, k, the conductivity, and C_p, the specific heat in the conservative form. Here, u is the velocity component in the x–direction, v is the velocity component in the y–direction, p is the pressure, T is the temperature, and g is acceleration due to gravity, The gravity vector $\vec{g} = -g\,\hat{j}$ is assumed to be in the –y direction. For inclined configurations, the appropriate components should appear in both the momentum equations. S_u, S_v and S_T are appropriate source terms in the governing equations. The form of the source terms is problem dependent and will be described later in the appropriate context.

It frequently is convenient to write and solve the governing equations in generalized, nonorthogonal, curvilinear coordinates, especially to fit complex geometries and implement the boundary conditions on surfaces or walls with arbitrary orientations. Furthermore, in many applications it is desirable to preferentially improve grid distribution in certain regions of the flow. These regions may be determined manually or may evolve dynamically during the solution process.

The transformation may be expressed as

$$\begin{aligned} \xi &= \xi(x, y) \\ \eta &= \eta(x, y) \end{aligned} \tag{2.14a}$$

The continuity equation in nonorthogonal coordinates then becomes,

$$\frac{\partial}{\partial t}(J\varrho) + \frac{\partial(\varrho U)}{\partial \xi} + \frac{\partial(\varrho V)}{\partial \eta} = 0 \tag{2.14b}$$

where

$$J = x_\xi y_\eta - x_\eta y_\xi \tag{2.14c}$$

is the Jacobian of the transformation and

$$\begin{aligned} U &= u y_\eta - v x_\eta \\ V &= v x_\xi - u y_\xi \end{aligned} \tag{2.14d}$$

are the contravariant velocity components. The momentum equations then become

$$\begin{aligned} \frac{\partial(J\varrho u)}{\partial t} + \frac{\partial(\varrho U u)}{\partial \xi} + \frac{\partial(\varrho V u)}{\partial \eta} = &- \left\{ y_\eta \frac{\partial p}{\partial \xi} - y_\xi \frac{\partial p}{\partial \eta} \right\} + \frac{\partial}{\partial \xi}\left[\frac{\mu}{J}\left(q_1 u_\xi - q_2 u_\eta \right) \right] \\ &+ \frac{\partial}{\partial \eta}\left[\frac{\mu}{J}\left(q_2 u_\xi - q_3 u_\eta \right) \right] + S_u(\xi, \eta) \cdot J \end{aligned} \tag{2.14e}$$

$$\begin{aligned} \frac{\partial(J\varrho v)}{\partial t} + \frac{\partial(\varrho U v)}{\partial \xi} + \frac{\partial(\varrho V v)}{\partial \eta} = &- \left\{ x_\xi \frac{\partial p}{\partial \eta} - x_\eta \frac{\partial p}{\partial \xi} \right\} + \frac{\partial}{\partial \xi}\left[\frac{\mu}{J}\left(q_1 v_\xi - q_2 v_\eta \right) \right] \\ &+ \frac{\partial}{\partial \eta}\left[\frac{\mu}{J}\left(q_2 v_\xi - q_3 v_\eta \right) \right] - \left(\varrho - \varrho_{ref} \right) g \cdot J + S_v(\xi, \eta) \cdot J \end{aligned} \tag{2.14f}$$

along x and y directions respectively, where x_η, y_η and so on are the metrics of the transformation and q_1, q_2 and q_3 are defined as

$$\begin{aligned} q_1 &= x_\eta^2 + y_\eta^2 \\ q_2 &= x_\xi x_\eta + y_\xi y_\eta \\ q_3 &= x_\xi^2 + y_\xi^2 \end{aligned} \tag{2.14g}$$

The energy and other scalar transport equations can be written down in a similar manner and will not be repeated here. The advantage of this form is that complex geometries can be fitted by body-conforming grids, whereby boundary conditions can be applied easily and the grid can be distributed preferentially in desired regions so as to obtain better resolution.

A pressure-based numerical procedure, SIMPLE, has been chosen for computing laminar incompressible flows of interest in this work. The details of the basic pressure correction algorithm are given in Patankar (1980), with the extension of the procedure to general curvilinear coordinates given in Shyy (1994). The present implementation of the algorithm follows the work of Braaten and Shyy (1986) and Shyy et al. (1985). A staggered grid arrangement is adopted for the discretization of Eqs. (2.14b–f) with the layout of the flow variables illustrated in Fig. 2.1. The finite volume form of the conservation laws may be obtained by integrating Eqs. (2.14b–f) over the sample control volume shown in Fig. 2.1. The diffusion terms are always approximated using second order central differences in this study and the time derivative by a first order backward Euler scheme. A variety of convection schemes have been used and a detailed discussion is provided later in the next section. In the SIMPLE algorithm, a segregated approach is adopted wherein the momentum, energy and other scalar equations are solved in a sequential manner. A pressure correction approach (Patankar 1980, Shyy 1994) is used to enforce mass continuity in each discrete control volume and the velocity components are corrected by the consistent and efficient D'yakonov procedure discussed in detail in Shyy (1994).

2.5 Formulation and Methodology for Free Surface Computation

Now, it is appropriate to take up the study of the generation of meniscus shapes for float zone configurations. The formation of the meniscus during the melting process is a major concern in the successful operation of the float zone technique and this aspect will be the

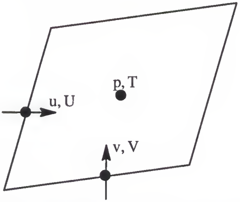

Figure 2.1. Layout of the dependent variables on the staggered grid. The direction of the contravariant velocities are different from the cartesian components. The contravariant components are perpendicular to the respective grid lines on which they are defined.

considered in detail in the next chapter by means of several examples. Specifically, the issues of existence, multiplicity and sensitivity of solutions to the Young–Laplace equation representing the liquid meniscus formed under equilibrium conditions, subject to different combinations of Bond number, aspect ratio and pressurization, will be addressed in this chapter and investigated by mean of several examples described in the next chapter. A free energy concept originated by Shyy et. al. (1993) is described next and will be applied to address the physical realizability of a given meniscus shape. The approach is static in nature, which is a satisfactory approximation considering the slow speed of the movement of the melt. Fig. 1.1 is a schematic illustration of the float zone process and Fig. 2.2 is a schematic of the mathematical model, which allows, as it should, the trijunction point to move to satisfy a given value of the static contact angle or other constraints such as a fixed volume of the melt.

Meniscus profiles obey the Young–Laplace equation in axisymmetric form (Finn 1986, Myshkis et. al. 1987, Shyy 1994), which relates the curvature of the free surface to the pressure difference across it. The governing equation describes the generation of surface curvature to balance the sum of the hydrostatic pressure and pressurization. Specialized to an axisymmetric geometry, it can be written as follows:

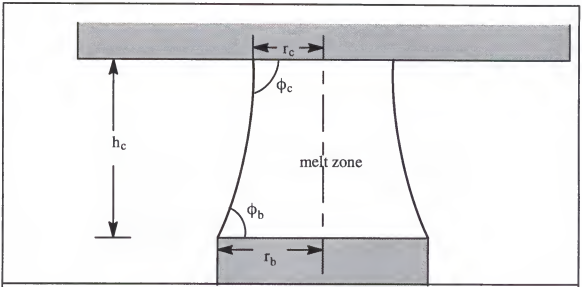

Figure 2.2. Schematic of the mathematical model. Major simplifications involve isothermal melt zone and a flat solid–liquid interface as opposed to the curved one shown in Fig. 1.1. Axisymmetry has been assumed.

$$\Delta\varrho \; g \; y - \Delta P = \gamma \left[\frac{f''}{(1 + f'^2)^{3/2}} - \frac{1}{f \; (1 + f'^2)^{1/2}} \right] \tag{2.15a}$$

where $\Delta\varrho$ is the density difference between the ambient and the melt and ΔP is the pressurization. γ is the surface tension coefficient and the meniscus is described by $f = r(y)$, where r is the radius and y is the vertical coordinate. A variety of boundary conditions have been treated in literature, such as fixed contact angles at both top and bottom (Finn 1986, Concus 1990, Myskis et. al. 1987), fixed radius at the bottom and fixed contact angle at the top (Shyy et. al. 1993) and fixed radius at both top and bottom (Coriell et. al. 1977, Li et. al. 1993, Kobayashi 1984, Kobayashi 1988, Zhang and Alexander 1992, Murthy 1987). These conditions have been devised for configurations under different physical constraints. In the context of floating zones, the boundary conditions to be imposed may vary depending on the operating conditions. Therefore this study has been conducted with a variety of different constraints imposed on the solutions. The following boundary conditions may be imposed:

$$f\,(y{=}0) = r_b \tag{2.15b}$$

either

$$f\,(y{=}h_c) = r_c \tag{2.15c}$$

or $$f'(y{=}h_c) = \tan(\pi/2 - \phi_c) \tag{2.15d}$$

Figure 2.2 shows a schematic of the geometry. For an isothermal liquid bridge, Eq. (2.15a) can be nondimensionalized with a length scale of r_b and:a pressure scale of γ/r_b, to yield,

$$\mathrm{Bo}\ \hat{y} - \Delta\hat{P} = \left[\frac{\hat{f}''}{(1+\hat{f}'^2)^{3/2}} - \frac{1}{\hat{f}\,(1+\hat{f}'^2)^{1/2}}\right] \tag{2.16}$$

where the italics indicate non–dimensionalized quantities. Bo is the Bond number defined as:

$$\mathrm{Bo} = \frac{\Delta\varrho\ g\ r_b^2}{\gamma} \tag{2.17}$$

In Shyy et. al. (1993), the nonlinear differential equation, Eq. (2.16), has been solved subject to a fixed radius at the lower boundary and a fixed contact angle at the top boundary. Such a two point boundary value problem cannot yield an unique solution. Thus there arises the problem of selecting, out of the multiple solutions that are mathematically permissible, the one that corresponds to the physical equilibrium condition that exists in reality. Therefore we now invoke the thermodynamic condition that at equilibrium the free energy is a minimum and select the solution that minimizes the free energy.

For simplicity, consider only the isothermal condition with no phase change and examine the Helmholtz free energy, F = U – TS which contains three contributions:

(i) The potential energy from the effective head

$$U_1 = \int \pi f^2\ (\Delta\varrho g y - \Delta P)\ dy \tag{2.18a}$$

(ii) The surface energy of the meniscus forming the gas–liquid interface

$$U_2 = \int 2\pi\ \gamma\ f\left(1 + f'^2\right)^{1/2}\ dy \tag{2.18b}$$

(iii) The surface energy needed to wet the solid–liquid wetted area

$$U_3 = \left(\gamma_{ls} - \gamma_{sg}\right)\pi\ r_c^2 \tag{2.18c}$$

and from Young's contact condition this becomes,

$$U_3 = -\gamma \cos\phi_0 \, \pi \, r_c^2 \tag{2.18d}$$

where ϕ_0 is the static contact angle. The equilibrium shape is the one that minimizes the total free energy:

$$E = \int_0^{h_c} \left[\pi f^2 (\Delta\varrho g y - \Delta P) + 2\pi \gamma f (1 + f'^2)^{1/2} \right] dy - \pi \gamma r_c^2 \cos(\phi_0) \tag{2.18e}$$

The Young–Laplace equation may be integrated starting with a fixed radius and base angles, $-\pi/2 < \phi_b < \pi/2$, to yield all possible solutions for a given aspect ratio of the domain. Subsequently, solutions satisfying a given contact angle at the top, ϕ_c, are selected and their free energies calculated according to Eq. (2.18e). If any of these solutions locally minimize the free energy, then these profile shapes are statically stable.

As described in Shyy et. al. (1993) and Shyy (1994), the value of ϕ_o is specified, and E is calculated by fixing the value of ϕ_0 in Eq. 18e) and scanning through the whole range of meniscus profiles obtained by fixing the lower trijunction location (with varying angle) and the height of the upper trijunction point (with varying locations and angles), distinct extrema are obtained at specified values of ϕ_o . Among the multiple solutions, the one corresponding to a point of minimum on the curve is the physically realizable stable meniscus profile. When either a maximum or a non–extremum point arises, the solution is unstable.

The volume of the melt zone in non–dimensional form is given by,

$$V = \int_0^{AR} \pi \, \hat{f}^2 \, d\hat{y} \tag{2.19a}$$

where

$$AR = h_c/r_b \tag{2.19b}$$

is the aspect ratio of the zone. In float zones, the meniscus profiles may be required to enclose a fixed volume of the melt thus satisfying Eq. (2.19) (Coriell et. al. 1977, Finn 1986, Myshkis 1987, Zhang and Alexander 1992, Li et. al. 1993). Furthermore, non–isothermal liquid bridges need to be considered considered for the float zone, see for instance Zhang and Alexander (1992). However, the present study described in the next chapter, will be restricted to the isothermal case to simplify the number of parameters involved. The aim is to determine the sensitivity of the profile shapes to the imposed boundary conditions. As will be demonstrated, the basic considerations from free energy and uniqueness can shed useful light on the issues relevant to the float zone. It is also noted that additional forces may be generated on the free surface due to electromagnetic effects if the zone is heated by an induction coil (Lie et. al. 1989, Riahi and Walker 1989).

Dynamic effects have been considered as secondary effects for the purposes of this analysis; however, they are incorporated later in this work with fully coupled moving grid calculations with fluid convection, phase change and free surface dynamics. Dynamic effects have been also considered by several investigators (Langbein 1992, Tsamopoulos et. al. 1988 and Tsamopoulos et. al. 1992). Quasiequilibrium studies involving contact angle hysterisis have been treated in Shyy et. al. (1993) and Shyy (1994). It is considered that the phenomenon of contact angle hysterisis is largely due to surface roughness (Huh and Mason 1977) and surface inhomogeneity (Shyy 1994). In the following, it is considered that the melt zone moves slowly and a static consideration suffices.

2.6 Results and Discussion

Meniscus profiles were obtained by solving the Young–Laplace equation in cylindrical coordinates subject to the boundary conditions of fixed radius at the bottom and either (I) fixed contact angle at the top, or (II) fixed volume of the liquid bridge (half domain assuming axial symmetry).

2.6.1 Low Bond Number

Initial calculations were conducted following the model proposed by Shyy et. al. (1993) and compared with experimental data provided by Dreeben et. al (1980). The parameters were as follows: $r_b = 2.42 \times 10^{-4}$ m, Bo = 2.825×10^{-3}, $\mathcal{R} = 2.24$, contact angle, $\phi_c = 115$ deg and pressurization, $\Delta P = 4.35\%$ of the ambient pressure given by $P_{ambient} = 1.0 \times 10^5$

Nm^{-2}. In this chapter, ΔP is always specified as a percentage of $P_{ambient} = 1.0 \times 10^5$ Nm^{-2}. Here r_b is the radius of the feed rod and it is assumed that the meniscus profile is pinned to the edge of the feed rod. It may be noted from the photographs of floating zones provided in Dreeben et. al. (1980) that the contact angle is not constant over the contact line nor is the liquid bridge axisymmetric. The solid–liquid interface is curved and not flat as is assumed in the simplified model used in the present calculations. It may also be noted that the variation of surface tension with temperature is also not considered in this model. The material under consideration is Sapphire (Al_2O_3) whose properties are listed in Table 2.1.

Figure 2.3 shows the meniscus profiles obtained using the theoretical model as well as the experimental data. In Fig. 2.3, (i) shows the actual profiles obtained by integrating the Young–Laplace equation, that satisfy the imposed contact angle condition at the top. (ii) shows the r_c versus ϕ_c, (iii) shows ϕ_c versus ϕ_b and (iv) is the free energy curve, E versus ϕ_c. In (i), the experimental data from Dreeben et. al. (1980) is shown alongside for comparison purposes. (ii) and (iii) show the range of solutions which may be obtained from the Young–Laplace equation. It is obvious that there are two solutions satisfying the given contact angle condition. The profile that minimizes the free energy is shown with a solid line and it matches the experimentally observed profile closely.

A sensitivity study has been conducted to study the formation and physical realizability of the meniscus profiles subject to various boundary conditions and parameters. First, holding the Bond number constant, the aspect ratio was varied over the range $0.5 \leq AR \leq 4.0$.

Figure 2.4 shows the profile shapes at each aspect ratio. Figure 2.5 is a summary of the results obtained by imposing a desired contact angle, $\phi_c = 115$ deg for the various aspect ratios considered. Multiple solutions may exist especially at lower aspect ratios The available solutions are marked with an ' × ' and the solutions having the lower free energy are marked with ' ⊗ '. A notable characteristic is the rapid variation in the meniscus profiles for aspect ratios in the range, $2.25 \leq AR \leq 2.5$. The value of r_c which shows a decreasing

$Bo = 2.825 \times 10^{-3}$, $\Delta P = 4.35\%$, $P_{ambient} = 1.0 \times 10^{5} Nm^{-2}$, Æ = 2.24

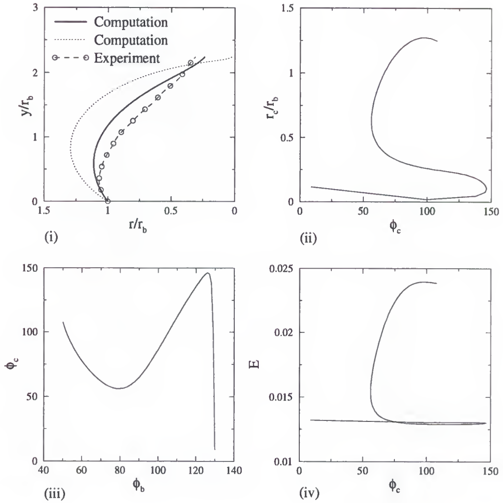

Figure 2.3. Comparison of calculated meniscus shapes with the experimental data of Dreeben et. al. (1980). (i) Calculated and experimentally obtained profiles. It may be observed that two solutions are obtained with the given contact angle of 115 deg. The profile with the lower free energy is closer to the experimentally observed profile. (ii) r_c/r_b versus ϕ_c (iii) ϕ_c vs ϕ_b (iv) Free energy, E vs ϕ_c

trend with increasing aspect ratio up to Æ = 2.25 shows a sudden increase as the aspect ratio increases to 2.5. The decreasing trend resumes thereafter. Only the profiles having the lower free energy are shown. Profiles with aspect ratio of 2.5 and higher show a 'neck' or turning point.

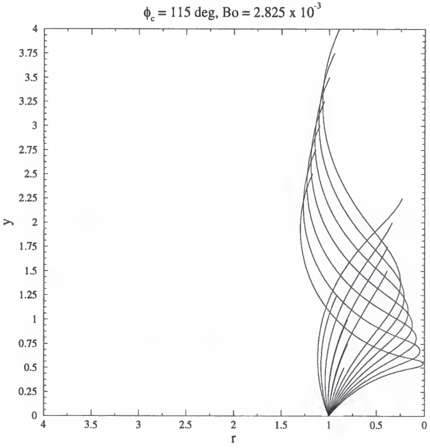

Figure 2.4. Profiles satisfying contact angle of 115 deg. for Bo = 2.825 x 10^{-3} for $0.5 \leq AR \leq 4.0$ Only profiles with the lower free energy are shown.

Table 2.1 Bond numbers for materials of interest. $r_b = 1.25 \times 10^{-2}$ m. Data obtained from Keene (1993) and Li et. al. (1993).

material	density	surface tension	Bond Number
Al_2O_3	3400 kg m^{-3}	0.69 N m^{-1}	7.55
GaAs	5720 kg m^{-3}	0.455 N m^{-1} (w.r.t B_2O_3)	13.72 (with encapsulant)
NiAl	5000 kg m^{-3}	1.35 N m^{-1}	5.68

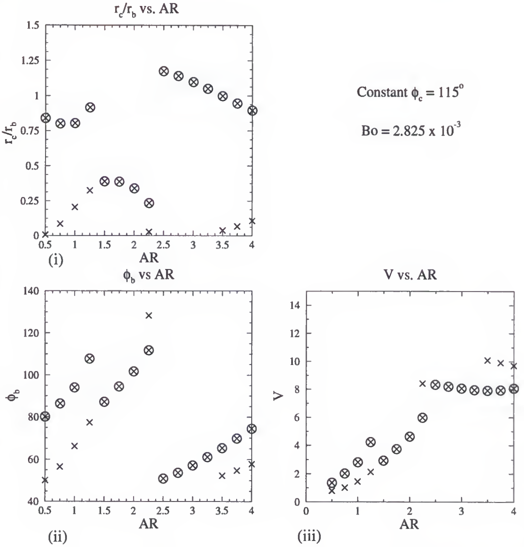

Figure 2.5. Solutions for an imposed contact angle of 115 deg in the range $0.5 \leq AR \leq 4.0$
(i) r_c vs. the aspect ratio. Note the change in the trend of the solutions when the aspect ratio changes from 2.25 to 2.5. (ii) ϕ_b that give rise to the imposed contact angle. (iii) volume vs. the aspect ratio. In all cases, if multiple solutions are obtained, then the solutions with the lower free energy are marked with a ' ⊗.'

With a set pull rate and heater power, at steady state, the float zone occupies a prescribed volume. Hence it is useful to examine the solution characteristics subject to the constraint of a fixed volume. However, in reality, the change in heat transfer characteristics due to the coupling between the movement of the float zone and heat transfer due to conduction as well as buoyancy driven flow, may result in changes of the prescribed melt volume with time.

Furthermore, the issue of viewing the static contact angle as a material property needs to be addressed also.

Figure 2.6 displays free energy curves at selected aspect ratios. It may be seen that all the selected curves, except the case of ÆR = 1.75, show a local minimum at $\phi_o = 115$ deg. The profile shown at ÆR = 1.75 cannot achieve static stability for the specified contact angle.

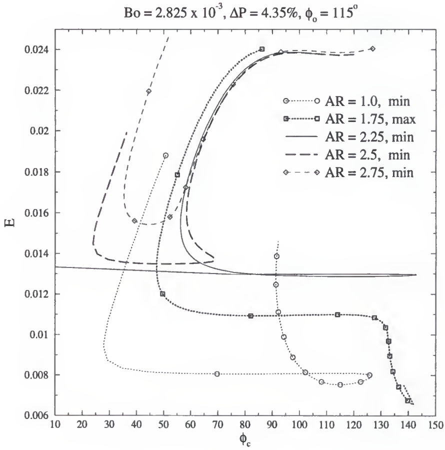

Figure 2.6. Energy versus ϕ_c curves for selected aspect ratios and $\phi_o = 115$ deg. It may be noted that at an aspect ratio of 1.75, the free energy curve shows a local maximum and hence cannot be statically stable. All other curves display a local minimum indicating static stability.

It is interesting to observe that such a "window" of AR exists within which, although the mensci exist mathematically, they are not physically realizable. Above and below this "window" statically stable menisci exist. In particular, it may be noted that profiles at AR = 2.5 and 2.75 exhibit 'necking.' The stability implication of such a shape needs to be addressed in a dynamic framework. Here, the necking can satisfy the static stability requirement.

Figures 2.7 and 2.8 are the corresponding solutions that satisfy a fixed volume criterion of V = 5.908, chosen so as to correspond with the theoretical solution shown in Figure 2.3. In this case the solution characteristics vary smoothly with the aspect ratio. However, the r_c shows a qualitatively different trend as the aspect ratio changes from 2.25 to 2.5. The corresponding meniscus profiles shown in Figure 2.8 start to exhibit a 'neck' in the profile for aspect ratios of 2.5 and above, although the 'necks' are shallower than those seen in the fixed contact angle, ϕ_c = 115 deg case shown in Figure 2.4. The contact angle, ϕ_c, correspondingly exhibits a sharp decrease as the aspect ratio increases from 2.25 to 2.5. This is consistent with the appearance of turning points or 'neck' in the profile shapes as shown in Figure 2.8.

The next case shown in Figure 2.9 examines the sensitivity of the solutions to changes in the Bond number. The Bond number was doubled to Bo = 5.650×10^{-3} retaining the pressurization of 4.35%. Figure 2.9 shows the range of the available solutions. It is readily noted that there is a substantial reduction in the range of the available solutions. The Young–Laplace equation cannot be integrated for aspect ratios greater than 0.75. The ϕ_c versus ϕ_b curves show that multiple solutions do not exist for the aspect ratios considered. It may be concluded that for the parameter ranges and geometrical configurations considered that the meniscus profiles are most sensitive to variations in Bond number rather than variations in the aspect ratio or the different boundary conditions used in the calculations. This set of computations can help explain the non–existence of floating zones as the surface tension coefficient is not sufficient to counteract the hydrostatic pressure of the melt.

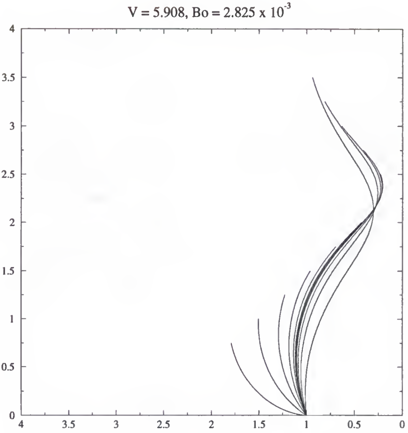

Figure 2.7 Profiles satisfying constant volume, $V = 5.908$, for $Bo = 2.825 \times 10^{-3}$ for $0.5 \leq AR \leq 4.0$ Only profiles with the lower free energy are shown.

2.6.2 High Bond Number

In practice, the geometrical configurations employed result in a high value of the Bond number. In particular, we are interested in the following configuration. Given a feed rod diameter of 25 mm, Table 2.1 shows the surface tension coefficients and the corresponding Bond numbers for some materials of current interest.

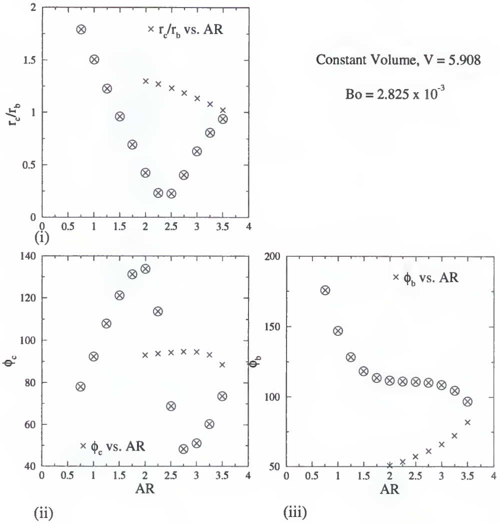

Figure 2.8 Solutions for an fixed volume of 5.9 in the range $0.5 \leq AR \leq 4.0$
(i) r_c versus the aspect ratio
(ii) ϕ_c versus the aspect ratio
Note the change in the trend of the solutions when the aspect ratio changes from 2.25 to 2.5. (iii) ϕ_b that give rise to solutions satisfying V = 5.9. In all cases, if multiple solutions are obtained, then the solutions with the lower free energy are marked with a ' ⊗ ' .

2.6.3 Determination of Pressurization Values

The meniscus shape is substantially influenced by the value of ΔP, pressurization, in Eq. (2.15). In literature, the value of the pressurization is usually determined by satisfying a constant volume criterion in addition to the boundary conditions imposed. In the present

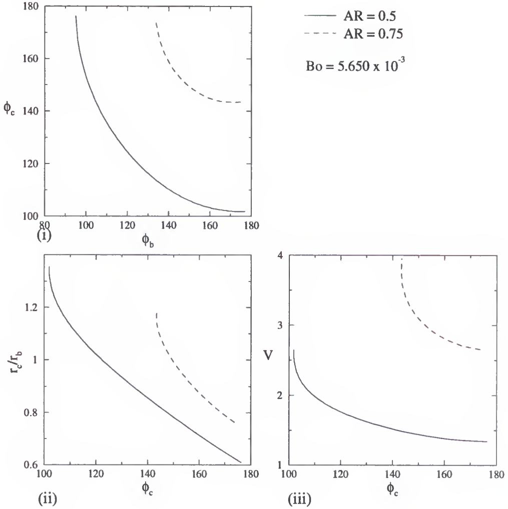

Figure 2.9. Solutions for Bo = 5.65 x 10^{-3}. Solutions are obtained for aspect ratio of 0.5 and 0.75. The decrease in the number of available solutions may be noted as opposed to the case of Bo = 2.825 x 10^{-3}.
(i) ϕ_c vs. ϕ_b
(ii) r_c vs. ϕ_c and
(iii) volume vs. ϕ_c.

calculations, the objective was to, instead, find a range of pressurization values for which aspect ratios close to unity can be achieved. The result of such a search is described in Fig. 2.10. A Bond number of 8.8 was selected in order to effect a comparison with the results of Quon et. al. (1993). The pressurization ranges obtained from Fig. 2.10 are used to generate the subsequent solutions.

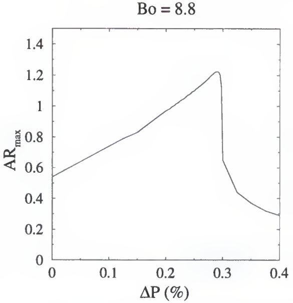

Figure 2.10 Maximum achievable aspect ratio versus pressurization for a Bond number of 8.8. The pressurization is calculated as a percentage of the ambient pressure, $P_{ambient} = 1.0 \times 10^5\ Nm^{-2}$.

2.6.4 Solutions for Aspect Ratio of Unity

Calculations were carried out for aspect ratio of unity, Bond number of 8.8 and six values of pressurization in the range, $0.2 \leq \Delta P \leq 0.3$. Figures 2.11 and 2.12 show the results of the calculations.

Figure 2.11 shows the profiles and the corresponding free energy curves that are obtained when contact angles of 30 deg and 60 deg are imposed. The free energy curves also indicate the range of contact angles for which the Young–Laplace equation can be integrated. It is useful to draw attention to the case of $\phi_o = 30$ deg, $\Delta P = 0.2295\%$. It may be observed that two profiles are obtained, marked in Fig. 2.11(i) with the solid curves, one of them also marked with '○'. The corresponding free energy curve in Fig. 2.11(iii) is marked with '□' and shows that two solutions can be obtained, one of which satisfies a local minimum. In Fig. 2.11(i), the unmarked solid curve satisfies a local minimum indicating static stability. For $\phi_o = 60$ deg, none of the obtained profiles satisfy a local minimum.

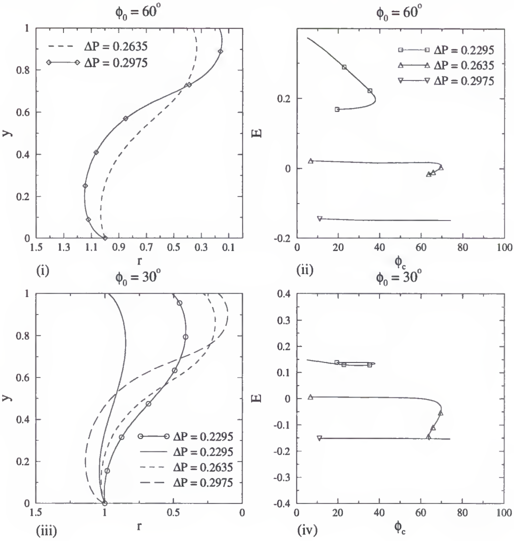

Figure 2.11 Calculations for Bond number of 8.8, unity aspect ratio and imposed contact angle condition.
(i) and (iii) Profiles meeting a desired contact condition of 60 deg and 30 deg respectively. (ii) and (iv) Free energy curves for imposed contact angles of 60 deg and 30 deg respectively, for the various values of the pressurization considered.

The curves in (ii) and (iv) use the same convention to indicate the pressurization value. (ii) and (iv) also indicate the range of values of ϕ_c that are obtainable by integrating the Young-Laplace equation. It may be noted that for $\phi_o = 30$ deg, and $\Delta P = 0.2295\%$, there are two profiles satisfying the given contact condition, indicated by the solid curves. The profile marked with o does not minimize the free energy whereas the unmarked one does. None of the other profiles corresponds to a local minimum indicating that although they mathematically satisfy the Young-Laplace equation, they are not statically stable.

Figure 2.12 shows profiles that (i) meet a fixed radius, r_c, condition for three values of r_c/r_b = 1.0, 0.75 and 0.5, and (ii) meet a fixed volume constraint of V = 2 and 3 (non–dimensionalized). The corresponding r_c versus ϕ_c and V versus ϕ_c show the overall range over which the Young–Laplace equation can be integrated. It may also be noted that the overall solution behavior does not show any abrupt changes as the pressurization, ΔP, is varied over the specified range. Hence, the curves shown in Fig. 2.12(iv) help in determining the existence of solutions that can simultaneously satisfy a given contact angle condition and a fixed volume. The free energy curves, such as those shown in Fig. 2.12(iii), show whether the calculated profiles shapes are statically stable.

2.7 Concluding Remarks

In this chapter, a formulation has been presented for fluid flow and heat transfer for thermally induced buoyancy driven flow and thermocapillary convection. This chapter also addresses the problem of integrating the Young–Laplace equation to determine the free surface shapes formed during float zone growth. Questions regarding the existence and uniqueness of the solutions to the static Young–Laplace equation are addressed in the context of a free energy minimization criterion. The method is validated against available experimental data. A variety of calculations have been carried out to determine free surface shapes over a range of Bond numbers, aspect ratios, internal pressurization and different boundary conditions. These calculations form the building block for determining the meniscus in float zone calculations. The governing equations and the solution methodology discussed in this chapter have been used for all the convective heat transfer computations in this work.

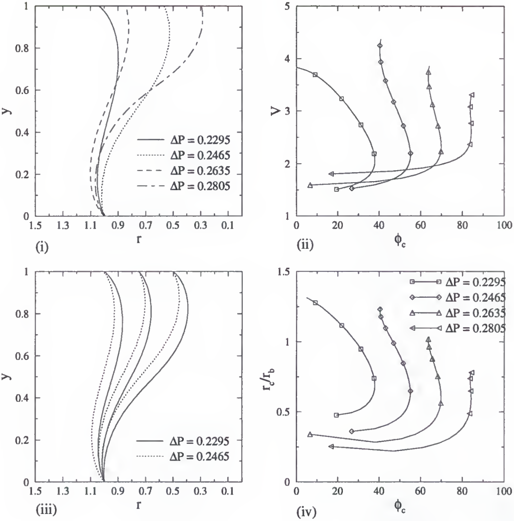

Figure 2.12 Calculations for Bond number of 8.8, unity aspect ratio and either (a) imposed radius at the top or (b) imposed volume of the melt. Profiles for (i) fixed volume and (iii) fixed r_c (for three different r_c).

(ii) volume versus ϕ_c curves and
(iv) r_c/r_b versus ϕ_c.

The curves in (ii) and (iv) use the same convention to indicate the pressurization value. (ii) and (iv) also indicate the range of values of ϕ_c that are obtainable by integrating the Young–Laplace equation.

CHAPTER 3
CONVECTIVE HEAT TRANSFER COMPUTATIONS

3.1 Background

In this chapter, the implementation of various convection schemes is discussed using the benchmark solution for natural convection in a cavity as the vehicle for testing and development. The developed techniques are then applied to compute transient natural convection in an enclosure and thermocapillary convection in a liquid bridge of molten NiAl. The validity of the static free surface assumption of the previous chapter is also assessed by an a posteriori estimation based on the thermocapillary convection in the liquid bridge.

3.2 Convection Treatment and Accuracy Assessment

Treatment of the convection terms is one of the most fundamental issues in Navier–Stokes computations. It is well established that the first order upwind scheme is the most stable one and does not produce numerical oscillations, at the cost of smearing out the sharp gradients which are usually present in a convection dominated flow. To overcome the problem of excessive numerical diffusion, numerous treatments have been proposed which are nominally second order accurate, based on a Taylor series expansion, but cannot guarantee physical realizability. Such schemes cannot be used with confidence for some scalar variables such as temperature, turbulent kinetic energy or rate of turbulent energy dissipation, which should be non–negative. Hence, it is not uncommon to adopt the practice of treating the convection terms in the momentum equations with higher order schemes, while employing a lower order scheme for transport equations of conserved scalar quantities. One such low order scheme is the hybrid scheme which is a combination of the first order upwind scheme and the second order central difference scheme. The impact of such a mixed discretization on the solution accuracy, however, needs to be assessed.

An appropriate test vehicle for such an assessment is the natural convection of air in a square cavity with differentially heated side walls. Accurate benchmark solutions for this problem exist in literature (de Vahl Davis 1983, Hortmann et. al. 1990) and are available for comparison with the present calculations. The Rayleigh number for the calculations is 10^6 and the Prandtl number for air is 0.71. The top and bottom walls are insulated. The right and left walls are maintained at constant temperatures of T_0 and T_1 respectively; in nondimensional terms they can be normalized to 1.0 and 0.0 respectively. The governing equations are the two dimensional steady Navier–Stokes and energy equations (2.9). The Boussinesq approximation has been employed wherein the density variations are neglected in all the terms of the governing equations except the source term for the v–momentum equation. Figure 3.13 shows a schematic of the problem domain.

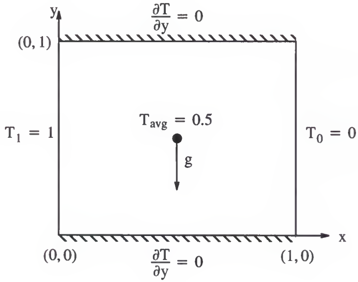
y
$\frac{\partial T}{\partial y} = 0$
(0, 1)
$T_{avg} = 0.5$
$T_1 = 1$
$T_0 = 0$
g
x
(0, 0)
$\frac{\partial T}{\partial y} = 0$
(1, 0)

Figure 3.13 Natural convection of air in a differentially heated square cavity.

An important feature of the solution is that it satisfies the following centrosymmetry conditions.

$$\begin{aligned} u(x,y) &= -\,u(1-x,1-y) \\ v(x,y) &= -\,v(1-x,1-y) \\ T(x,y) &= -\left(\,T(1-x,1-y) - T_{avg}\,\right) \\ \psi(x,y) &= \psi(1-x,1-y) \end{aligned} \tag{3.1}$$

where $\psi(x,y)$ is the stream function and $T_{avg} = 0.5\left(T_1 + T_0\right)$. While this feature of the solution was not directly utilized in the computational procedure, it was used as an indicator of convergence of the solutions to machine accuracy.

The solution technique was the SIMPLE algorithm described in the previous section. The central difference method was used to evaluate the diffusion fluxes. The following convection schemes employing different profile assumptions were tested on the convection terms:

(i) Central differences for both momentum and energy equations,

(ii) Second order upwind for both momentum and energy equations, and

(iii) A mixed treatment consisting of the second order upwind scheme for the momentum equations and the hybrid scheme for the energy equation.

It may be noted that while the implementation of the central differencing scheme is well established due to its simplicity, that of the second order upwind is not. The central difference scheme computes the convective flux as a linear interpolation of the values in two neighboring control volumes. However, the second order upwind scheme has been treated in a variety of ways resulting in inconsistent performance in literature (Shyy et. al. 1992, Vanka 1987). The scheme adopted in this study is that proposed by Shyy et. al. (1993) where the convective flux is evaluated by a linear extrapolation of the dependent variable from two nearest upwind neighbors. This results in a conservative treatment and yields consistent performance with respect to grid refinement for two dimensional driven cavity flows (Shyy et. al. 1993). In this work, the same implementation is tested against natural convection flow. The present investigations and the results of Shyy et. al. (1993), together give a more comprehensive account of the performance of the second order upwind scheme for complex flow calculations. The two cases represent two different types of problems, one induced by shear stress and the other by body force.

Two benchmark solutions are available for the purpose of comparison. One is due to de Vahl Davis (1983). This work used the streamfunction – vorticity formulation of the governing equations. Central differencing was used for all spatial derivatives and the method of false transients using first order forward difference in time was used to solve the equations. The finest grid used was an uniform 81 × 81 mesh. Richardson extrapolation was then used to obtain more accurate grid independent results for the dependent variables and the derived quantities such as the Nusselt number. Another benchmark solution is that due to Hortmann et. al. (1990). This work solved the Navier–Stokes equations using a SIMPLE–like solution algorithm for a finite volume formulation on a non–staggered grid. Central differencing was used to discretize all convection terms. A multigrid procedure was used to solve the resulting systems of linearized equations. Computations were carried out for grid sizes up to 321 × 321 on an uniform grid and up to 641 × 641 on a non–uniform grid. The results are considered accurate to within 0.01%.

In the current study, computations have been carried out on uniform grids of up to 81 × 81 using a variety of approximations for the convection terms. Comparisons have been carried out with the solution of Hortmann et. al. (1990) for all quantities considered except the streamfunction. Since the streamfunction data is not available in Hortmann et. al. (1990), the required data has been obtained from de Vahl Davis (1983).

Computation of the local heat transfer rate utilizes the staggered grid arrangement for a consistent evaluation of the heat flux. The expression for the convective part of the heat flux is consistent with the convection scheme used in the computations. This ensures that the total heat flux crossing any vertical line is a constant throughout the cavity.

3.2.1 Results and Discussion

Figure 3.14 shows the contour plots of the streamfunction, isotherms and heat flux. The streamfunction plots shows the vertical boundary layers developing along the isothermal walls and the horizontal boundary layers along the adiabatic walls. Centrosymmetry of the solution can be observed. Also, three secondary vortices rotating in the clockwise direction can be seen. Two of these are displaced towards the walls in the streamwise direction and the third is a central vortex that separates these two. Distortion of the isotherms in the streamwise direction can be observed in these regions. It should be noted that the heat flux function cannot satisfy the centrosymmetry condition.

Comparisons of the obtained solutions with the benchmark solutions have been made. The following quantities have been used for comparison and error analysis in this study.

(i) Streamfunction at the midpoint of the cavity,

(ii) Average Nusselt number,

(iii) Maximum u–velocity on the vertical mid–plane of the cavity (u_{max}), and

(iv) Maximum v–velocity on the horizontal mid–plane of the cavity (v_{max}).

Figure 3.15 shows the percentage relative errors versus the grid spacing, h, for all solutions due to the different convection schemes used. It can be observed that, for the derived quantities — the Nusselt number and the streamfunction — the mixed treatment is the most accurate. Overall, the three schemes exhibit comparable performance with no clearly superior one emerging. The errors are not monotonic with decreasing grid spacing. However, the locations of the quantities u_{max} and v_{max} tend to vary with change in the grid spacing indicating that they may not be accurate indicators of grid independent solutions. Nevertheless, Fig. 3.15 clearly shows that a mixed treatment utilizing the second order upwind scheme for the momentum equations and the hybrid scheme for the energy equation yields comparable performance with the second order central difference scheme.

The hybrid scheme automatically switches from a central difference to a first order upwind scheme at a cell Peclet number of 2. The cell Peclet numbers are defined as,

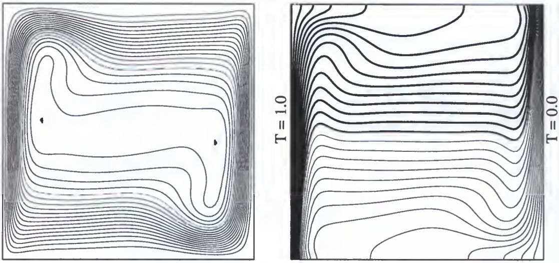

(a) Streamfunction: max: –17.0, min: 0.0, $\Delta\Psi = 0.9$. The extrema are marked with black dots.

(b) Isotherms: min: 0.0 max: 1.0 $\Delta T = 0.034$. Contour values higher than or equal to T = 0.5 are shown with thick lines.

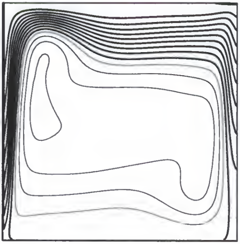

(c) Heat function. min: –9.0 max: 9.0 $\Delta H = 0.9$. Contour values greater than or equal to 0.0 have been thickened.

Figure 3.14 Natural convection in a square cavity. Solutions for Ra = 10^6 and Pr = 0.71. (a) Streamfunction (b) Isotherms (c) Heat flux

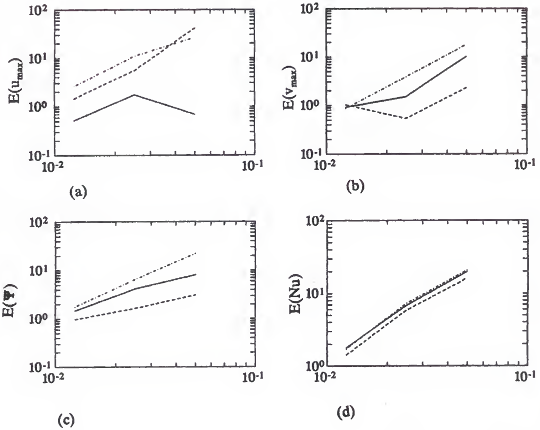

Figure 3.15 Percentage error in solution versus grid spacing, h.
(a) u_{max} (b) v_{max} (c) Streamfunction (d) Nusselt number

Key:

———————	Central difference
- - - - - - - - -	Mixed treatment
— · — · — · — ·	Second order upwind

$$\begin{aligned} Pe_u &= \varrho C_p u \Delta y / k \\ Pe_v &= \varrho C_p v \Delta x / k \end{aligned} \tag{3.2}$$

and their contours are shown in Fig. 3.16. It has also be observed that if the cell Peclet number is greater than 2 and the solution gradients are sharp, then the central difference solutions may be wiggle–free yet inaccurate (Shyy et. al. 1992). A good measure of the solution gradients are the cell Peclet numbers based on Δu and Δv rather than u and v. Contours of the cell Peclet number based on Δu and Δv are also shown in Fig. 3.16. It can be observed that, on the 81 × 81 grid, Pe_u is less than 1.6 over the entire domain indicating that the central difference scheme is used for the u–momentum equation whereas Pe_v exceeds 2 in the vertical boundary layers close to the isothermal walls indicating that the first order upwind scheme is used in the v momentum equations inside the vertical boundary layers. It should be noted that on the coarser grids, the hybrid scheme will switch to the first order upwind scheme in the boundary layer regions due to the higher values of Δx and Δy. Nevertheless, Fig. 3.16 indicates that for all grid spacings tested, the use of the lower order convection treatment in the energy equation does not degrade the solution accuracy.

Thus, it is clearly established that

(i) the second order upwind scheme yields satisfactory solutions, and

(ii) an apparently lower order combination of schemes consisting of second order upwind for the momentum equations and the hybrid scheme for the energy equation can produce satisfactory results for this problem.

3.3 Transient Natural Convection in an Enclosure

In the following, the present numerical method will be further validated in the context of a transient natural convection flow relevant to electronics cooling. In the literature, two generic problem types have been extensively investigated; the enclosure and the open cavity. Flows within enclosures are bounded on all sides by walls, whereas open cavities, such as vertical parallel plate channels or tubes, have their ends open to the ambient flow. An extensive discussion of important heat transfer results pertaining to such configurations has

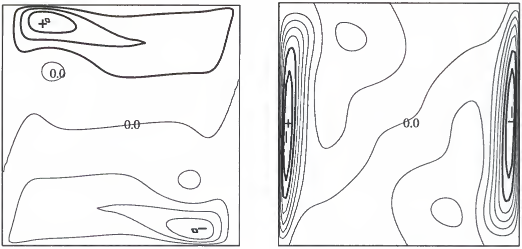

(a) Cell Peclet numbers based on u. min: –1.6 (–) max: 1.6 (+) $\Delta Pe_u = 0.4$.

(b) Cell Peclet numbers based on v. min: –2.8 (–) max: 2.8 (+) $\Delta Pe_v = 0.7$. Contour values less than –2 or greater than 2 have been thickened.

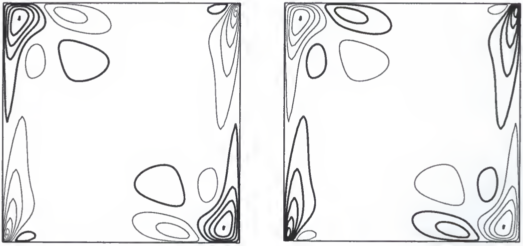

(c) Cell Peclet numbers based on Δu. min: –0.22 max: 0.18 $\Delta Pe_{\Delta u} = 0.04$. Contour values greater than or equal to zero have been thickened.

(d) Cell Peclet numbers based on Δv. min: –0.18 max: 0.22 $\Delta Pe_{\Delta v} = 0.04$. Contour values greater than or equal to zero have been thickened.

Figure 3.16 Contours of cell Peclet number.
(a) based on u (b) based on v (c) based on Δu (d) based on Δv.

been presented by Raithby and Holland (1985), Gebhart et al (1988) and Peterson and Ortega (1990).

The first experimental investigation of natural convection of air in isothermal, parallel–plate channels was carried out by Elenbaas (1942). By analyzing a simplified set of equations, and fitting experimental results, a correlation for the Nusselt number was obtained against Ra^* where $Ra^* = Ra\ d/L$ is the Elenbaas Rayleigh number, Ra is the Rayleigh number based on channel half width, d is the half width of the channel and L is its height. The experiments spanned the range $0.1 < Ra^* < 10^5$. Subsequent investigations by Sparrow and Bahrami (1980) showed inaccuracies in the data of Elenbaas at low values of Ra^* and they observed that the corrections employed by Elenbaas for extraneous heat losses, like radiation, exceeded the actual natural convection heat transfer; they and Martin et al (1991) have improved Elenbaas's correlation for the isothermal parallel plate channel.

Isothermal, asymmetrically heated, vertical parallel–plate channels have been investigated by Sparrow et al (1984). In this study, one wall was isothermal while the other was unheated. The experiments, carried out in water, with Pr = 5, revealed a pocket of recirculating flow adjacent to the unheated wall, close to the downstream end of the channel. In spite of this recirculating zone, the Nusselt number correlated well with the parameter $(2d/L)\ Ra$ where 2d is the inter–wall spacing. They also complemented the experimental results with numerical solutions based on parabolic equations, derived by neglecting the streamwise second derivatives. Thus, they concluded that the Nusselt number is relatively insensitive to the backflow. Sparrow and Azevedo (1985) followed up this study by investigations over a greater range of inter–wall spacing. They were able to obtain a correlation for the Nusselt number against $(2d/L)\ Ra$ over a wide range spanning the fully developed limit and the flat plate limit. They found that the flat plate limit does not form an upper bound on the heat transfer results. They also concluded that the Nusselt number is insensitive to 3–D effects.

Experiments have also been performed for iso–heat–flux plates by Wirth and Stutzman (1982) for the symmetrically heated case and by Webb and Hill (1989) for the asymmetrically heated plates. Correlations were presented for the average Nusselt number, local Nusselt number and the maximum temperature on the plates, as a function of the Rayleigh number. The results were in reasonable agreement with the previous numerical work of Aung (1972), for the limit of fully developed flow, and Aung et. al. (1972) for developing flow.

Theoretical investigation of free convection between parallel–plates was first undertaken by Bodoia and Osterle (1962). They solved the finite difference form of the parabolic equations, and obtained good agreement with the data of Elenbaas except at low values of the Grashof number, which they attributed to side leakage effects. However, they confined their analysis to the slot region, neglecting the effects of inflow and outflow boundaries.

In order to resolve the flow profile at the inlet, Kettleborough (1972) solved the laminar, 2–D Boussinesq equations for air with $Pr = 0.7$, $Gr = 12.5$ and 1250, and on a domain with an aspect ratio, AR of 5 that included an upstream entrance region. He however, imposed fully developed conditions at the channel exit, which is a restrictive assumption. A similar analysis was carried out by Nakamura et. al. (1982) with the difference that the wall boundary condition for the streamfunction was obtained by consideration of the pressure drop along the channel wall. Their results were significantly different from those of Kettleborough, especially at higher Grashof number. Also they could not capture the reverse flow region predicted by Kettleborough.

Chang and Lin (1989) performed a transient analysis which ultimately ended in steady state. Calculations were carried out for $Pr = 0.7$, $10^3 < Ra < 10^6$, and $AR = 5, 10$. The inlet and exit domains were considered in the analysis. However, they replaced the 180^o turn at the slot inlet and exit with an artificial 90^o adiabatic corner. They presented the time evolution of the flow and thermal fields and also a correlation for the Nusselt number as a function of the Rayleigh number and the channel aspect ratio, for air. At the free surfaces they prescribed the following boundary conditions; normal gradient of all velocities were zero at the free surfaces, normal gradient of temperature was zero if, locally, the fluid flowed out of the domain, otherwise, the temperature was set equal to the ambient temperature.

Naylor et al (1991) have solved the steady 2–D Navier–Stokes equations with consideration of the inlet domain. They also replaced the 180° turn at the inlet and outlet with an artificial 90° adiabatic corner. The inflow boundary was a semicircle and the boundary conditions were obtained from considerations of Jeffrey–Hamel flow which is a similarity solution of isothermal flow due to a sink at the point of intersection of two walls. Fully developed flow conditions were imposed at the slot exit. They also, for comparison purposes, solved the parabolic equations. Their solutions are in closer qualitative agreement with those of Nakamura et al (1982) than with Kettleborough (1972), but the overall quantitative agreement with either is quite poor. Reverse flow predicted by Kettleborough was not obtained.

Shyy et al (1992) carried out calculations modelling both the inflow and the outflow domains. The inflow domain had an upstream boundary condition amounting to that generated by a virtual line mass source located at the centerline of the inlet, and whose side boundaries were modelled by side entrainment boundary conditions. For the outflow region, the downstream boundary corresponded to the plume solution generated by a virtual line heat source located at the inlet centerline. The source/sink strengths were determined by matching the total convective energy transported across each boundary with the thermal energy conducted from the plates to the fluid. For the side entrainment boundaries, the normal derivatives of the velocity components were set to zero and the normal derivative of the temperature was set to zero, if the fluid flowed out of the domain; otherwise, the temperature was set equal to the ambient temperature. Calculations were carried out for Gr $= 10^3$, 10^4 , 10^5 and for AR = 1 , 2. For channel aspect ratio of unity, and at the Grashof numbers studied, a recirculation zone was observed in the slot.

Ramanathan and Kumar (1991) tried to circumvent the problem of artificial outflow and inflow boundary conditions by putting the slot within a large, isothermal enclosure. Iso–heat–flux boundary conditions were applied to the side of the heated plates facing the interior of the channel. The sides facing the enclosure were insulated. The problem is difficult to solve parametrically; apart from the usual Ra, Pr, and channel AR , there are five more geometric parameters. They found that their results were sensitive to the relative location of the slot in the vertical direction. In order to extrapolate their results to the limit of infinitely large enclosures, the temperatures within the slot were offset by the entry temperature at the inlet centerline. The steady 2–D Navier–Stokes equations, incorporating the Boussinesq approximation, were employed for the computations. They obtained good agreement with the experimental results of Wirth and Stutzman (1982) for Ra = 18.8, 191, and 2414. Correlations were presented for maximum temperature on the plates and for the average Nusselt number versus the Rayleigh number and channel aspect ratio, for air. They also found that for fluids with $\mathrm{Pr} > 0.7$, the hydrodynamic development length is smaller than the thermal development length up to Ra = 400 and for $\mathrm{Pr} < 0.1$, the opposite holds. They concluded that vertical diffusion of energy cannot be neglected, especially for low Pr and short AR channels.

Thus it is seen that various investigators, in the attempt to compute natural convection heat transfer between two vertical plates have formulated various boundary conditions to deal with the artificial boundaries of a finite computational domain. The results are also as varied. The heat transfer results seem to correlate well with parameters obtained by neglecting streamwise diffusion, yet, in terms of the velocity field, recirculating flows have been found within the slot, which is incompatible with the boundary layer assumption. Attempts have been made to solve the full elliptic equations with the fully developed boundary conditions at the channel exit, which is restrictive and has been found unsatisfactory by other investigators.

Despite the fact that most investigators have dealt with the flow between two parallel plates in an open domain, many practical applications, especially in the electronics industry, have geometrical configurations similar to the one in this study, as shown in Fig 3.17. For example, as discussed by Gingrich et al (1992), an electronics cooling cabinet often adopts such a generic design where hot plates are placed in the middle of the enclosing cabinet. Such geometries, however, involve several independent geometrical parameters and it may not be feasible to conduct parametric investigations over the entire range of possible values, especially if the transient effects are of interest. Recently, interest has arisen in the use of non–Newtonian fluids in electronics cooling applications (Gingrich et al 1992), which, however, is outside the scope of the current study.

A discussion of the present contribution relative to the previous efforts is in order. In Shyy et. al. (1992), not only were the computations conducted for an open channel, but more importantly, there was a major issue in terms of prescribing the boundary conditions for that configuration. As discussed in that paper, there is a fundamental difficulty in determining the overall incoming and outgoing mass fluxes and their distributions, for an open channel flow, unless some simplifications are made in the problem formulation. That is the rationale behind deriving the line–source and the plume solutions for the inlet and outlet conditions respectively. A detailed account of this issue can be found in Shyy et. al. (1992). There is a need to understand the way of extending the theoretical framework from a confined enclosure to that of an open domain, and the correct approach has yet to be identified. The configuration chosen here represents a more realistic case in the area of electronics cooling. Furthermore, the present work is a simulation of transient heat transfer, whereas the work of Shyy et. al. (1992) is a steady state formulation.

The current study consists of two isothermal vertical parallel plates placed within a rectangular enclosure. The top and bottom walls of the enclosure are insulated, whereas the side walls are isothermal, as shown in Fig 3.17. The geometrical parameters are held constant and have the values $X_{max}/2d = 4$, $Y_{max}/2d = 3$, $L_1/2d = 1.5$ and

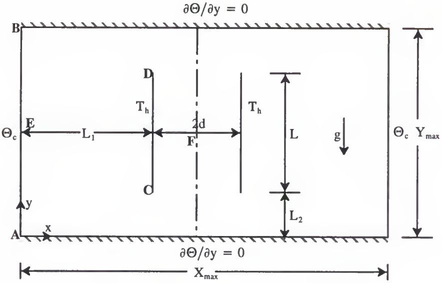

Figure 3.17 Schematic of present problem with a heated vertical channel inside a cold rectangular enclosure. The hatched lines indicate adiabatic walls. The domain is symmetric about the vertical centerline. The side walls of the enclosure and the channel walls are isothermal. The letters A,B indicate the vertical extent of the enclosure wall. Similarly, the letters C,D designate the vertical extent of the channel wall.

$L_2/2d = 1$. Initially there is no convection and uniform temperature prevails. At time t = 0, the plates experience a step change in the temperature. A Grashof number of 10^5, typical of electronic devices, is considered in our work. The present study attempts to accurately capture the detailed flow and thermal structures of the transient, two–dimensional buoyancy induced flowfield and associated heat transfer results. Thus, care has been taken to ensure adequate numerical accuracy in both time and space. Also reasonable for the Navier–Stokes flow fields, is the Boussinesq approximation, which has been employed here. The main motivation of the work is to utilize a set of accurate transient simulations to facilitate a detailed scrutiny of the development of the flow and heat transfer characteristics, yielding improved insights in important practical problems.

3.3.1 Formulation and Solution Procedure

The non–dimensionalized, unsteady, two–dimensional, Navier–Stokes equations incorporating the Boussinesq approximation can be written as:

Continuity:
$$\frac{\partial \hat{u}}{\partial x} + \frac{\partial \hat{v}}{\partial y} = 0 \tag{3.3}$$

x–momentum:
$$\frac{\partial \hat{u}}{\partial t} + \frac{\partial \hat{u}^2}{\partial x} + \frac{\partial \hat{u}\hat{v}}{\partial y} = -\frac{\partial p}{\partial x} + \Pr\left[\frac{\partial^2 \hat{u}}{\partial x^2} + \frac{\partial^2 \hat{u}}{\partial y^2}\right] \tag{3.4}$$

y–momentum:
$$\frac{\partial \hat{v}}{\partial t} + \frac{\partial \hat{u}\hat{v}}{\partial x} + \frac{\partial \hat{v}^2}{\partial y} = -\frac{\partial p}{\partial y} + \Pr\left[\frac{\partial^2 \hat{v}}{\partial x^2} + \frac{\partial^2 \hat{v}}{\partial y^2}\right] + \mathrm{Ra}\ \Pr\ \hat{T} \tag{3.5}$$

Energy:
$$\frac{\partial \Theta}{\partial t} + \frac{\partial(\hat{u}\Theta)}{\partial x} + \frac{\partial(\hat{v}\Theta)}{\partial y} = \frac{\partial^2 \Theta}{\partial x^2} + \frac{\partial^2 \Theta}{\partial y^2} \tag{3.6}$$

The dimensionless variables are defined by Eq. (2.5), where the reference scales are d, the half channel width, the velocity scale $U_r = \alpha/d$, α, the thermal diffusivity, and the time scale $\tau_r = d^2/\alpha$. The Boussinesq approximation involves the assumption that density variations are small enough to be neglected everywhere except in the buoyancy source term in the Y–momentum equation. All other fluid properties such as viscosity, thermal conductivity and specific heat are assumed constant.

The solution methodology involved the use of the second order central differences for discretization of all spatial derivatives, including the convection terms, and the first order, implicit, backward Euler scheme for the time derivatives. The resulting algebraic equations were iterated till a desired accuracy was achieved. The SIMPLE algorithm, Patankar (1980), which is a semi–implicit pressure correction based approach, was used for the iteration procedure at each time step. The following quantities were monitored at each time step: (i) heat flux from the heated plates, (ii) heat flux out of the enclosure wall, and (iii) volume flux through the channel. These quantities were nondimensionalized as:

$$\mathrm{Nu}_c = \frac{d}{2L} \int_{L_2/d}^{(L_2+L)/d} \left[\frac{\partial \Theta}{\partial x}\bigg|_{x=xp_+} + \frac{\partial \Theta}{\partial x}\bigg|_{x=xp_-} \right] dy \tag{3.7}$$

where $xp = L_1/d$ is the non–dimensional x–location of the heated plate under consideration

$$Nu_c = \frac{d}{Y_{max}} \int_0^{Y_{max}/d} \frac{\partial \Theta}{\partial x}\Big|_{x=0} dy \qquad (3.8)$$

where x = 0 defines the cold enclosure wall, and

$$Q = \int_{L_1/d}^{(L_1+L)/d} \hat{v}\,|_{y=y_k}\ dx \quad , \qquad L_2/d \le y_k \le (L_2 + L)/d \qquad (3.9)$$

where y_k is any y–location within the channel region.

The temperature gradients at the walls were evaluated by one–sided finite differences at the walls. The integrals were evaluated by assuming a piece–wise constant distribution of the dependent variables within each control volume, which is consistent with the discretization procedure. The heat flux distribution on the isothermal walls can be described as a local Nusselt number:

$$Nu+ = \frac{\partial \Theta(y)}{\partial x}\Big|_{x=xp+} \qquad Nu- = \frac{\partial \Theta(y)}{\partial x}\Big|_{x=xp-} \qquad Nu = \frac{\partial \Theta(y)}{\partial x}\Big|_{x=0+} \qquad (3.10)$$

where xp is the x–location of the heated plate, and x = 0 defines the cold enclosure wall. Calculations were carried out for a Grashof number, Gr = 10^5, and channel aspect ratio, AR = 1. Other geometrical parameters were also held constant.

Initial computations were carried out on a coarse grid of 60 × 60 control volumes and a fine grid of 90 × 90 control volumes, with a time step (nondimensional) $\Delta t = 10^{-2}$. The grid spacing was adjusted by a cubic polynomial, with the grid spacing specified at the two ends. The coarse grid had 30 control volumes between the enclosure wall and the channel wall, in the x –direction, with $\Delta X/2d = 10^{-3}$ at the channel wall and 10^{-2} at the enclosure wall and 30 control volumes between the channel wall and the channel centerline. In the y – direction, there were 15 control volumes between the bottom enclosure wall and the channel inlet, 20 control volumes in the channel region and 25 control volumes between the channel outlet and the enclosure top wall. The grid spacing was $\Delta Y/2d = 10^{-3}$ at the channel inlet and outlet and 10^{-2} at the enclosure wall. The corresponding parameters for the fine grid were $\Delta X/2d = 5 \times 10^{-4}$ at the channel wall and 5×10^{-3} at the enclosure wall, with 50 control volumes in the x –direction between the enclosure side walls and the channel walls, and 40 control volumes between the channel wall and the channel centerline. In the y – direction, the parameters were $\Delta Y/2d = 5 \times 10^{-4}$ at the channel inlet and outlet, and 5×10^{-3} at the enclosure top and bottom walls. There were 20 control volumes in the region between the bottom enclosure wall and the channel inlet, 30 control volumes in the channel region, and 40 control volumes in the region between the channel outlet and the top enclosure wall. Symmetry boundary conditions:

$$\hat{u} = 0 \, , \; \frac{\partial \hat{v}}{\partial x} = 0 \, , \; \frac{\partial \Theta}{\partial x} = 0 \tag{3.11}$$

were applied at the channel centerline and the calculations were carried out for half the domain, thereby achieving good spatial resolution along with economy of storage and CPU time. At each time step, the algebraic equations were iterated until the normalized residuals obtained by summing, over the whole domain, the absolute values of the mass, momentum and energy flux imbalances within each cell, were within 10^{-3}.

3.3.2 Results and Discussion

Initially, a time step, $\Delta t = 10^{-2}$ was chosen and the calculations advanced up to 300 time steps. At that point, the calculations converged in less than 3 iterations per time step. At that time instant, the heat balance within the domain was within 0.6% for the coarse grid and 0.4% for the fine grid, yielding a difference of less than 0.2% between the two solutions. The iterative calculation procedure at a given time step was terminated when the normalized residual, for each dependent variable, was less than 10^{-3}. The residual for any given dependent variable is computed by summing over the absolute values of the relevant flux imbalances in each control volume over the entire computational domain. The residuals are then normalized with respect to characteristic quantities obtained from the reference scales defined previously. For example, the mass imbalance in the domain is non–dimensionalized with respect to the total mass in the enclosure. From Fig. 3.18 it can be observed that the above comparisons hold true over the entire time history. It was clear that grid independence

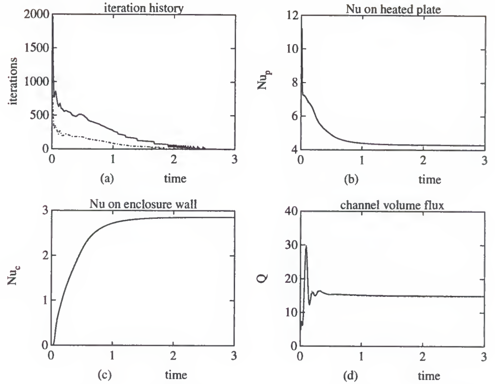

Figure 3.18 Comparison of calculations on the 61 x 61 grid versus the 91 x 91 grid. $\Delta t = 10^{-2}$ for both cases.
(a) Number of iterations for convergence at each time step.
(b) Nusselt number, Nu_p, based on heat flux through channel wall.
(c) Nusselt number, Nu_c, based on heat flux through enclosure wall.
(d) Nondimensional volume flux through channel, Q.
Key: ——— 91 x 91 grid .... 61 x 61 grid.

had been achieved. However, to maintain adequate computational accuracy, the fine grid was used for all further calculations.

To verify the time step independence of the solution, a computation was conducted for $\Delta t = 10^{-4}$ and marched up to 10^4 time steps. Figure 3.19 summarizes some of the key findings in terms of the monitored quantities. At time t = 1.0, the differences between the two solutions are within 0.2% for the heat flux from the heated plates, 0.3% for the heat flux out of the enclosure walls and 0.1% for the volume flux through the channel. However, at intermediate time, i.e., $0.01 < t < 0.6$, there are significant differences between the solutions. For the Nusselt number based on heat flux from the channel wall, Nu_p, the

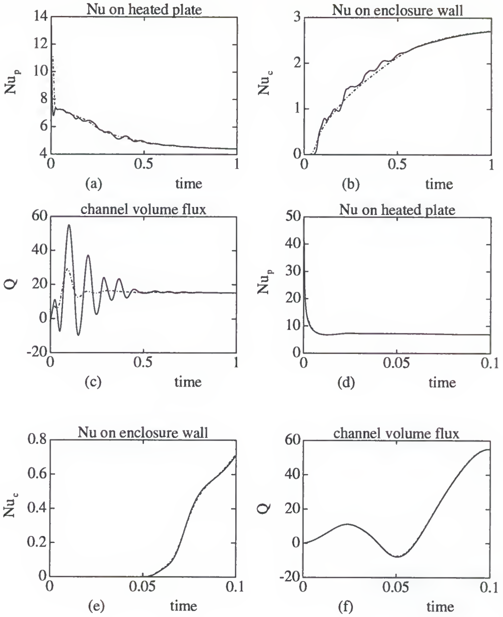

Figure 3.19 Comparison of calculations with (a–c) $\Delta t = 10^{-2}$ and $\Delta t = 10^{-4}$ on the 91 x 91 grid and (d) – (f) $\Delta t = 10^{-4}$ and $\Delta t = 10^{-5}$ on the 91 x 91 grid.

(a) Nusselt number, Nu_p, based on heat flux through channel wall.
(b) Nusselt number, Nu_c, based on heat flux through enclosure wall.
(c) Nondimensional volume flux through channel, Q
(d) Nusselt number, Nu_p, based on heat flux through channel wall.
(e) Nusselt number, Nu_c, based on heat flux through enclosure wall.
(f) Nondimensional volume flux through channel, Q

(a) – (c) Key: ——— $\Delta t = 10^{-4}$, - - - - - - $\Delta t = 10^{-2}$
(d) – (f) Key: ——— $\Delta t = 10^{-5}$, - - - - - - $\Delta t = 10^{-4}$

differences are negligible throughout the time history, but for the Nusselt number based on heat flux out of the enclosure walls, Nu_c, there are noticeable quantitative and qualitative differences. For the volume flux, Q, the solutions corresponding to each of the two time steps are profoundly different. The solution corresponding to $\Delta t = 10^{-2}$ shows a highly damped oscillatory trend, extending up to $t \sim 0.3$, but does not show net mass flow reversal through the channel. But the solution corresponding to $\Delta t = 10^{-4}$ shows oscillations of much larger amplitude showing net mass flow reversal through the channel. The amplitude reaches a maximum at about $t \sim 0.1$ and the oscillations are damped to their steady state value at about $t \sim 0.6$. The peak–to–peak average also displays an oscillatory tendency. The solutions also differ in phase. As an explanation, it is recalled that the backward Euler is first order in time and prone to numerical damping. As a check on the solution accuracy, a computation was initiated with $\Delta t = 10^{-5}$ and advanced up to 10^4 time steps. Figure 3.19 shows no discernible differences in the solutions corresponding to $\Delta t = 10^{-4}$ and $\Delta t = 10^{-5}$, indicating that the solution is independent of the value of Δt.

It is noted that the solution corresponding to $\Delta t = 10^{-4}$ was marched up to 10^4 time steps, i.e., $t = 1.0$. From a comparison with the steady state solution obtained with $\Delta t = 10^{-2}$, it is seen that steady state cannot be achieved at $t = 1.0$. But the differences, in terms of the monitored quantities are quite small, less than 2.6% for Nu_p, 5% for Nu_c and 1% for Q. The fine time step calculations are expensive in terms of computer time. The solution corresponding to $\Delta t = 10^{-4}$ and 10^4 time steps took about 1.5 days of CPU time on a DECstation 5000. Since the steady state solution can be obtained by using $\Delta t = 10^{-2}$ or higher, the calculations were terminated at this stage. All further discussion applies to the transient solution corresponding to $\Delta t = 10^{-4}$.

Figure 3.20 shows the distribution of the local Nusselt number on the heated channel walls. The solid line shows the Nusselt number, Nu+, based on the heat flux from the plates to the interior of the channel and the broken line the Nusselt number, Nu–, based on the heat flux from the heated plates to the exterior of the channel. The quantities Nu+ and Nu– are

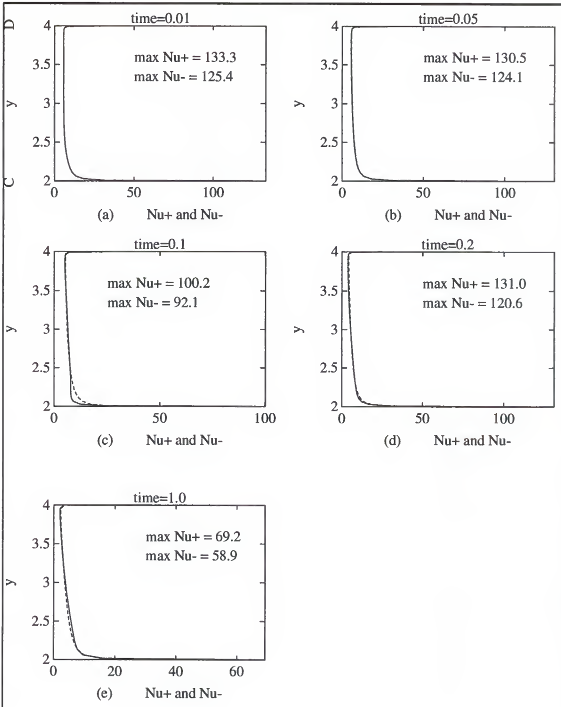

Figure 3.20 Time evolution of Nusselt number distribution on the inner (Nu+) and outer (Nu–) channel wall as defined in Eq. (3.8). The letters C and D designate the channel wall at $2d \leq Y \leq 4d,\ X = 1.5d$, as shown in Fig. 3.1.

Key: ——— Nu+, based on heat flux to channel interior

- - - - - Nu–, based on heat flux to the open side.

defined in Eq. (3.10). These are established early in time and do not vary significantly thereafter. Notably, these are relatively insensitive to the oscillations in the net volume flux through the channel, Q, as will be discussed later in connection with the detailed analysis of the flow and thermal structures in the slot.

Figure 3.21 shows the local Nusselt number distribution, Nu as defined in Eq. (3.10), on the enclosure walls. Initially, there is a spike–like distribution established near the top, as the heated fluid reaches that location. Gradually, it broadens as the convection field develops and increases in magnitude and at large time, it has a triangular distribution

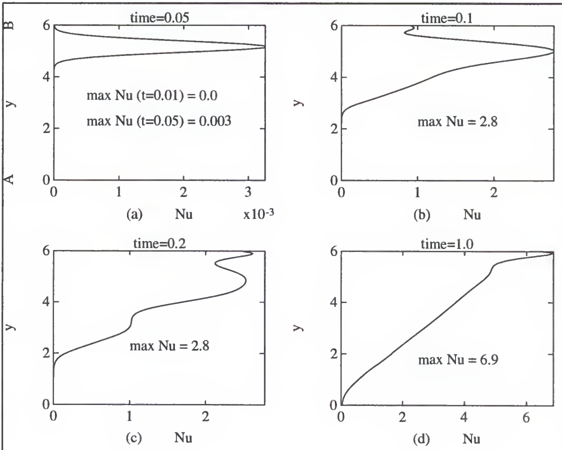

Figure 3.21 Time evolution of the Nusselt number distribution on the enclosure wall, Nu as defined in Eq. (3.8). The letters A and B refer to the vertical extent of the enclosure wall at $0 \leq Y \leq 6d$, $X = 0$, as shown in Fig. 3.1

resulting from the fact that the convection field moves towards the top part of the enclosure side–wall and moves away from its bottom part.

Figure 3.22 shows the streamlines, isotherms and contours of motion pressure at t = 0.01, 0.05, 0.1, 0.15, 0.2 and 1.0. Physically, at the early stages of the transient process, heat transfer from the heated plates to the fluid amounts to a conduction process (Gebhart et al. 1988); buoyancy induced motion arises, but convective effects on the heat transfer process are absent. This phenomenon is however, present only for a short time during the startup of the transient. At any location, the conduction effect ends with the arrival of the leading edge effect. Thereafter, the process is multi–dimensional and the transient process continues towards a steady state. Thus it is evident, from the streamlines and the isotherms, that time t = 0.01 depicts the end of the one dimensional conduction process. The flow adjacent to the channel walls consists of a thin layer of heated fluid moving upward and has a structure qualitatively similar to a buoyancy driven boundary layer on a single isothermal vertical flat plate as can be observed from the v–velocity profiles across the middle of the channel, depicted in Fig 3.23. It is evident from Fig. 3.23 that in the course of the transient evolution while the v–velocity reverses in sign in the regions away from the heated plates, adjacent to the plates it exhibits only modest variations in magnitude and maintains its direction. Thus the flow structure near the channel walls is qualitatively insensitive to the flow in the rest of the channel. This particular flow feature, established early in the transient stages, persists till steady state, and shields the wall heat transfer process from the effects of the flow in the central region of the channel. This explains the relative insensitivity of the plate Nusselt number to the oscillating volume flux within the slot. At t = 0.05 large vortical structures can be seen both inside and outside the slot. The net volume flow rate in the channel, Q, is in the negative y direction. The isotherms show distorted shapes corresponding to the convection field in the vicinity of the recirculating flow structures.

At t = 0.1 there are many pockets of recirculating flow close to the enclosure walls and near its top. The net volume flux, Q, is directed upward and attains its global maximum

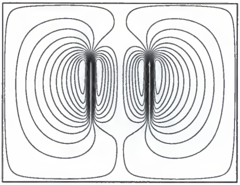

(a) streamlines: min: −12.13 (between plates) max: 21.15, ΔΨ: 1.664

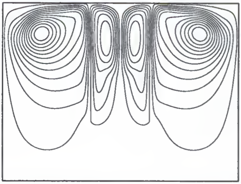

(a) streamlines: min: −12.13 (between plates) max: 21.15, ΔΨ: 1.664

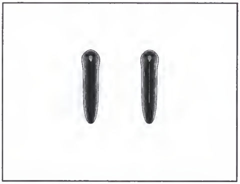

(b) isotherms: min: 0 max: 0.997183 ΔT: 0.0665

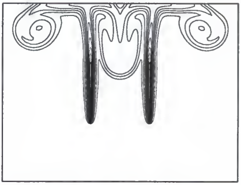

(b) isotherms: min: 0 max: 0.997255 ΔT: 0.0665

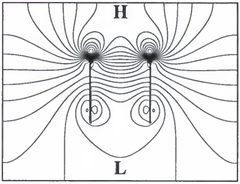

(c) motion pressure: ΔP: 421

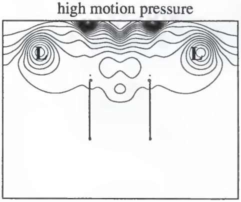

(c) motion pressure: ΔP: 2339

Fig. 3.6(i) t = 0.01

Fig. 3.6(ii) t = 0.05

Figure 3.22 Contour plots of the solution.

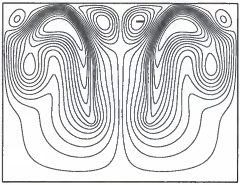

(a) streamlines: min: –37.92 (–), max: 90.25
ΔΨ: 6.41

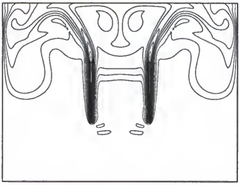

(b) isotherms: min: 0 max: 0.997488
ΔT: 0.0665

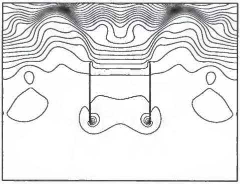

(c) motion pressure: ΔP: 1564

Fig. 3.6(i) t = 0.1

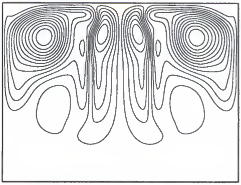

(a) streamlines: min: –52.53 (between plates)
max: 99.1, ΔΨ: 7.58

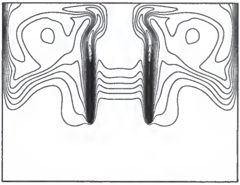

(b) isotherms: min: 0 max: 0.99786
ΔT: 0.0499

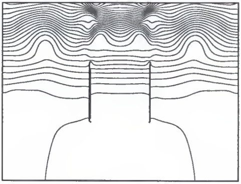

(c) motion pressure: ΔP: 2090

Fig. 3.6(ii) t = 0.15

Figure 3.22 — continued. Contour plots of the solution

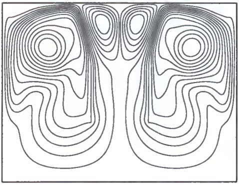

(a) streamlines: min: –41.49 (above plates) max: 107.1, ΔΨ: 7.43

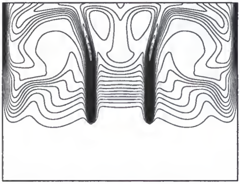

(b) isotherms: min: 0 max: 0.998157 ΔT: 0.0333

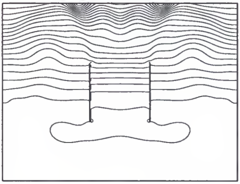

(c) motion pressure: ΔP: 3229

Fig. 3.6(i) t = 0.2

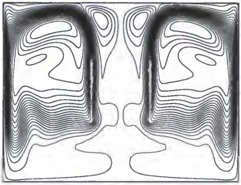

(a) streamlines: min: –8.49 (above plates) max: 41.64, ΔΨ: 1.671

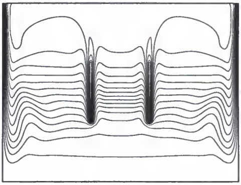

(b) isotherms: min: 0 max: 0.998983 ΔT: 0.0499

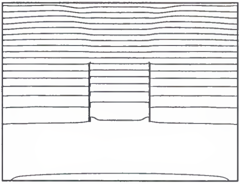

(c) motion pressure: ΔP: 6824

Fig. 3.6(ii) t = 1.0

Figure 3.22 — continued. Contour plots of the solution

value. It is noted that vorticity generation occurs in the flow field as explained by the fact that the equation of vorticity transport has a source term proportional to $\partial T / \partial x$, the physical origin of which lies in the baroclinicity of the flowfield. The isotherms in the channel show a strong tendency to become horizontal and the temperature increases in the positive y direction.

At $t = 0.15$, there is a net downward volume flux, Q, in the channel. Many recirculating flow structures persist, although the tendency to decay by viscous action is evident. The isotherms in the center of the slot are horizontal and increasing in the positive y direction. It is observed that the motion pressure contours are normal to the plates and to the sidewalls of the enclosure, i.e, $\partial P / \partial x$ is negligible in the slot and near the sidewalls of the enclosure. At $t = 0.2$, the net volume flux is upward, and attains a local maximum, but the other trends described for the previous case continue. At $t = 1.0$ the solution approaches the steady state solution. At this time, viscous action results in the decay of several of the vortices and many of the recirculating flow structures coalesce. There are two counter rotating vortices near

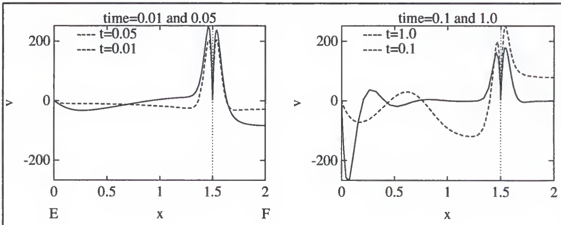

Figure 3.23 v–velocity profiles along a horizontal line at the center of the domain, i.e., along $y = 1.5$. The dotted line shows the location of the heated plate. Only the left half of the domain is shown. The profiles clearly show the existence of a thin wall layer adjacent to the heated channel walls. The letters E and F correspond to the physical locations shown in Fig. 3.1.

the top wall of the enclosure and these extend downward into the slot region. It is also noted that the motion pressure variation in the x–direction is negligible.

A qualitative comparison of the current results can be made against the results of Chang and Lin (1989). They have presented detailed studies of the flow and thermal structures for the case of $Pr = 0.7$, $Ra = 10^4$, $AR = 5$. A monotonic variation of the flow characteristics up to steady state, especially the recirculating cells in the early stages of the transient, was obtained, as opposed to the current results, where, an oscillatory volume flux, decaying to steady state can be observed. However, in the heat transfer results, notably, the Nusselt number, they recorded an undershoot in the time evolution of the Nusselt number. In the current calculations, the Nusselt number decays monotonically to the steady state and no undershoot can be observed. Also, Chang and Lin (1989) did not obtain recirculating flow in the channel at steady state, probably due to the higher aspect ratio channel used in their calculations. The recirculating flow observed at steady state, in the present case, is qualitatively consistent with the results obtained by Shyy et al (1992) for their case of $Pr = 0.71$, $Gr = 10^5$, $AR = 1$. Low Ra cases have been presented by Ramanathan and Kumar (1991), where, no backflow was found. They have also presented a case for $Ra = 10^5$, for which they have not presented the complete details of the flow and thermal fields. However, they show that the temperature distribution along the channel walls were qualitatively consistent with the similarity solution of Sparrow and Gregg (1956). This agreement with a theoretical prediction based on the parabolic equations implies the absence of recirculating flow in the channel, in their case.

3.4 Steady Thermocapillary Convection in a Liquid Bridge

Apart from buoyancy, the other important physical mechanism found in many crystal growth processes is capillarity resulting from a free surface. The formulation aspects of the float zone free surface have been presented in chapter 2. A major goal of the present thesis is to simulate the complete crystal growth process in a float zone. Such a task will be presented in chapter 5 after the phase change aspect has been addressed. In the following, thermocapillary convection in a liquid bridge has been conducted. Such a liquid bridge illustrated in Fig. 3.24(a) may be considered as a model for the study of convective heat transfer mechanisms in the float zone crystal growth process. The most influential factors on the crystal quality and process economics are the heat and solute transport processes in the melt, which control the morphology and movement of the solidifying front. In the following study, a configuration frequently encountered in practical float-zone processes is isolated for detailed analysis of heat transport within the melt. Of particular interest is the role of buoyancy-driven and thermocapillary convection processes and the interaction of these processes with the shape of the free surface in determining the heat transfer within the melt. The Navier-Stokes equations, along with the energy equation are written in cylindrical coordinates to facilitate the treatment of the axisymmetric geometry shown in Figure 3.24(b). The numerical scheme involves the discretization of the transformed form of the governing equations based on a control volume formulation as described earlier in chapter 2. The free surface shape is chosen so as to satisfy the static force balance between the hydrostatic pressure of the melt and surface tension forces generated due to the presence of the free surface between the melt and the ambient gas. The details of the integration of the Young–Laplace equation to arrive at an equilibrium shape of the free surface have been considered previously in chapter 2.

3.4.1 Scaling, Nondimensionalization and Governing Equations

An appropriate choice of scales for the nondimensionalization procedure is arrived at by selecting the base radius r_b as the characteristic length scale and the thermal diffusion velocity scale, defined as α/r_b, where α is the thermal diffusivity. The selection of the temperature scale is not as straightforward because the boundary condition at the free surface is specified as a heat flux from which an estimate of the maximum temperature in the domain has to be derived. The procedure is explained below in detail. Since the heat flux is specified on the free surface, a temperature scale has to be derived in order to nondimensionalize the energy equation and to define the Grashof and the Marangoni numbers. It would seem natural to define a temperature scale based on the heat flux

$$\Delta T = \frac{q_{max}}{k} r_b \tag{3.12a}$$

where q_{max} is the maximum value of the heat flux specified on the boundary. However, it has been observed that such a definition consistently overestimates the temperature scale, that is, the maximum temperatures achieved in the domain, even for conduction cases, are of the order of five times less than the value suggested by Eq. (3.12a). In addition, it is expected that the maximum temperatures obtained by taking convection into account should be even less. Therefore, the temperature scale obtained above will be scaled down by a factor of ten in order to obtain a more realistic temperature scale. Thus, the temperature scale used to calculate the Grashof and Marangoni numbers is:

$$\Delta T = 0.1 \times \frac{q_{max}}{k} r_b \tag{3.12b}$$

Regarding the convection mechanisms, the buoyancy effect within the melt and the thermocapillary effect on the free surface have been included in this model. The strength of buoyancy induced convection is indicated by the Rayleigh number, defined as

$$Ra = Gr \cdot Pr \tag{3.13a}$$

where Gr is the Grashof number,

$$Gr = \frac{g r_b^3 \Delta \varrho}{\nu^2 \varrho} \tag{3.2b}$$

Invoking the Boussinesq approximation, this becomes

$$Gr = \frac{g \beta_T \Delta T r_b^3}{\nu^2} \tag{3.14}$$

where Pr is the Prandtl number, as defined in Eq. (3.2c). The relative magnitude of the thermocapillary effect is described by the Marangoni number, Eq. (3.4). The governing equations may be nondimensionalized with respect to the reference scales developed in Eq.

(2.5) as follows:

(i) continuity:
$$\frac{\partial(R\tilde{u})}{\partial R} + \frac{\partial(R\tilde{v})}{\partial Y} = 0 \qquad (3.15a)$$

(ii) radial momentum:
$$\frac{\partial(R\tilde{u}^2)}{\partial R} + \frac{\partial(R\tilde{u}\tilde{v})}{\partial Y} = - R\frac{\partial P}{\partial R} + \Pr\left[\frac{\partial}{\partial R}\left(R\frac{\partial \tilde{u}}{\partial R}\right) + \frac{\partial}{\partial Y}\left(R\frac{\partial \tilde{u}}{\partial Y}\right)\right] - \Pr\frac{2\tilde{u}}{R} \qquad (3.15b)$$

(iii) axial momentum:
$$\frac{\partial(R\tilde{u}\tilde{v})}{\partial R} + \frac{\partial(R\tilde{v}^2)}{\partial Y} = - R\frac{\partial P}{\partial Y} + \Pr\left[\frac{\partial}{\partial R}\left(R\frac{\partial \tilde{v}}{\partial R}\right) + \frac{\partial}{\partial Y}\left(R\frac{\partial \tilde{v}}{\partial Y}\right)\right] + R\ \mathrm{Ra}\ \Pr\ \Theta \qquad (3.15c)$$

(iv) energy:
$$\frac{\partial(R\tilde{u}\Theta)}{\partial R} + \frac{\partial(R\tilde{v}\Theta)}{\partial Y} = \left[\frac{\partial}{\partial R}\left(R\frac{\partial \Theta}{\partial R}\right) + \frac{\partial}{\partial Y}\left(R\frac{\partial \Theta}{\partial Y}\right)\right] \qquad (3.15d)$$

Here $\tilde{u}$ and $\tilde{v}$ are the non–dimensional velocity components in the radial and axial directions, respectively and the reference length scale, d is set to r_b. The Boussinesq approximation is employed; thus, density variations are neglected in the governing equations, except for the buoyancy terms in the momentum equations. Only the right half of the domain is considered in the calculation procedure, and symmetry boundary conditions are applied at the centerline. The associated boundary conditions are listed below in nondimensional form:

symmetry:
$$\text{At } R = 0, \quad \tilde{u} = \frac{\partial \tilde{v}}{\partial R} = \frac{\partial \Theta}{\partial R} = 0 \qquad (3.16a)$$

top and bottom boundaries:
$$\text{At } Y = 0 \text{ and } 1: \quad \Theta = 0, \quad \tilde{u} = \tilde{v} = 0 \qquad (3.16b)$$

At the free surface; R = *f(Y)*:

(i) heat flux through the free surface (dimensionless) :
$$\vec{q} = \nabla\Theta \cdot \vec{n} \qquad (3.16c)$$

which equals the normal derivative of the temperature at the free surface, and $\hat{n}$ is the unit normal vector to the free surface.

(ii) Marangoni effect: $\nabla (\vec{V} \cdot \vec{t}) \cdot \vec{n} = \mathrm{Ma}\ \nabla\Theta \cdot \vec{t}$ (3.10)

where the shear stress equals the surface tension gradient and gives rise to the normal derivative of the tangential velocity at the free surface. $\vec{V}$ is the velocity vector, $\vec{n}$ is the unit normal vector to the free surface, and $\vec{t}$ is the unit tangent vector to the free surface.

(iii) kinematic condition at the free surface:

$$\vec{V} \cdot \vec{n} = 0 \tag{3.16d}$$

which specifies a no-penetration condition at the free surface.

3.4.2 Heat Transfer Calculations

A series of calculations was carried out with the geometry of the free surface as shown in Figure 3.24. The material selected for simulation is NiAl whose thermophysical properties of this material are listed in Table 3.1. If phase change effects are not considered, and the power input from the heater is 2.3×10^6 W/m^2, then the temperature scale can be obtained from Eq. (3.12b) as $\Delta T = 36.5$ K. For the length scale defined by $r_b = 1.25 \times 10^{-2}$ m as in the previous calculations for the meniscus shape, this temperature scale implies a Marangoni number of 10^3, a Grashof number of 520, and a Prandtl number of 0.04. These values vary with the composition of the NiAl. Nevertheless, it is clear that for the length scales under consideration, thermocapillary convection plays a dominant role in the heat transfer process. In the computations to follow, a range of nondimensional parameters,

$$0 \leq \mathrm{Gr} \leq 10^6, \quad 0 \leq \mathrm{Ma} \leq 10^3, \quad \text{and} \quad \mathrm{Pr} = 0.04,\ 0.1$$

have been considered for investigation.

3.4.3 Numerical Procedure

The governing equations (3.15) are solved using the pressure-correction formulation in nonorthogonal body-fitted coordinates. The convection and diffusion terms in both the momentum and energy equations are discretized using second order central differences. The

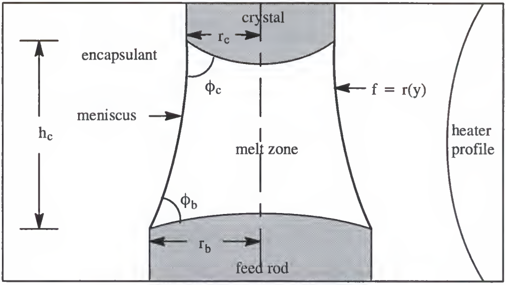

(a) Schematic of the float-zone process. The melt zone is sustained by the surface tension between the melt and the encapsulant. The heating profile is schematically illustrated in the right. Axisymmetry has been assumed.

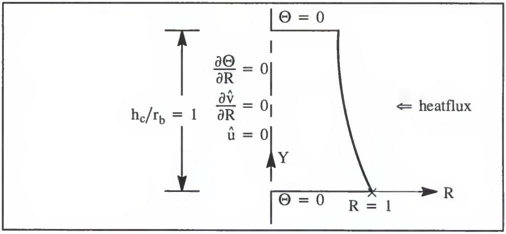
$\Theta = 0$
$\frac{\partial \Theta}{\partial R} = 0$
$\frac{\partial \hat{v}}{\partial R} = 0$
$h_c/r_b = 1$
$\hat{u} = 0$
⇐ heatflux
Y
R
$\Theta = 0$
$R = 1$

(b) Schematic of the mathematical model and geometry employed in the calculation procedure.

Figure 3.24 Schematic of the float-zone process and the mathematical model employed.

grid points were clustered towards the free surface and for the computations involving Marangoni convection, they also were clustered towards the lower boundary at Y = 0. For the cases involving natural convection only, two grid systems involving 81 × 52 nodes and 161 × 103 nodes, were used to discretize the domain. The solutions are indistinguishable, indicating grid independence. The solutions presented are based on the grid system involving 161 × 103 nodes for cases not involving Marangoni convection and 401 × 201 nodes for cases involving Marangoni convection

Table 3.1 Thermophysical properties of NiAl and process parameters

Density	6000 kg/m^3
Thermal conductivity	80 W/m-K
Heat capacity	586 J/kg-K
Coefficient of thermal expansion	1.51×10^{-5} K^{-1}
Kinematic viscosity	9×10^{-7} m^2/s
Surface tension coefficient	-2.7×10^{-4} N/m-K
Surface tension	1.35 N/m
Latent heat	5.1×10^5 J/kg
Melting point	1900 K
Gravitational acceleration	9.81 m/s^2

3.4.4 Heat Conduction

A calculation was carried out with the heat transfer taking place through conduction effects only. The purpose was to carry out an a posteriori verification of the temperature scales used to define the Grashof and the Marangoni numbers in subsequent calculations. It may be noted that due to the curved geometry of the free surface, the location of the maximum temperature shifts towards the convex portion of the free surface, as is evident from the region labelled B in Figure 3.25. The nondimensional value of Θ_{max} obtained here is 2.3 based on the temperature scale defined in Eq. (3.12b).

3.4.5 Natural Convection

Figure 3.26 shows the results of incorporating the effects of buoyancy induced convection with a Grashof number of 10^6 and a Prandtl number of 0.1. The streamline

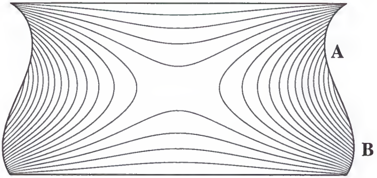

Isotherms: max: 2.3, 20 contours

Figure 3.25. Temperature distribution in the float zone neglecting convective heat transport.

pattern shows a single recirculating zone in each half of the domain and is tangential to the free surface. It may be recalled that since surface tension effects have not been accounted for, the free surface does not exert a shear stress on the fluid. The fluid adjacent to the free surface is heated and rises to the top of the domain due to buoyancy effects, causing the isotherms to be distorted towards the top of the domain and the location of Θ_{max} to shift correspondingly upwards. The magnitude of Θ_{max} drops to 1.14, reflecting the validity of the temperature scale defined by Eq. (3.12b).

3.4.6 Interaction of Natural and Thermocapillary Convection

$Gr = 10^6$, $Pr = 0.1$, and $Ma = 500$. Figure 3.27(a) shows the streamfunction and isotherms by imposing a Marangoni number of 500. Since the surface tension decreases with temperature, the tendency of the surface tension gradient induced shear stress is to reduce the convection strength in the vicinity of the convex part of the free surface (labelled B in Fig. 3.27a) and increase the convection strength near the upper part of the domain where the free surface is concave (labelled A in Fig. 3.27a). The overall effect is to marginally shift

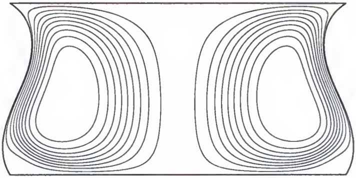

Gr = 10^6, Ma = 0, Streamfunction: max: 6.31, 20 contours

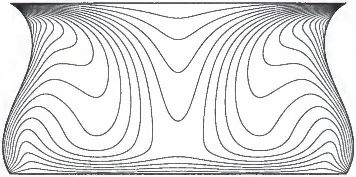

Gr = 10^6, Ma = 0, Isotherms: max: 1.14, 20 contours

Figure 3.26. Effect of natural convection on transport characteristics in the float zone.

the location of Θ_{max} in the downward direction, towards the convex portion of the free surface as compared with the Ma = 0 solution shown in 3.27(b).

Gr = 10^6, Pr = 0.1, and Ma = 1000. Figure 3.27(b) shows the effect of increasing the Marangoni number. The trends established in the previous case continue, shifting the location of Θ_{max} downwards towards the convex portion of the free surface. Since the

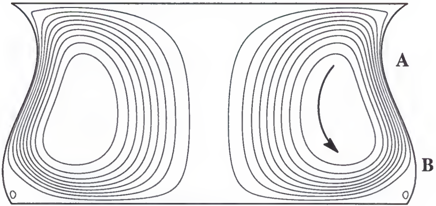

Streamfunction
max: 5.99, 20 contours

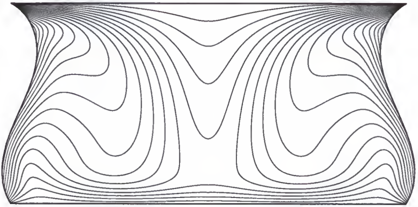

Isotherms
max: 1.14, 20 contours

Figure 3.27. Effect of Grashof number, Marangoni number and Prandtl number on transport characteristics in the float zone.

(a). $Gr = 10^6$, $Ma = 500$ and $Pr = 0.1$. The shear stress due to the surface tension gradient marginally decreases the overall convection strength since it counteracts the buoyancy induced convection.

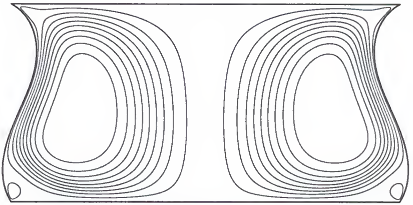

Streamfunction
max: 5.55, 20 contours

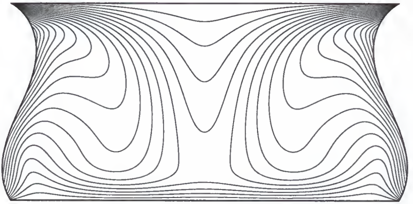

Isotherms
max: 1.18, 20 contours

Figure 3.27 — continued. Effect of Grashof number, Marangoni number and Prandtl number on transport characteristics in the float zone.

(b). Gr = 10^6, Ma = 1000 and Pr = 0.1. The trend exhibited in case (a) continues. The increased shear stresses due to the stronger surface tension gradient causes a noticeable decrease in the convection strength and an increase in maximum temperature on the free surface.

convection strength in the vicinity of Θ_{max} is further reduced, the value of Θ_{max} also increases.

Gr = 2000, Pr = 0.1, and Ma = 1000. Figure 3.27(c) shows the effect of decreasing the relative strength of buoyancy induced convection versus Marangoni convection. In this case, the convection pattern is dominated by the Marangoni effect. The convection pattern consists of counterclockwise rotating convection roll at the top right of the domain adjacent to the free surface (labelled A) and clockwise rotating convection roll at the bottom right of the domain corresponding to region labelled B. The convection rolls adjacent to the convex portion of the free surface, which occur at the lower portion of the boundary, are substantially stronger because of the stronger temperature gradients along the convex portion of the free surface. The location of Θ_{max} is close to that of the pure conduction solution as compared to the high Gr cases. The effect of Marangoni convection is to shift the location of Θ_{max} to the convex portion of the boundary.

Gr = 2000, Pr = 0.04, and Ma = 1000. Figure 3.27(d) shows the effect of decreasing the Prandtl number. The effect of lower Prandtl number is to increase the convective effects in the flow (Shyy 1994) by decreasing the magnitude of the viscous terms in the momentum equations. In the energy equation, this effect will be balanced by the increased thermal diffusivity. The convection pattern is qualitatively similar to the case shown in Fig. 3.27(c). It can be observed that the isotherms are distorted near the convex portion of the free surface, due to the strong fluid convection, whereas in the upper portion of the domain, the pattern resembles the pure conduction case.

From the above cases, some useful inferences can be made that are directly applicable to the float-zone growth of NiAl. For the length scales of current experimental interest, it is observed that the pure conduction model of heat transfer is inadequate. Strong convective heat transfer effects can be observed, which are dominated by the Marangoni effect. The Marangoni effect causes clockwise recirculating convection rolls in the bottom right and top left of the domain and counterclockwise recirculating rolls at the top right and bottom left

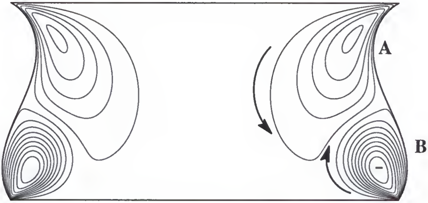

Streamfunction
min: −1.72 (–), 20 contours

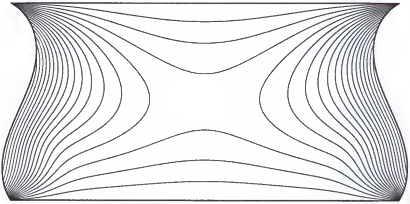

Isotherms
max: 1.47, 20 contours

Figure 3.27 — continued. Effect of Grashof number, Marangoni number and Prandtl number on transport characteristics in the float zone.

(c). Gr = 2000, Ma = 1000 and Pr = 0.1. Decreasing the Grashof number results in a clockwise rotating convection cell in the convex region of the meniscus labelled B. The location of the maximum temperature shifts downward. The convection cells in the upper region labelled A is substantially weaker than the cases dominated by buoyancy induced convection.

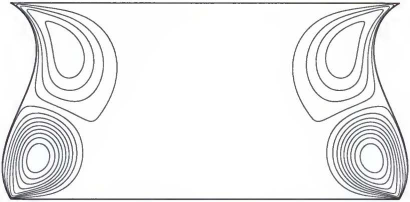

Streamfunction
min: –1.63, 20 contours

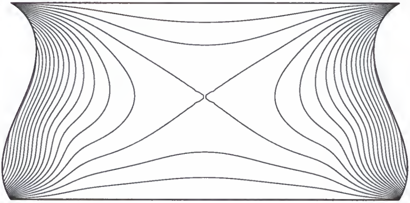

Isotherms
max: 1.57, 20 contours

Figure 3.27 — continued. Effect of Grashof number, Marangoni number and Prandtl number on transport characteristics in the float zone.

(d) Gr = 2000, Ma = 1000 and Pr = 0.04. With decreasing Prandtl number, the magnitude of the maximum temperature increases, but the convection cells do not penetrate as deeply into the melt zone and the overall convection strength is reduced.

of the domain. For the high Bond numbers that prevail under 1-g conditions on earth, the free surface has a convex shape in the lower portion of the melt due to the hydrostatic pressure of the melt column. This convex shape induces asymmetry in the shape, spatial extent, and strength of the convection rolls and the distribution of the temperature. For the pure conduction case, the convex shape causes the location of the maximum temperature to be shifted towards the convex side of the free surface. In the presence of Marangoni convection, this effect is augmented by the strong convective effect near the convex portion of the domain, due to the stronger temperature gradients along the convex portion of the free surface. This convection in turn causes the location of the maximum temperature to move further downwards. Marangoni convection completely overwhelms the buoyancy-driven convection for this particular configuration and material properties, augmenting the buoyancy effect in the upper portion of the domain and counteracting it in the lower portion of the domain. Thus, the dependence of surface tension on temperature plays a dominant role in the heat transfer characteristics in the float zone.

3.5 Effect of Convection on Meniscus Shape

It may be expected that convection in the melt will impact the meniscus shape through the normal stress terms which will be balanced by the free surface curvature. In addition, the free surface will no longer be an isotherm, which implies that the surface tension will vary from point to point depending on the spatial distribution of the temperature along the free surface. Under such conditions, Equation (2.15) must be modified as follows:

$$\Delta\varrho\ g\ y - \Delta p + 2\mu\frac{\partial v_n}{\partial n} = \gamma(T)\left[\frac{f''}{(1 + f'^2)^{3/2}} - \frac{1}{f\ (1 + f'^2)^{1/2}}\right] \tag{3.17}$$

where μ is the viscosity of the melt. This can be nondimensionalized in a manner similar to Eq. (2.15) along with the reference velocity scale defined as α/r_b, where α is the thermal diffusivity. In nondimensional form, this becomes:

$$\mathrm{Bo}\ \hat{y} - \Delta\hat{P} + \mathrm{Ca}\frac{\partial \hat{V}_n}{\partial n} = \left(1 - \left|\frac{d\gamma}{dT}\right|\frac{\Delta T}{\sigma_o}\right)\left[\frac{\hat{f}''}{(1 + \hat{f}'^2)^{3/2}} - \frac{1}{\hat{f}\ (1 + \hat{f}'^2)^{1/2}}\right] \tag{3.18}$$

where Ca is the Capillary number defined as $(2\ \mu\ \alpha)/(\gamma_o\ r_b)$, γ_o is the surface tension at the reference temperature, and the italics denote the nondimensionalized variables. The Capillary number and the Bond number determine the relative influence of the hydrostatic and the convective effects, respectively. The term premultiplying the curvature term describes the correction due to the variation of surface tension with temperature. In many instances as will be illustrated later it is found that the Capillary number, Ca, as well as the normal gradient of the normal velocity are both small compared to the hydrostatic term, from an a posteriori estimation, and hence meniscus shapes based on Eq. (2.15) generally suffice.

The deformation of the free surface due to thermocapillary convection is dominated by the Capillary number. For example, Zebib et al. (1985) found that whereas the shape is qualitatively sensitive to the Prandtl number, the magnitude of the deformation is determined, to the leading order, by the Capillary number. More insight into the effects of Marangoni convection on transport dynamics can be found in Carpenter and Homsy (1989) and Mundrane and Zebib (1994). Equation (3.18) describes the role of the normal stress, arising from the normal derivative of the normal velocity component at the free surface, in changing the shape of the meniscus. Under 1-g conditions and at the length scales considered, the hydrostatic terms dictated by the high Bond numbers are the dominant terms in Eq. (3.18) and the normal stress terms due to convection are small compared to the hydrostatic term. As an example consider the impact of convection on the shape of the liquid bridge considered earlier in this chapter. The Bond number for this case is Bo = 8.8 and the Capillary number is $Ca = 1.5 \times 10^{-5}$. The impact on the surface curvature varies with the vertical distance and is described by $1 + \dfrac{Ca\ \partial\hat{V}_n/\partial n}{Bo\ \ \hat{y}}$. This quantity may be plotted to show the variation of its magnitude along the y-axis as shown in Figure 3.28. This shows that except at the lowermost corners of the domain, the normal stress term is vanishingly small. Considering that the meniscus is pinned at both the top and the bottom of the domain, the correction to the overall shape of the meniscus is expected to be modest except at the

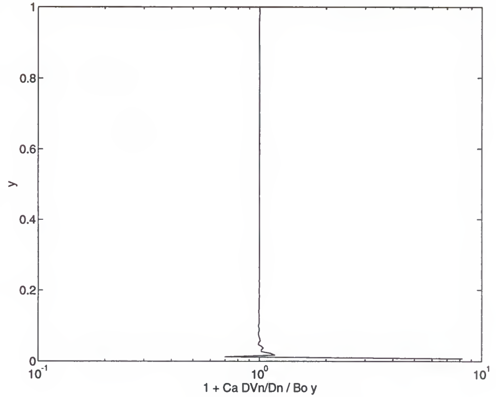

Figure 3.28 Semilog plot of Y versus $1 + \dfrac{\mathrm{Ca}\ \partial\hat{V}_n/\partial n}{\mathrm{Bo}\ \hat{y}}$.

This shows the locations where the normal stress term due to convection becomes important compared to the hydrostatic pressure.

lowermost corner where the curvature will be substantially lower. Since the effect is extremely localized at the corner locations where the flow turns to match the boundary, the overall effect on the heat transfer and convection characteristics is expected to be negligible for this case. Accordingly, corrections to the meniscus shape appear unnecessary in this particular study. We also observe that the percentage variation of the surface tension with temperature is less than 1% and hence cannot significantly affect the force balance at the interface.

Similar results have been reported by Tao et al. (1995), where a vorticity-stream function formulation was employed. The fluid chosen in that study is silicone oil, which has a very different Prandtl number, of the order of 10^2 to 10^4. Their solutions can help understand Marangoni convection in a different parameter range. In a recent effort, Hou et al. (1994) have employed a boundary integral approach to simulate surface tension driven flows, with good results obtained for a wide range of phenomena. Kanouff and Greif (1994) have analyzed oscillations in thermocapillary convection in a square cavity.

3.6 Concluding Remarks

In this chapter, different convection schemes have been investigated and applied in the context of the SIMPLE algorithm to compute fluid convection and heat transfer characteristics. Two test cases have been considered to illustrate the computational and physical aspects of buoyancy driven and thermocapillary convection. The problem of electronics cooling in a cabinet has been modeled by considering transient natural convection inside an enclosed vertical channel. Accurate simulations have been conducted to capture the transient effects which are important during startup operations. The second problem considered is Marangoni convection in a liquid bridge serving as a simplified model of the float zone crystal growth process. These simplified computations serve as the foundation for more elaborate and complex float zone simulations later in this study.

This chapter also addresses the effect of melt convection on the free surface shape in the context of small Capillary numbers encountered in the float zone growth process. It is found that in many practical configurations under 1–g conditions, the combination of high Bond number and small Capillary numbers results in negligible impact of melt dynamics on the free surface shape. These calculations form the building block for the development of a more complete algorithm for float zone simulation.

CHAPTER 4
ENTHALPY BASED PHASE CHANGE MODELING

4.1 Background

Apart from establishing the capability of solving the fluid flow and convective heat transfer problem, the computation of phase change is the other major challenge. In this chapter, a numerical method is investigated and enhanced to compute phase change phenomena on a fixed grid in the context of pressure based algorithms. In this method, also known as the enthalpy formulation, the energy equation is initially cast in terms of the total enthalpy. By splitting the total enthalpy into the sensible enthalpy and the latent heat, a unified formulation can describe energy transport in both phases. The relationship between the sensible heat and the latent heat is modeled in a simplified manner without recourse to either morphological or microscopic scales. In this manner, phase boundaries are captured naturally rather than by separate explicit tracking procedures. The spatial averaging in the enthalpy method implies that a phase fraction is defined based on the volume fraction occupied by a given phase, say, liquid. Such a two-phase approach is naturally suitable for alloys where phase change generally occurs over a temperature range, according to the local mixture composition, forming a mushy zone in which both phases can coexist. A detailed discussion can be found in Crank (1984). For pure materials, which undergo phase change at a given temperature, the mushy zone is a modeling artifact. This practice is akin to the shock capturing technique for compressible flows where a finite thickness, larger than physical reality, of the order of one or two grid spacings is needed to define the shock. However, for both shock and phase change calculations, this artificial smearing is generally quite acceptable and does not necessarily impact the global accuracy of the flow solution.

A major requirement for both problems is to devise numerical schemes that are accurate and robust in the bulk of the flow domain and can resolve the internal boundaries (shock, interface etc.) within one or two computational cells. As will be demonstrated later, this requirement can be quite satisfactorily met by the enthalpy formulation.

4.2 Heat Conduction

In the following, the enthalpy formulation and the associated numerical algorithm is developed via application to a heat conduction problem. The governing equation can be cast in the form

$$\frac{\partial(\varrho H)}{\partial t} = \nabla \cdot (k \nabla T) \tag{4.1}$$

where H is the total enthalpy. The equation can be discretized according to the conventional control volume procedure, wherein the total enthalpy H and the temperature T can be interpreted as averaged values within a control volume. Then H can be written as

$$H = C_p \, T + f \cdot L \tag{4.2}$$

where f is the phase fraction of phase 1 and can be interpreted as the fractional volume of a computational cell occupied by that phase. The phase fraction of phase 1 is zero in the region occupied by phase 2 and unity in the region occupied by phase 1. The phase fraction lies between zero and unity when the control volume is undergoing phase change. L is the latent heat. Substituting equation (4.2) into the governing equation (4.1) we get:

$$\frac{\partial(\varrho C_p T)}{\partial t} = \nabla \cdot (k \nabla T) - L \cdot \frac{\partial(\varrho f)}{\partial t} \tag{4.3}$$

where the latent heat now appears as a source term. This formulation is a single-region formulation, wherein one set of governing equations can describe both phases and hence can more readily handle complex interface shapes, branched and multiple-valued interfaces. To close the physical model, a unique relationship between the fluid fraction f and the temperature T has to be formulated. For a pure substance undergoing isothermal phase change, the total enthalpy, H, is a discontinuous function of the temperature (Fig. 4.1a)

$$H = \begin{cases} C_p T , & T < T_m \\ C_p T + L , & T > T_m \end{cases} \tag{4.4}$$

However, from a computational viewpoint discontinuities are difficult to track, and often it is necessary to smear the phase change over a small temperature range to attain numerical stability, as schematically illustrated in Fig. 4.1(b). Thus,

$$H = \begin{cases} C_p T , & T < T_s \\ C_p T_s + \left[C_p + \frac{L}{2\varepsilon} \right] (T - T_s) , & T_s \leq T \leq T_l \\ C_p T + L , & T > T_l \end{cases} \tag{4.5}$$

where $T_s = T_m - \varepsilon$, $T_l = T_m + \varepsilon$, and ε is a phase change interval. The discontinuity is thus replaced by a small interval over which phase change occurs. For a pure substance undergoing isothermal phase change, this is a purely numerical artifact and needs to be as low as possible in order to accurately model the physical system. The above relationship is substituted into Eq. (4.5) to obtain:

$$f = \frac{T - T_s}{2 \varepsilon} \tag{4.6}$$

which is used to iteratively update the phase fraction from the computed temperature field. This technique has been used successfully by many researchers, including Bennon and

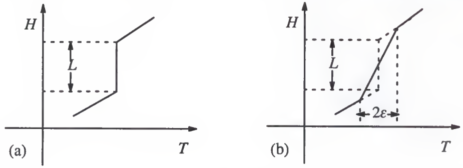

Figure 4.1 (a) Schematic of the enthalpy — temperature relationship for a pure substance; (b) Illustration of the numerical treatment of the discontinuity which is accomplished by smearing the phase change interval over a finite temperature range.

Incropera (1987), Lacroix (1989), Lacroix and Voller (1990), Prakash (1990), Prakash and Voller (1989), Shyy and Chen (1991), Voller and Cross (1981), Voller and Prakash (1987) and henceforth will be referred to as the T-based update method. An alternative formulation is to express the phase fraction as a function of the total enthalpy rather than the temperature, whereby a continuous relationship can be obtained (Atthey 1975). An implicit procedure is examined here. First, we invert the $H = H(T)$ relationship (4.5) (see Fig. 4.2) so that

$$T = \begin{cases} \dfrac{H}{C_p}\ , & H < H_s \\ T_s + \left[\dfrac{2\varepsilon}{L + 2C_p\varepsilon}\right] (H - H_s)\ , & H_s \le H \le H_l \\ \dfrac{H - L}{C_p}\ , & H > H_l \end{cases} \tag{4.7}$$

where H_s and H_l are the enthalpy values corresponding to the T_s and the T_l temperatures, respectively, $H_s = C_p T_s$ and $H_l = C_p T_l + L$, for constant C_p. Substituting the above relationships into Eq. (4.7), we obtain

$$f = \frac{H - H_s}{H_l - H_s} \tag{4.8}$$

for the iterative update of the fluid fraction. The motivation for the above formulation stems from the fact that the temperature is always a continuous function of the total enthalpy. In

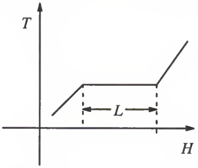

Figure 4.2. Sketch showing the inverted enthalpy — temperature relationship for a pure material.

particular, it is noted that $\varepsilon = 0$ is allowed in this formulation, thereby accurately modeling phase change of a pure substance. Another motivation is the fact that in the phase change zone, the phase fraction is a rapidly varying function of the temperature, causing it to be sensitive to small errors in temperature. In particular, this can result in an unphysically thick phase change zone (mushy region) due to round-off errors in the temperature calculation. Contrast this with the fact that if the latent heat is large relative to the sensible enthalpy, the phase fraction is a slowly varying function of the total enthalpy resulting in a more stable update procedure. This update procedure will henceforth be referred to as the H-based update method.

4.3 Numerical Implementation

4.3.1 The T–Based Method

A straightforward implementation of the T-based method, using the notation due to Patankar (1980), would be

$$a_P T_P^k = \sum a_{nb} T_{nb} + b^k - \varrho \cdot L \, \frac{\Delta x \, \Delta y}{\Delta t} \left[f_P^{k-1} - f_P^{n-1} \right] \tag{4.9}$$

followed by the iterative update

$$f_P^k = \begin{cases} 0 & , \quad T_P^k < T_s \\ \dfrac{T_P^k - T_s}{2\,\varepsilon} & , \quad T_s \le T_P^k \le T_l \\ 1 & , \quad T_P^k > T_l \end{cases} \tag{4.10}$$

where the superscript k stands for the current iteration value at a given time level n and superscript n – 1 stands for the previous time level. For Stefan numbers less than unity (large values of latent heat relative to the sensible heat $C_p \Delta T$), this form of the iterative update is prone to numerical instability in the form of oscillations, although for moderate Stefan numbers, underrelaxation of the source term or the phase fraction update facilitates the solution process. Similar findings have been reported by Prakash et al. (1987), Prakash and Voller (1989), Voller and Prakash (1987). The chief cause of this oscillatory, nonconvergent behavior is the extreme sensitivity of the phase fraction to small changes in temperature, leading to a large negative feedback effect through the source term. This tendency gets worse as the Stefan number is reduced and the time step is refined. A simple hypothetical example will serve to illustrate the deficiencies of the above procedure and also will provide a criterion for devising a stable update procedure. Consider some typical nondimensional parameters: $L = 20$, $T_m = 0.5$, $C_p = 1$. Choose $\varepsilon = 0.1$, then $T_s = 0.4$ and $T_l = 0.6$. Suppose that in the course of the calculation we obtain $T^k = 0.39$, $f^k = 0$ and $T^{k+1} = 0.42$; now calculate the total enthalpy, $H = T^{K+1} + f^k \Delta H = 0.42$; carrying out the update procedure, we get $f^{k+1} = 0.1$. The total enthalpy H jumps to 2.42, an increase of about 500% due to the update procedure alone. This large jump in total enthalpy due to the update procedure is nonphysical; the temperature and fluid fraction fields are no longer consistent with the discrete form of the conservation law. Thus this update procedure will not be able to yield mutually consistent T and f fields and hence is not guaranteed to converge (Shyy and Rao 1994a). A more stable update procedure can now be devised by substituting Eq. (4.10) into the discrete form of the conservation law and moving the resulting coefficients of T_p into the a_p term to give

$$a_P T_P^k = \sum a_{nb} T_{nb}^k + b^k - \varrho \cdot L \frac{\Delta x \; \Delta y}{\Delta t} \left[f_P^{n-1} \right] \quad , \qquad T_P^{k-1} < T_s$$

$$\left[a_P + \varrho \cdot L \frac{\Delta x \; \Delta y}{\Delta t} \frac{1}{2\varepsilon} \right] T_P^k = \sum a_{nb} T_{nb}^k + \varrho \cdot L \frac{\Delta x \; \Delta y}{\Delta t} \left[\frac{T_l}{2\varepsilon} + f_P^{n-1} \right] , \qquad T_s \le T_P^{k-1} \le T_l \tag{4.11}$$

$$a_P T_P^k = \sum a_{nb} T_{nb}^k + b^k - \varrho \cdot L \frac{\Delta x \; \Delta y}{\Delta t} \left[f_P^{n-1} - 1 \right] \quad , \qquad T_P^{k-1} > T_l$$

where the superscript k indicates the current iterative value. It can be observed that with this form of the update procedure, the temperature and the fluid fraction field are computed simultaneously and are therefore mutually consistent at every step of the iterative process. This procedure converges quickly while still retaining accuracy, as will be demonstrated later.

4.3.2 The H–Based Method

The implementation of the H-based method is relatively straightforward. Equation (4.9) is applied at every discrete cell, followed by the update procedure, which can be written as follows:

(i) Compute the total enthalpy

$$H_P^k = C_p T_P^k + f_P^{k-1} \cdot L \tag{4.12}$$

(ii) Carry out the update procedure:

$$f_P^k = \begin{cases} 0 & , \quad H_P^k < H_s \\ \dfrac{H_P^k - H_s}{H_l - H_s} & , \quad H_s \leq H_P^k \leq H_l \\ 1 & , \quad H_P^k > H_l \end{cases} \tag{4.13}$$

4.4 Results and Discussion

4.4.1 Accuracy Assessment

A one-dimensional conduction driven phase change problem with an exact solution was chosen as the test bed for the assessment of accuracy (Chandra 1990). A schematic is shown in Fig. 4.3. Consider an idealized phase change material, with constant thermophysical properties, including density, and with phase change occurring at a constant, specified temperature. This implies the absence of convection, the phase change being driven entirely by the conduction process and release of latent heat at the phase change interface. This class of problems is also known as the Stefan problem. The material is initially at the phase-change temperature, $T_m = 0$. At time, $t = 0$, the temperature at $x = 0$ is instantaneously raised to $T_h = 1$. The interface is defined by the $T = T_m = 0$ isotherm. For the pure conduction problem in each phase we have

$$\frac{\partial T_i}{\partial t} = \alpha_i \nabla^2 T_i \qquad i = \text{liquid, solid} \tag{4.14a}$$

along with the jump condition:

$$k_s \frac{\partial T_s}{\partial n} - k_l \frac{\partial T_l}{\partial n} = \varrho L v_n \tag{4.14b}$$

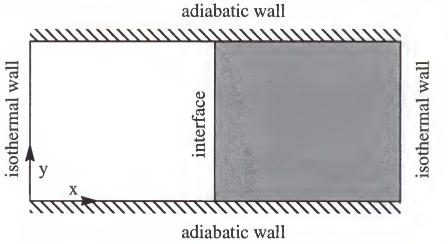

Figure 4.3. Schematic of the phase change problem showing the domain and boundary conditions. For the conduction driven problem, the interface is planar. For the problem with gravity driven convection included, the gravity vector is in the negative y direction.

where v_n is the interface velocity. For this problem, a closed-form solution exists for the time-dependent location of the phase change front given by $x = 2\lambda\sqrt{\alpha t}$, where λ is the root of

$$\lambda \exp\left(\lambda^2\right) \operatorname{erf}(\lambda) = \frac{\mathrm{St}}{\sqrt{\pi}} \tag{4.15}$$

and St is the Stefan number; defined as $\mathrm{St} = C_p\left(T_h - T_m\right)/L$. Note that the heat flux to the interface takes place only through the liquid and the solid remains at a uniform temperature.

Calculations were carried out on uniform grids consisting of 21 and 41 nodes with a time step $\Delta t = 0.01$ and on a grid with 81 points with time steps $\Delta t = 0.1$, 0.01, and 0.001 for both the H-based and the T-based methods in order to compare the two methods on the basis of accuracy. Comparisons were made with the exact solution to assess the accuracy of the two methods on the basis of the interface location. The interface location was obtained by interpolating for the $f = 0.5$ contour. For the T-based method, $\varepsilon = 10^{-5}$ was adopted. Second-order central differences were used for all spatial derivative terms and first-order Euler backward differencing was employed for marching in time. Figures 4.4(a) and 4.4(b) show that the H-based and T-based methods yield identical solutions even for coarse grids. An error distribution was formed by computing the relative error at every time instant. Figure 4.4(c) shows that the error distribution oscillates about a zero mean. This can be correlated with the fact that a significant part of the latent heat content in a computational cell is released when it starts to undergo phase change. Thus the interface first slows down when a computational cell just starts to change state and then subsequently speeds up. The computed solution coincides with the exact solution when the interface is at the boundary between two control volumes. The amplitude of the error distribution drops with increasing spatial resolution, and its frequency doubles when the grid spacing is halved. A measure of the cumulative error is obtained from the norm of the error distribution, which is the rms value of the error distribution. A log-log plot of the cumulative error versus Δx (Fig. 4.4(d)) shows that the cumulative error varies as $(\Delta x)^{1.5}$. A calculation conducted with a time step of 0.001 yielded a solution that could not be distinguished from the solution for the time step of 0.01. This indicates that the solution is time-accurate.

4.4.2 Performance Assessment

The problem described above was generalized in order to make an extensive comparison of the two update procedures formulated earlier. In general, the solid and liquid phases differ in their thermal diffusivities. Thus the above problem was reformulated such that a steady state solution would exist with the interface positioned within the computational domain so that the effects of heat conduction through the solid would also play an equally important role. So the phase-change temperature was set to $T_m = 0.5$ with all other parameters being the same as the previous study.

Figures 4.5, 4.6, and 4.7 show the solutions and the relative performance obtained for various combinations of ε, Δt, and Δx. Figures 4.5 and 4.6 show the solutions and performance comparisons on a coarse grid of $\Delta x = 0.04$ for time steps Δt of 0.1 and 0.01 and with ε of 10^{-2}, 10^{-3}, 10^{-4}, and 10^{-6}. As ε decreases, the step-like character of the interface movement becomes obvious. Corresponding to these step-like movements, there are sharp spikes in the iteration count required for convergence at the given time step. It is evident that the T-Based method requires far fewer iterations when ε and Δt are relatively large. It is also noted from Fig. 4.5(d) that the T-Based method performs better than the H-Based method as the interface slows down and approaches the steady state. For a combination of low ε and smaller Δt, the T-Based method does not converge and solutions can be obtained only with the H-Based method as is evident in Fig. 4.5(e) and (f) and also in Fig. 4.6(e) and (f), where $\varepsilon = 10^{-6}$ and a time step $\Delta t = 0.01$ have been employed. Figure 4.7 shows the effect of grid refinement. The spatial resolution was doubled to $\Delta x = 0.02$. In Fig. 4.7(a), for $\varepsilon = 10^{-2}$, the step-like behavior almost vanishes but reappears when ε is decreased to 10^{-3} in (c). The corresponding performance curves in (b) and (d) show the same trends, that is, the T-Based method performs better under more benign conditions, but when ε is reduced the relative advantage reduces and the H-Based method becomes more efficient. The H-Based method is not very sensitive to the value of ε and can work for $\varepsilon = 0$. Also, the T-Based method is more efficient when the interface motion approaches the steady state. In general, it appears that the T-Based method is relatively efficient compared to the H-Based method when the magnitude of the nonlinear term $\frac{L\ \Delta x\ \Delta y}{\Delta t}\ \frac{T^n - T^{n-1}}{2\ \varepsilon}$ is sufficiently low. In particular, the performance degrades rapidly with decreasing ε until a point is reached where a solution is no longer feasible with the T-Based method.

4.4.3 Summary

The enthalpy formulation has been applied to a one-dimensional heat conduction driven phase-change problem to examine alternative procedures for the phase fraction update. The range of applicability and relative performance of the T-based and H-based updates have been examined in the context of solidification problems. It is shown that the T-based update can yield better performance provided the time step is not too small and the grid has sufficient resolution. Recently, Ding and Anghaie (1994) have found that the H-based update yields

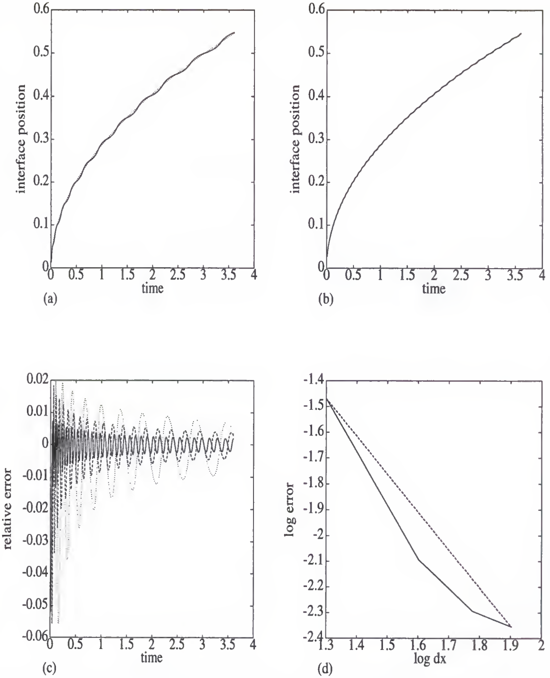

Figure 4.4. Solution features for the pure conduction problem with St = 0.042: (a) Coarse grid solution (21 grid points); (b) Fine grid solution (41 grid points). In each case the solid line designates the solution obtained using the H-based method, the dashed line using the T-based method and the dotted line is the exact solution. The H-based and the T-based method yield identical results. (c) Error at every time instant for various grid sizes. The solid line is the error with $\Delta x = 1/80$, the dashed line is the error with $\Delta x = 1/40$, and the dotted line is the error with $\Delta x = 1/20$. The error oscillates about a zero mean, its amplitude decreases and the frequency doubles when the grid spacing is halved. (d) Cumulative error versus grid spacing for $\Delta t = 0.01$. The solid line is the numerical result, and the dotted line has an approximate slope of 1.5.

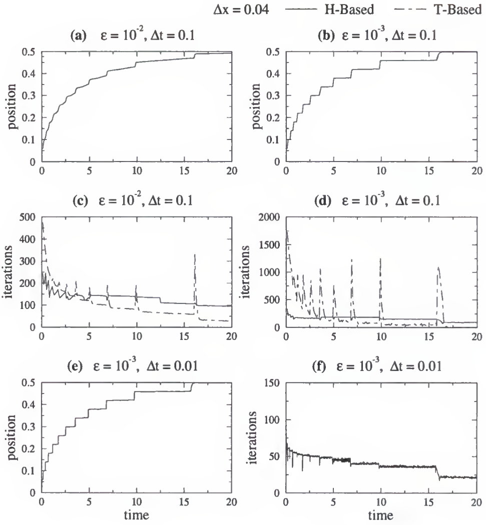

Figure 4.5. Comparison of the H-Based and the T-Based update methods for the conduction problem using a grid with 26 uniformly distributed points, i.e., $\Delta x = 0.04$. In all cases the solid line represents the H-Based method and the dash-dotted line, the T-Based method. (a) and (b) show the solutions obtained with ε of 10^{-2} and 10^{-3}, respectively. (c) and (d) show the relative performance of the two schemes with ε of 10^{-2} and 10^{-3}, respectively. In (e) and (f), where the time step has been reduced from $\Delta t = 0.1$ to $\Delta t = 0.01$, the T-Based method could not reach a residual of 10^{-4} and has been excluded from consideration.

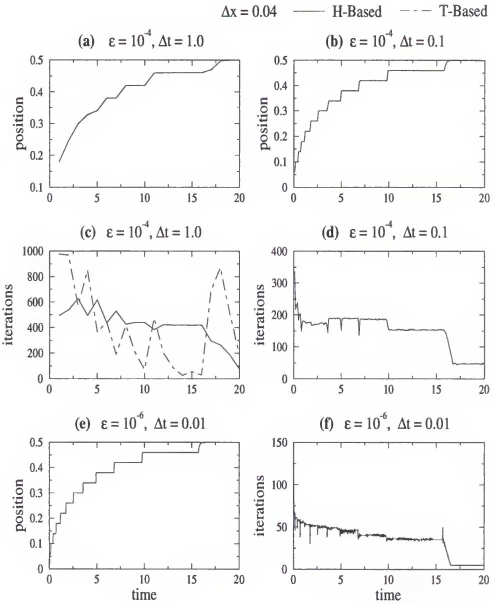

Figure 4.6. In (a) and (b) the value of ε has been further reduced to 10^{-4}. It is seen that the T-Based method does not yield solutions when the time step is reduced from $\Delta t = 1.0$ to $\Delta t = 0.1$. When the T-Based method works, it gives better performance than the H-Based method, as shown in (c) and (d). However, from (a) and (b) it is obvious that the solutions are not time step independent. (e) shows the results of the H-Based method for $\varepsilon = 10^{-6}$ and $\Delta t = 0.01$. The T-Based method does not converge to a residual level of 10^{-4} for this combination of lower ε and lower Δt.

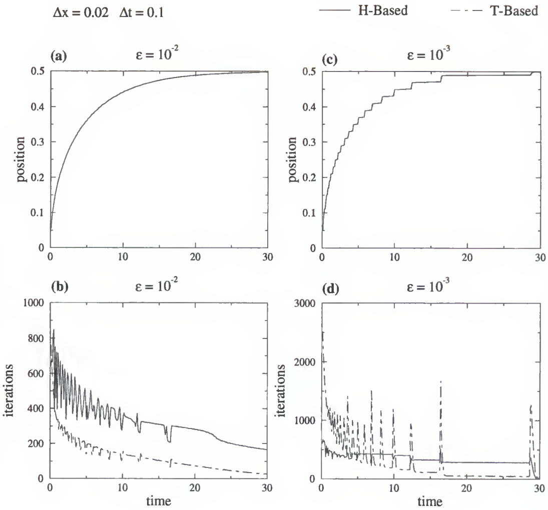

Figure 4.7. This shows the effect of grid refinement. The calculations were carried out on a grid with 51 uniformly distributed points. (a) and (c) show that the step-like behavior of the solutions decreases with increasing spatial resolution. The spikes in the performance curves in (b) and (d) correspond to the step-like movement of the interface in (a) and (c), respectively. The T-Based method performs better in both cases, but its comparative advantage reduces as ε is reduced from 10^{-2} to 10^{-3}. Also, it may be observed that the H-Based method performs better when the temporal gradients are high, i.e., when the interface moves faster due to higher thermal fluxes.

better performance for the evaporation problem where the boiling point varies with the pressure according to the Clausius-Clayperon equation (Shyy 1994). Thus, the choice of the update procedure depends on the computational parameters, such as time step and grid resolution, and on physical parameters such as the phase change interval and whether the interface temperature varies with the pressure, as in the evaporation/condensation problem.

4.5 Convective Effects

So far, only conduction-dominated effects have been taken into account, but, as will be demonstrated in the following, convection can substantially modify the flow and heat transfer characteristics. Consequently, the interface shape and translation velocity can be substantially altered by fluid convection. Consideration of fluid convection implies that the fluid fraction field be coupled with the flow solver along with the energy equation. In the energy equation, apart from the fluid convection terms, additional source terms are incorporated. In the momentum equations, the velocities in the solid need to be set to the casting rate of the solid phase. One way to accomplish this is by considering the mushy zone to be a porous medium and incorporating D'arcy law terms in the momentum equations. The D'arcy law terms vary the porosity as a function of the fluid fraction from unity in the liquid to zero in the solid.

4.5.1 Governing Equations

The governing equations in Cartesian coordinates and in dimensional form for two-dimensional, incompressible flow can be written as:

continuity:

$$\frac{\partial(\varrho u)}{\partial x} + \frac{\partial(\varrho v)}{\partial y} = 0 \tag{4.16a}$$

x–momentum:

$$\frac{\partial(\varrho u)}{\partial t} + \frac{\partial(\varrho uu)}{\partial x} + \frac{\partial(\varrho uv)}{\partial y} = -\frac{\partial p}{\partial x} + \left[\frac{\partial}{\partial x}\left(\mu\,\frac{\partial u}{\partial x}\right) + \frac{\partial}{\partial y}\left(\mu\,\frac{\partial u}{\partial y}\right)\right] - A\,(u - u_{cast}) \tag{4.16b}$$

y–momentum:

$$\frac{\partial(\varrho v)}{\partial t} + \frac{\partial(\varrho u v)}{\partial x} + \frac{\partial(\varrho v v)}{\partial y} = - \frac{\partial p}{\partial y} + \left[\frac{\partial}{\partial x}\left(\mu \frac{\partial v}{\partial x}\right) + \frac{\partial}{\partial y}\left(\mu \frac{\partial v}{\partial y}\right) \right] - \left(\varrho - \varrho_{ref}\right) g - A\left(v - v_{cast}\right) \quad (4.16c)$$

energy:

$$\frac{\partial(\varrho C_p T)}{\partial t} + \frac{\partial(\varrho C_p u T)}{\partial x} + \frac{\partial(\varrho C_p v T)}{\partial y} = \left[\frac{\partial}{\partial x}\left(k \frac{\partial T}{\partial x}\right) + \frac{\partial}{\partial y}\left(k \frac{\partial T}{\partial y}\right) \right] - L \left[\frac{\partial(\varrho f)}{\partial t} + \frac{\partial(\varrho u f)}{\partial x} + \frac{\partial(\varrho v f)}{\partial y} \right] \quad (4.16d)$$

In the above, ϱ is the density, u is the velocity component in the x-direction, v, the velocity component in the y-direction, p is the pressure, μ is the viscosity, k is the conductivity, g is acceleration due to gravity, L is the latent heat of fusion, C_p is the specific heat, f is the liquid fraction, u_{cast} and v_{cast} denote the prescribed velocity at which the solid phase is moving, say, for example, in a crystal growth or a casting process. Here, the gravity vector $\vec{g} = - g \hat{j}$ is assumed to be in the negative y direction. For inclined configurations, the appropriate components should appear in both the momentum equations.

4.5.2 Source Terms in the Momentum Equations

When computing the solidification process on a fixed grid, special treatment is needed to enforce the solid velocity to be either zero or equal to the pulling rate of the solid phase in a typical crystal growth or casting operation. The approach taken here is the inclusion of D'arcy-type source terms in the momentum equations. Here the phase change material is considered to be a porous medium, with the porosity changing from zero to unity as the material melts. For pure materials, the porosity changes abruptly as the phase change occurs, but to ensure numerical stability a continuous variation should be imposed. Following Shyy and Chen (1991a), the term A in Eqs. 4.16(b,c) is a function of the liquid fraction as follows:

$$A = C \left(\frac{1 - f^2}{f^3 + q} \right) \tag{4.17}$$

where the constants C and q are adjusted so that A is at least seven orders of magnitude higher than all the other terms in the momentum equations in the solid region. For a pure material, which melts isothermally, the concept of a porous mushy zone is a numerical artifact, but for alloys, which melt over a temperature range, the porous mushy zone is a physical reality, and convection within the mushy zone definitely influences the structure of the mushy zone (Voller and Prakash 1987). However, it is not straightforward to obtain a relationship between the morphology of the mushy zone and the D'arcy source term, (4.17), and it is certainly a matter for further investigation.

4.5.3 Sources of Convection

Depending on the geometry and the configuration, there can be several driving forces for convection in phase-change systems. Consider typical solidification systems. Unless the solidification process takes place under microgravity conditions, say, on orbiting space platforms, gravity is always present, and thermal inhomogeneities, which also are always present, give rise to density differences. Density gradients also can be caused by compositional inhomogeneities. Depending on the mutual orientation of the gravity vector and the density gradient, buoyancy driven convection can be set up which can significantly alter the temperature and composition distribution within the system and also affect the solid–liquid interface shape and dynamics. If there is a free surface separating the liquid phase and a surrounding ambient gas, a surface tension gradient usually will exist, caused by thermal and composition inhomogeneities, which will exert a shear stress on the fluid phases, leading to Marangoni convection. The different modes of convection can interact to give very complex flow patterns (Shyy and Chen 1993).

Convection also can be caused by density changes during phase change. Usually the different phases have quite different densities. This can be a source of vigorous convection as the fluid moves to conserve mass (Shyy 1994). Many other modes of convection can exist and interact, such as forced convection (due to crystal rotation, etc.), convection due to time-varying electromagnetic fields, etc. The examples shown later in this chapter will be confined to thermally induced buoyancy driven convection.

4.5.4 Computational Procedure

The solution methodology employs a finite volume formulation in the context of the SIMPLE algorithm discussed in chapter 2. Second-order central difference schemes are used to discretize the diffusion and the convection terms. The unsteady terms are discretized using the implicit first order Euler differencing. The phase-change source terms are discretized in a manner consistent with the rest of the terms in energy equation. Specifically, the $\vec{V} \cdot \nabla f$ term is discretized consistently with the $\vec{V} \cdot \nabla T$ term. Further details of the general solution procedure can be found in Shyy (1994).

As an illustration of the procedure, the melting of gallium in a square cavity can be considered. For this case, Gau and Viskanta (1986) have reported experimental information of interface shapes and position at specified time instants. The shape of the phase change interface is determined by the combined effects of conduction and convection driven by buoyancy forces. It will be shown that convective effects can have a substantial impact on the interface shape.

In order to make a comparison of the predicted interface shape, at various time instants, with the experimental results of Gau and Viskanta (1986), the calculations were carried out with the following parameters: $Ra = 2.2 \times 10^5$, $Pr = 0.0208$, $St = 0.042$. A value of $\varepsilon = 0.001$ was used in conjunction with the T–based method to ensure numerical stability. The time stepping scheme chosen was the 1st order backward Euler and the convection scheme chosen was the 1st order upwind method. All other terms were discretized by 2nd order central differences. The interface location was determined by interpolation for the $f = 0.5$ contour. Solutions were computed on a 21×21 uniform grid and a 41×41 uniform grid and a time step of 0.01 (1.43 seconds). Numerical results have been shown for t = 2 mins, 5 mins, 6.667 mins and 8 mins in Fig. 4.8 alongside the experimental determinations of Gau

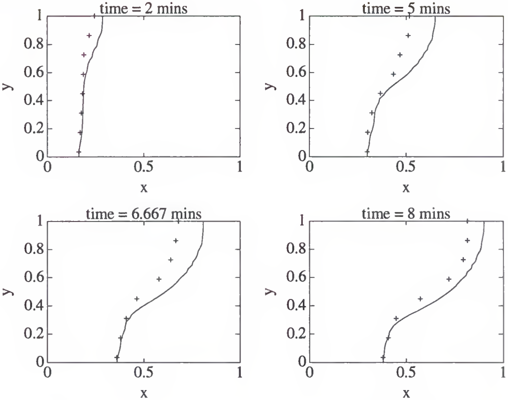

Figure 4.8. Qualitative comparison of predicted interface shapes obtained on a 41 × 41 uniform grid (solid line) with experimental data (+) of Gau and Viskanta (1986) for the melting of gallium in a square cavity.

and Viskanta, after translating the predicted interface to account for the undercooling present in the experiment (Lacroix 1989). Reasonable agreement has been obtained in terms of the interface shapes at the various time instants. The effect of convection is to transport the hot fluid to the top of the cavity and the interface moves faster near the top of the cavity. The shape of the interface is distorted by the convection patterns established as the calculation progresses in time. Thus, it is evident that natural convection can substantially affect the speed and the shape of the interface from the planar one yielded by the pure conduction calculations.

4.6 Effect of Gravity Jitter

Many devices in spacecraft contain enclosures filled with fluids. In the following, a problem is formulated which is motivated by the need of understanding materials solidification in a reduced but fluctuating gravitational field, the so–called g–jitter condition.

The configuration schematically illustrated in Fig. 4.9 was subjected to a sinusoidal variation in the magnitude of the gravity vector:

$$g(t) = \frac{g_{max}}{2}\left[1 + \sin(\omega t)\right] \tag{4.18}$$

The initial condition for this calculation was the conduction driven solution with a planar interface at the x = 0.5 location. Calculations were then conducted with an angular frequency, $\omega = 1$ and Rayleigh number, $Ra = 10^5$, based on the maximum value of the gravity vector, g_{max}. A uniform grid of 41 × 41 nodes was used and the time step used was 5% of the time period of the forcing function.

The following quantities are used to describe and assess the solution. q_h ; the total heat flux through the hot wall (x = 0), q_c ; the total heat flux through the cold wall (x = 1). A measure of the instantaneous interface location and shape was obtained by sampling the *f* = 0.5 contour at a total of 5 points, at every discrete time step. The coordinates of the sampled points may be described as: (a(t),0), (b(t),0.25), (c(t),0.5), (d(t),0.75), and (e(t),1) where a, b, c, d and e are found by interpolating for the *f* = 0.5 contour, along y = 0, y = 0.25, y = 0.5, y = 0.75 and y = 1 respectively, at every time step. A schematic describing this process

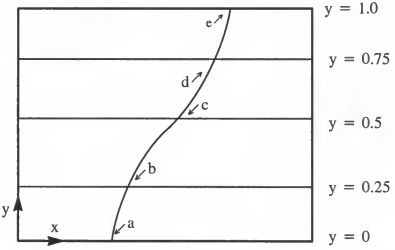

Figure 4.9 Schematic showing the sampled locations for the interface position at each time instant for the g–jitter problem.

is shown in Fig. 4.9.

Figure 4.10(a) shows the time history of the heat fluxes q_h and q_c along with their phase relationships to the forcing frequency. The heat flux through the hot wall, q_h, is mostly determined by convective effects, whereas the heat flux through the cold wall, q_c, is affected by conduction only. The quick response of convection to time variations in the body force ensures that (a) the flux q_h reaches a periodic state quickly (about 2 time periods), and (b) the phase difference between q_h and the forcing function is negligible for the chosen forcing frequency, $\omega = 1$. The heat flux q_c is determined by conduction effects and its time variation is determined by the change in boundary conditions caused by the migration of the $T = 0.5$ isotherm that constitutes the interface. Hence, q_c lags the forcing frequency by 90^o. The power spectrum of q_h, and q_c (10(b)) shows the existence of superharmonics, but the energy content of the superharmonics are at least two orders of magnitude less than that of the fundamental. Thus the fundamental frequency is the dominant one. Figure 4.11(a) shows the time history of the interface motion at the sampled points. It is observed that the portion of the interface at the top of the cavity ($y = 1$) moves towards the cold wall ($x = 1$) as g increases in magnitude and convection strength increases, whereas, the portion of the interface near the bottom of the cavity ($y = 0$) moves towards the cold wall ($x = 0$). The spectral plots (11(b)) show that the fundamental frequency is the dominant one although higher harmonics exist.

4.7 Float Zone Growth of NiAl

In the following, the enthalpy method is applied to the float zone growth of NiAl single crystals. β–NiAl is an intermetallic that is currently being investigated as a promising high temperature structural material for application in the next generation of aircraft engines and structural components. NiAl is especially attractive because of its low density, high thermal conductivity, high melting temperature, superior isothermal and cyclic oxidation resistance (Sen and Stefanescu 1991). However, it has two major drawbacks; low toughness at room temperatures and low strength at high temperatures (Darolia 1991). These deficiencies need

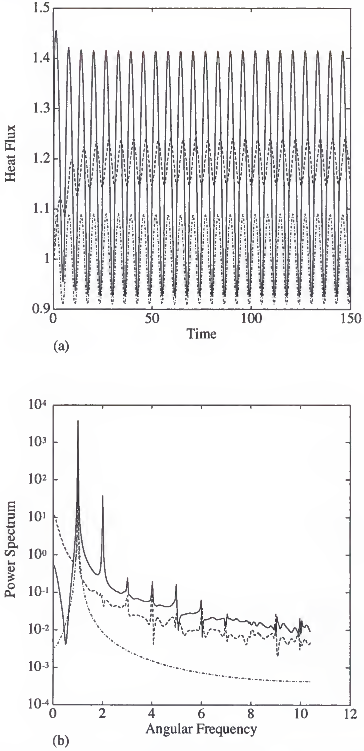

Figure 4.10. (a) Time history of the integrated heat fluxes for the g–jitter problem. The solid line indicates the heat flux through the heated wall and the dashed line indicates the heat flux through the cold wall. The dotted line indicates the forcing function. (b) Spectral plot of the heat flux through the walls of the cavity. The solid line indicates the heat flux through the heated wall and the dashed line indicates the heat flux through the cold wall. The dotted line indicates the forcing function.

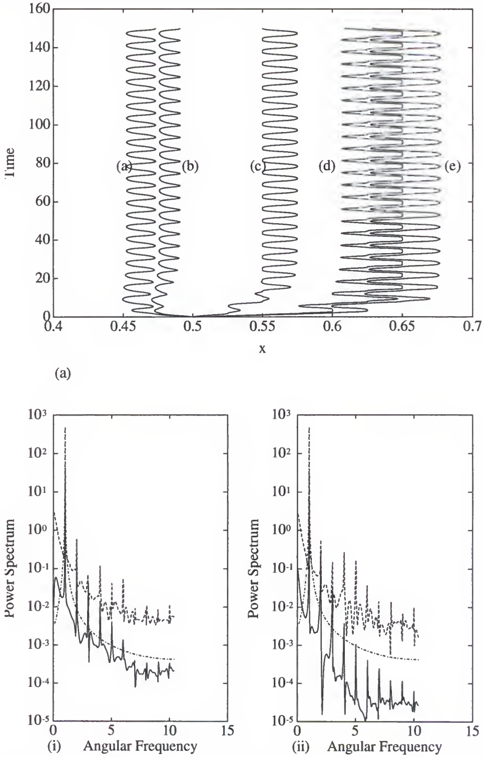

Figure 4.11. (a) Time history of the sampled interface motion at every time step. The letters a,b,c,d,e indicate the sampling locations as shown in 9 . (b) Spectral plots of the sampled interface motion. (i) The solid line refers to location a and the dashed line to location e. (ii) The solid line refers to location b and the dashed line to location d. In both cases, the dotted line refers to the forcing frequency.

to be resolved before NiAl can be used in structural applications. The current study is part of an ongoing effort to grow high purity single crystals of NiAl with controlled compositions and under controlled conditions. This would be the starting point in fundamental and detailed studies directed towards understanding the behavior of this material. Figure 4.12 shows the schematic of a practical float zone growth system for producing single crystals of NiAl. Here the enthalpy formulation is applied to a practical growth system as shown in the schematic in Fig. 4.12. In this study the scope is restricted to the convective heat transfer within the melt and its impact on the solid/liquid interface shape. Therefore, the meniscus shape and the heat input will be considered given quantities during the course of the computations.

4.7.1 Calculation Procedure

Issues regarding the formation and stability of the meniscus shapes have been discussed in chapter 2. Equation (2.15) with associated boundary conditions is used to generate the meniscus shape. In the current set of calculations, only the heat transfer within the melt and its effect on the melt/crystal and melt/feed interfaces will be of interest. In order to efficiently model the float zone with adequate resolution, it is necessary to consider only half the domain and apply symmetry conditions at the centerline. The governing equations in nondimensional form, are

(i) continuity:

$$\frac{\partial(R\tilde{u})}{\partial R} + \frac{\partial(R\tilde{v})}{\partial Y} = 0 \tag{4.19a}$$

(ii) radial momentum:

$$\frac{\partial(R\tilde{u}^2)}{\partial R} + \frac{\partial(R\tilde{u}\tilde{v})}{\partial Y} = -R\frac{\partial P}{\partial R} + \Pr\left[\frac{\partial}{\partial R}\left(R\frac{\partial \tilde{u}}{\partial R}\right) + \frac{\partial}{\partial Y}\left(R\frac{\partial \tilde{u}}{\partial Y}\right)\right] - \Pr\frac{2\tilde{u}}{R} - A\,R\,(\tilde{u} - \tilde{u}_{cast}) \tag{4.19b}$$

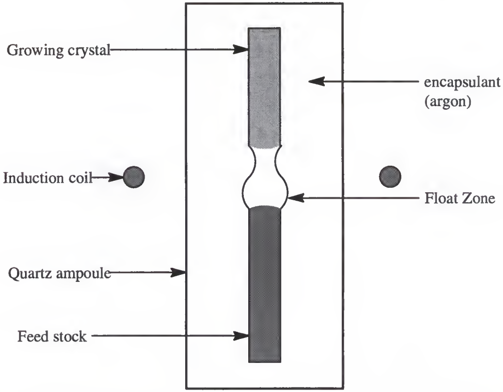

Figure 4.12. Illustration of the float zone process. The float zone is heated by the eddy currents induced by the induction coil and is held up by the surface tension between the melt and the encapsulant. The quality of the crystal is controlled by the thermofluid transport and the shape/velocity of the crystal/melt interface.

(iii) axial momentum:

$$\frac{\partial(R\tilde{u}\tilde{v})}{\partial R} + \frac{\partial(R\tilde{v}^2)}{\partial Y} = -R\frac{\partial P}{\partial Y} + \mathrm{Pr}\left[\frac{\partial}{\partial R}\left(R\frac{\partial \tilde{v}}{\partial R}\right) + \frac{\partial}{\partial Y}\left(R\frac{\partial \tilde{v}}{\partial Y}\right)\right] + R\ \mathrm{Ra}\ \mathrm{Pr}\ \Theta - AR\,(\tilde{v} - \tilde{v}_{cast}) \qquad (4.19c)$$

(iv) energy:

$$\frac{\partial(R\tilde{u}\Theta)}{\partial R} + \frac{\partial(R\tilde{v}\Theta)}{\partial Y} = \left[\frac{\partial}{\partial R}\left(R\frac{\partial \Theta}{\partial R}\right) + \frac{\partial}{\partial Y}\left(R\frac{\partial \Theta}{\partial Y}\right)\right] - L\left[\frac{\partial(R\tilde{u}f)}{\partial R} + \frac{\partial(R\tilde{v}f)}{\partial Y}\right] \qquad (4.19d)$$

and the boundary conditions are:

(i) Top and bottom boundaries:

$$\frac{\partial^2\Theta}{\partial Y^2} = 0,\ \tilde{u} = \tilde{v} = 0 \ \text{ at } Y = 0,\ 1.4 \tag{4.20a}$$

(ii) Symmetry:

$$\tilde{u} \ = \ \frac{\partial \tilde{v}}{\partial R} \ = \ \frac{\partial \Theta}{\partial R} = 0 \ \text{ at } R = 0 \tag{4.20b}$$

(iii) Free surface (melt zone): at $R = F(Y)$, $0.2 \leq Y \leq 1.2$

(a) Heat flux: $$\vec{q} = \nabla\Theta \cdot \hat{n} \tag{4.20c}$$

(b) Marangoni effect: $$\nabla(\vec{V} \cdot \hat{t}) \cdot \hat{n} = \mathrm{Ma}\ \nabla\Theta \cdot \hat{t} \tag{4.20d}$$

(shear stress equals the surface tension gradient)

(c) Kinematic condition: $$\vec{V} \cdot \vec{n} = 0 \tag{4.20e}$$

(fluid flow is tangential to the free surface)

(iv) Trijunction points: at $R = 1$, $Y = 0.2$ and $Y = 1.2$

$$\Theta = \Theta_{\text{liquidus}} = 0.2 \tag{4.20f}$$

and at $R = 1$, $Y = 0$ and $Y = 1.4$ $$\Theta = 0 \tag{4.20g}$$

where the variables have been nondimensionalized using the same reference scales as for equations (3.15a – d). The treatment of the additional source terms arising due to phase change has been described in section 4.5. The geometry and boundary conditions have been illustrated in Fig. 4.13.

The governing equations have been solved using the pressure-correction formulation in nonorthogonal body-fitted coordinates. The convection and the diffusion terms in both the momentum and the energy equations have been discretized using second order central differences. The grid points were clustered towards the free surface and for the computations involving Marangoni convection, the grid points also were clustered towards the lower boundary at $Y = 0$. Only steady state calculations have been conducted. Calculations have been carried out on two different grids – a coarse grid of 81×51 points and a fine grid of 161×101 points – to assess grid independence and solution accuracy. The fine grid system

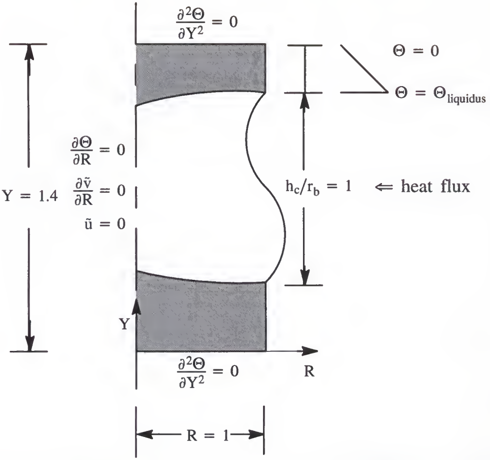
$\frac{\partial^2\Theta}{\partial Y^2} = 0$
$\Theta = 0$
$\Theta = \Theta_{liquidus}$
$\frac{\partial\Theta}{\partial R} = 0$
$Y = 1.4$
$\frac{\partial\tilde{v}}{\partial R} = 0$
$\tilde{u} = 0$
$h_c/r_b = 1$
⇐ heat flux
Y
$\frac{\partial^2\Theta}{\partial Y^2} = 0$
R
R = 1

Figure 4.13. Idealized geometry and boundary conditions.

is shown in Fig. 4.14(a). The grid has been clustered towards the free surface to obtain better resolution of the flow and heat transfer characteristics. The results shown in the following are based on the fine grid calculations.

4.7.2 Results and Discussion

It will be shown later in this section that for the given non-dimensional parameter ranges, surface tension gradients generated at the free surface will play a dominant role in melt convection and heat transfer. Based on the thermophysical properties of NiAl and the estimated environmental parameters in the experimental growth configuration of Fig. 4.12, we can arrive at the following non–dimensional parameters.

(i) Grashof number, Gr = 2000

(ii) Marangoni number, $100 < Ma < 200$ (dominant source of convection)

(iii)Stefan number, $St = 0.1$, and

(iv)Prandtl number, $Pr = 0.1$

The definitions of the parameters listed above are based on those discussed in section 2.3. The heat flux is assumed to be input normal to the free surface and is estimated based on methods outlined in chapter 2.

4.7.3 Heat Conduction

A calculation was carried out with the heat transfer taking place through conduction effects only. The purpose was to carry out an a posteriori verification of the temperature scales used to define the Grashof and the Marangoni numbers in subsequent calculations. It is noted that due to the curved geometry of the free surface, the location of the maximum temperature shifts towards the convex portion of the free surface, region (B), as is evident from Fig 4.14(b). The nondimensional value of Θ_{max} is 2.47. The solid/liquid interfaces show moderate curvature at the axis of symmetry (regions C and D) as is evident from Fig 4.14(b).

4.7.4 Thermocapillary Convection

Calculations were conducted for $Gr = 2000$ and two Marangoni numbers, 100 and 200. Figures 4.15(a) and (b) show the streamfunction and isotherms respectively for the case of $Gr = 2000$ and $Ma = 100$. For these values of the parameters, the surface tension gradient, in the form of Marangoni convection, plays a more dominant role than buoyancy, in the form of natural convection, in determining the heat transfer characteristics. Figures 4.16(a) and (b) show the corresponding quantities for $Gr = 2000$ and $Ma = 200$. It is evident that as the Marangoni number increases, the solid/liquid interfaces show increased convexity towards the melt, especially near the axis of symmetry, i.e., in regions (C) and (D). A clockwise convection cell is formed in region (B), adjacent to the convex side of the free surface and an anticlockwise cell in region (A) adjacent to the concave side of the free surface. The location of the maximum temperature is pulled downwards towards region (B) by the

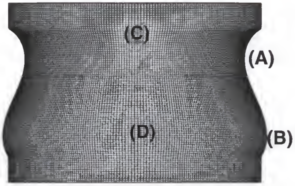

(a) Grid: 161 × 101 points

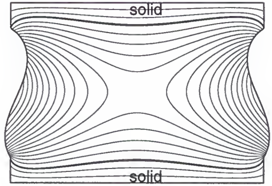

(b) Conduction solution
Min: 0.003 Max: 2.472 20 Contours at uniform intervals

Figure 4.14 (a) Illustrates the grid used. (A) denotes the region adjacent to the concave side of the free surface; (B) denotes region adjacent to the convex side of the free surface; (C) and (D) denote the regions close to the intersection of the solid/liquid interfaces and the centerline as shown.
(b) shows the conduction solution. The solid/liquid interfaces are mildly convex towards the melt in regions (C) and (D) at the centerline and concave close to the free surface at regions (A) and (B).

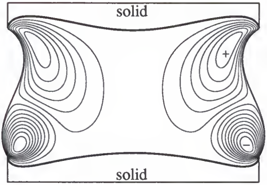

(a) Ma = 100, Streamfunction
Min: –0.851 (-) Max: 0.559 (+) 20 Contours
- denotes clockwise convection and + anticlockwise convection cells.

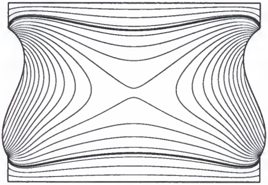

(b) Ma = 100, Isotherms
Min: 0.004 Max: 2.065 20 Contours

Figure 4.15 Ma = 100. (a) Streamfunction: The bold lines indicate the solid/liquid interfaces. The increase in convexity of the interfaces in regions (C) and (D) is evident. There is a clockwise convection cell in region (B) adjacent to the convex side of the free surface and a counterclockwise cell adjacent to the concave side of the interface in region (A). This is because the surface tension decreases with temperature. From (b) the maximum temperature occurs close to the point of inflexion of the free surface. The convex region of the free surface leads to a stronger convection cell.

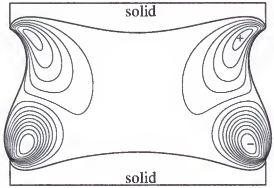

(a) Ma = 200, Streamfunction
Min: –1.349 (-) Max: 0.711 (+) 20 Contours
- denotes clockwise convection and + anticlockwise convection cells.

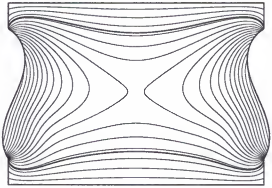

(b) Ma = 200, Isotherms
Min: 0.006 Max: 1.887 20 Contours

Figure 4.16 Ma = 200. The convex region of the free surface leads to a stronger convection cell in region (B). Therefore the clockwise cell is much stronger than the counterclockwise cell in region (A). The location of maximum temperature is pulled downwards towards (B) by the clockwise convection cell. The magnitude of maximum temperature has decreased significantly due to increased heat transport by the convection cells. Decreased heat transfer to the center caused increased convexity of the solid/liquid interfaces near the centerline and increased distortion near the free surface due to the tangential heat transport at the free surface.

stronger recirculation of the clockwise convection cell, which in turn is caused by the stronger surface temperature gradients there. As the convection strength increases with the Marangoni number, the magnitude of the maximum temperature decreases due to the increased heat transfer effectiveness. Increasing the strength of Marangoni convection causes the heat transport to be tangential to the free surface. As a consequence of the decreased heat transfer in the normal direction, the centerline experiences a lower temperature. The increasing temperature inhomogeneity due to this type of convection pattern results in increased curvature of the solid/liquid interfaces and decreasing volume of the melt. The trend is clearly demonstrated by the centerline temperatures shown in Fig. 4.17(a), which shows that the centerline temperatures decrease with increasing Marangoni number, and from Fig. 4.17(b), which shows increasing curvature of the solid/liquid interfaces as a result. The overall effect of Marangoni convection is to increase the temperature inhomogeneity of the melt, especially in the radial direction, causing the solid/liquid interfaces to experience increased curvature towards the melt.

The above series of calculations demonstrate the application of the enthalpy method and its effectiveness in treating problems with complex geometry and involving the interaction of the solidification interfaces with a deformable free surface. It is shown that surface tension gradients generate strong convection in the vicinity of the free surface which significantly affects the heat transfer characteristics and interact with the phase change dynamics. The resulting increases in the curvature of the crystal/melt interface will have a significant impact on crystal quality.

4.8 Concluding Remarks

In this chapter, alternative numerical formulations of the enthalpy method have been developed and assessed for the computation of phase change of pure materials. It is shown that enthalpy formulation and its implementation in terms of the T–based method can efficiently capture the melt/solid interface with adequate resolution. Convective heat transfer in the liquid phase has also been taken into account. A variety of problems relating

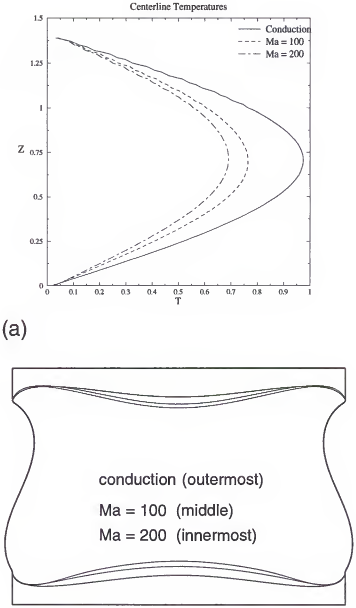

(b) Interface shapes

Figure 4.17. Centerline temperatures are reduced in the melt as the Marangoni number increases as is evident from (a). The solid-liquid interface is drawn inward towards the melt at the centerline but pushed towards the solid near the free surface as the Marangoni number increases, as shown in (b). Marangoni convection causes the heat flux to move tangentially to the interface and decreases the heat transported to the interior. This causes the interface to distort and become convex towards the melt, as the Marangoni effect becomes stronger.

to melting and solidification have been considered – melting of gallium in a cavity and float zone growth of NiAl single crystals – all of which are of immense practical importance. The calculations in this chapter also form the framework for a more extensive and detailed consideration of the float zone process in the next chapter.

CHAPTER 5
MOVING BOUNDARY COMPUTATION OF FREE SURFACE FLOW AND SOLIDIFICATION IN FLOAT ZONE PROCESSING

5.1 Introduction

In this chapter a numerical methodology has been developed to treat fluid flow and heat transfer in the float zone process for single crystal growth. A moving boundary approach has been developed to handle the free surface between the melt and ambient gas. The solidification interfaces between the growing crystal and its melt have been treated using the enthalpy method discussed in Chapter 4 as opposed to the explicit interface tracking employed by studies described earlier in Chapter 1. The enthalpy method makes it unnecessary to explicitly track the solid–liquid interfaces, thus the grid generation requirements are less stringent. The free surface has been computed by solving the dynamic form of the Young–Laplace equation coupled with a mass conservation condition. The SIMPLE algorithm in body–fitted coordinates (Shyy 1994) has been utilized to solve the convective heat transport problem.

5.2 Governing Equations and Boundary Conditions

5.2.1 Transport Processes

The Navier–Stokes equations of continuity, momentum and energy can be written in a cylindrical coordinate system and specialized to the axisymmetric case as follows:

continuity:
$$\frac{\partial(\varrho r)}{\partial t} + \frac{\partial(\varrho r u)}{\partial r} + \frac{\partial(\varrho r v)}{\partial y} = 0 \qquad (5.1a)$$

r–momentum:

$$\frac{\partial(\varrho r u)}{\partial t} + \frac{\partial(\varrho r u u)}{\partial r} + \frac{\partial(\varrho r u v)}{\partial y} = -\, r\,\frac{\partial p}{\partial r} + \left[\frac{\partial}{\partial r}\left(\mu r \frac{\partial u}{\partial r}\right) + \frac{\partial}{\partial y}\left(\mu r \frac{\partial u}{\partial y}\right)\right] - \frac{2\mu u}{r} - Ar(u - u_{cast}) \tag{5.1b}$$

y–momentum

$$\frac{\partial(\varrho r v)}{\partial t} + \frac{\partial(\varrho r u v)}{\partial r} + \frac{\partial(\varrho r v v)}{\partial y} = -\frac{\partial(r p)}{\partial y} + \left[\frac{\partial}{\partial r}\left(\mu r \frac{\partial v}{\partial r}\right) + \frac{\partial}{\partial y}\left(\mu r \frac{\partial v}{\partial y}\right)\right] - \left(\varrho - \varrho_{ref}\right) r g - Ar(v - v_{cast}) \tag{5.1c}$$

energy:

$$\frac{\partial(r \varrho C_p T)}{\partial t} + \frac{\partial(r \varrho C_p u T)}{\partial r} + \frac{\partial(r \varrho C_p v T)}{\partial y} = \left[\frac{\partial}{\partial r}\left(k r \frac{\partial T}{\partial r}\right) + \frac{\partial}{\partial y}\left(k r \frac{\partial T}{\partial y}\right)\right] - L\left[\frac{\partial(\varrho r f)}{\partial t} + \frac{\partial(\varrho r u f)}{\partial r} + \frac{\partial(\varrho r v)}{\partial y}\right] \tag{5.1d}$$

where the source terms in the energy equation arise from the enthalpy formulation for phase change problems (Shyy 1994). The effect of property variation in the domain has been taken into account and the properties in the mushy zone are given by,

thermal conductivity: $$k_{mush} = f\, k_l + (1 - f)\, k_s \tag{5.2a}$$

density: $$\varrho_{mush} = f\, \varrho_l + (1 - f)\, \varrho_s \tag{5.2b}$$

where the subscripts ‘l’ and ‘s’ indicate the liquid and solid phases respectively and f is the liquid fraction. The D’arcy law term is used to drive the velocities in the solid to equal the casting or pulling rate given by $\vec{v}_{cast}$. The D’arcy coefficient is given by,

$$A = C\left(\frac{1 - f^2}{f^3 + q}\right) \tag{5.2c}$$

where C is a large number and q is a small number. For a pure material they can be chosen quite arbitrarily so as to drive the velocity in the solid region to the casting rate while retaining numerical stability. The liquid fraction is modeled as a linear function of the temperature within the phase change interval and is set to zero in the solid

$$f = \begin{cases} 0 & , \quad T < T_s \\ \dfrac{T - T_s}{2\,\varepsilon} & , \quad T_s \leq T \leq T_l \\ 1 & , \quad T > T_l \end{cases} \tag{5.2d}$$

and unity in the liquid. For a pure material, the phase change interval, 2ε, is chosen so as to spread the numerical mushy zone over one or two computational cells in order to achieve numerical stability. As regards the numerical implementation, a choice of either the T–based or the H–based method is available. All the calculations in this work employ the T–based method.

5.2.2 Boundary Conditions

5.2.2.1 Thermal Boundary Conditions

Heat transfer to the system is controlled by radiation and convective transfer from the ambient, i.e.,

$$-\,k\nabla T \cdot \hat{n}\big|_{r=R} = h\left(T - T_{amb}\right) + \varepsilon\sigma\left(T^4 - T_{amb}^4\right) \tag{5.3a}$$

where $r = R$ designates the surface of the melt/crystal/feed system. T_{amb} is the imposed temperature distribution due to the heater. Following Duranceau and Brown (1986) and Lan (1994), T_{amb} is modeled as a gaussian distribution given by

$$T_{amb} = \left(T_p - T_\infty\right) \exp\left(-\left(\frac{y - y_p}{a}\right)^2\right) + T_\infty \tag{5.3b}$$

where T_p is the heater temperature located at position y_p, T_∞ is the ambient temperature far away from the heater and a is the half width of the distribution.

5.2.2.2 Free Surface Treatment

For liquids bounded by a free or deformable boundary where a temperature gradient exists along the interface, a surface shear stress is generated by the surface tension gradient. Thus, the force balance can be written as,

$$\mu\ \nabla\ (\vec{V} \cdot \vec{t}) \cdot \vec{n} = \frac{\partial\gamma}{\partial T}\ \nabla T \cdot \vec{t} \tag{5.4a}$$

where the surface tension gradient is proportional to the temperature gradient and gives rise to the normal derivative of the tangential velocity at the free surface. $\vec{V}$ is the velocity vector, $\vec{n}$ is the unit normal vector to the free surface, and $\vec{t}$ is the unit tangent vector to the free surface. The convection strength is described, in nondimensional terms, by the Marangoni number,

$$\mathrm{Ma} = \left|\frac{d\gamma}{dT}\right| \frac{\Delta T\, r_b}{\mu\, \alpha} \tag{5.4b}$$

which is obtained by nondimensionalizing Eq. (5.4a) with a temperature scale, ΔT, length scale, r_b, and a velocity scale given by α / r_b, where α is the thermal diffusivity of the melt and μ is its viscosity. This dimensionless parameter represents the strength of the velocity gradients generated by the shear stress due to the surface tension gradient.

The velocity boundary conditions for the momentum equations are obtained by solving Eq. (5.4a), in conjunction with the fact that the meniscus is a material surface, i.e.,

$$\frac{\partial F}{\partial t} + u\frac{\partial F}{\partial r} + v\frac{\partial F}{\partial y} = 0 \tag{5.5a}$$

where $F(x, y, t) = 0$ describes the equation of the meniscus. This can be written as,

$$\vec{V} \cdot \hat{n} = 0 \tag{5.5b}$$

in a moving grid system generated to fit a moving and deforming meniscus. Equations (5.4a) and (5.5b) are solved simultaneously to obtain the boundary velocities at the free surface.

5.2.2.3 Symmetry

Since axisymmetry is assumed, the centerline is taken to a symmetry boundary. Thus, at $r = 0$,

$$\begin{aligned} u &= 0 \\ \frac{\partial v}{\partial r} &= 0 \\ \frac{\partial T}{\partial r} &= 0 \end{aligned} \tag{5.6}$$

5.2.3 Governing Equations for a Deformable Meniscus

The meniscus shape obeys the Young–Laplace equation obtained by balancing the hydrostatic pressure, hydrodynamic pressure and viscous normal stress terms against the surface tension force, i.e.,

$$\Delta\varrho\ g\ y - p_L - p_d + 2\mu\frac{\partial v_n}{\partial n} = \gamma(T)\left[\frac{r''}{(1 + r'^2)^{3/2}} - \frac{1}{r\ (1 + r'^2)^{1/2}}\right] \quad (5.7a)$$

where $r = r(y)$ describes the free surface shape. Here, $\Delta\varrho$ is the density difference between the melt and the ambient fluid, g is the acceleration due to gravity, γ is the temperature dependent surface tension between the melt and the ambient fluid. The term on the right hand side represents the product of the temperature dependent surface tension and the free surface curvature. The left hand side represents the hydrostatic pressure, the hydrodynamic pressure, P_d, and the viscous normal stress generated by the fluid motion. In addition, there is a pressurization parameter, P_L, that must be determined as part of the solution either by satisfying a contact angle condition at the solidifying interface or by a mass conservation constraint.

The dynamic form of the Young–Laplace equation, Eq. (5.7a), can be nondimensionalized as follows:

$$\mathrm{Bo}\,Y - \mathrm{We}\,P_d - P_L + \mathrm{Ca}\frac{\partial V_n}{\partial n} = \left(1 - \left|\frac{d\gamma}{dT}\right|\frac{\Delta T}{\gamma_o}\right)\left[\frac{R''}{(1 + R'^2)^{3/2}} - \frac{1}{R(1 + R'^2)^{1/2}}\right] \quad (5.7b)$$

where the Bond number, Bo, is defined as

$$\mathrm{Bo} = (\Delta\varrho\ g\ r_b^2)/(\gamma_0) \quad (5.8a)$$

describes the force balance between the hydrostatic pressure and the surface tension, the Weber number, We,

$$\mathrm{We} = (\varrho\ \alpha^2)/(\gamma_0\ r_b) \quad (5.8b)$$

describes the relative magnitudes of the inertia and surface tension, and the Capillary number, Ca,

$$Ca = (2\ \mu\ \alpha)/(\gamma_o\ r_b) \tag{5.8c}$$

describes the relative magnitudes of the viscous normal stress and the surface tension. Here, α is the thermal diffusivity of the melt, μ is the viscosity of the melt and r_b is a characteristic length scale typically taken to be radius of the melting feed.

Equation (5.7a) may be solved with the following boundary conditions:

(i) Fixed radius at the melting feed.

$$r(y = h_c) = r_b \tag{5.9}$$

and either

(ii) Fixed radius at the solidifying crystal,

$$r(y = 0) = r_c \tag{5.10a}$$

or fixed contact angle at the solidifying crystal

$$r'(y = 0) = \tan(\pi/2 - \phi_c) \tag{5.10b}$$

assuming downward pulling as is the case in the problem considered subsequently. Equation (10a) has been used in all the cases considered in this study for the purpose of comparison with the solutions available in literature. Here, $y = 0$ describes the location of the melting feed and $y = h_c$ is the height of the meniscus, ϕ_c is the contact angle between the meniscus and the solidifying crystal and r_c is the radius of the growing crystal.

5.3 Moving Grid Transformation

Equations (5.1a–d) are transformed into a moving grid body fitted coordinate system as follows:

The transformation may be expressed as

$$\begin{aligned} \xi &= \xi(x, y, t) \\ \eta &= \eta(x, y, t) \end{aligned} \tag{5.11a}$$

The continuity equation in nonorthogonal coordinates then becomes,

$$\frac{\partial}{\partial t}(Jr\varrho) + \frac{\partial(\varrho rU)}{\partial \xi} + \frac{\partial(\varrho rV)}{\partial \eta} = 0 \tag{5.11b}$$

where r is the radial coordinate which is identical to x in the following treatment. The separation between r and x is maintained for the ease of application to a two dimensional Cartesian coordinate system as opposed to a cylindrical coordinate system considered here.

$$\begin{aligned} U &= (u - \dot{x})\, y_\eta - (v - \dot{y})\, x_\eta \\ V &= (v - \dot{y})\, x_\xi - (u - \dot{x})\, y_\xi \end{aligned} \tag{5.11d}$$

are the contravariant velocity components and $\dot{x}$ and $\dot{y}$ are the radial and vertical components of the grid velocity vector respectively. The determination of the Jacobian, J, will be explained subsequently. The momentum equations then become

r–momentum:

$$\begin{aligned} \frac{\partial(J\varrho ru)}{\partial t} + \frac{\partial(\varrho rUu)}{\partial \xi} + \frac{\partial(\varrho rVu)}{\partial \eta} = -\left\{ r y_\eta \frac{\partial p}{\partial \xi} - r y_\xi \frac{\partial p}{\partial \eta} \right\} &+ \\ \frac{\partial}{\partial \xi}\left[\frac{\mu}{J} r \left(q_1 u_\xi - q_2 u_\eta \right) \right] &+ \\ \frac{\partial}{\partial \eta}\left[\frac{\mu}{J} r \left(q_2 u_\xi - q_3 u_\eta \right) \right] + S_u(\xi, \eta) \cdot J \cdot r & \end{aligned} \tag{5.11e}$$

y–momentum:

$$\begin{aligned} \frac{\partial(Jr\varrho v)}{\partial t} + \frac{\partial(\varrho rUv)}{\partial \xi} + \frac{\partial(\varrho rVv)}{\partial \eta} = -\left\{ x_\xi \frac{\partial(rp)}{\partial \eta} - x_\eta \frac{\partial(rp)}{\partial \xi} \right\} &+ \\ \frac{\partial}{\partial \xi}\left[\frac{\mu}{J} r \left(q_1 v_\xi - q_2 v_\eta \right) \right] + \frac{\partial}{\partial \eta}\left[\frac{\mu}{J} r \left(q_2 v_\xi - q_3 v_\eta \right) \right] &- \\ \left(\varrho - \varrho_{ref} \right) g \cdot J \cdot r + S_v(\xi, \eta) \cdot J \cdot r & \end{aligned} \tag{5.11f}$$

along x and y directions respectively, where x_η, y_η and so on are the metrics of the transformation and q_1, q_2 and q_3 are defined as

$$\begin{aligned} q_1 &= x_\eta^2 + y_\eta^2 \\ q_2 &= x_\xi x_\eta + y_\xi y_\eta \\ q_3 &= x_\xi^2 + y_\xi^2 \end{aligned} \tag{5.11g}$$

Following Shyy (1994), the metric terms x_η, y_η and so on are evaluated as the projected lengths of the control volume in the physical space in order to ensure conservative treatment.

5.3.1 Determination of the Jacobian

The Jacobian of the transformation is defined as,

$$J = x_\xi y_\eta - x_\eta y_\xi \tag{5.12}$$

which can be interpreted as the volume of the computational cell (Shyy 1994). However, in a moving grid system, the Jacobian has to satisfy the geometric conservation law which can be derived by considering the transformed continuity equation. Consider an uniform flowfield with $\varrho = 1$, $u = 1$ and $v = 1$. Such a flowfield identically satisfies the continuity equation (1a) and is required to satisfy the transformed continuity equation (5.11b). Equation (5.11b) then becomes

$$\frac{\partial[Jr]}{\partial t} + \frac{\partial\left[r\left(\dot{y}\,x_\eta - \dot{x}\,y_\eta\right)\right]}{\partial\xi} + \frac{\partial\left[r\left(\dot{x}\,y_\xi - \dot{y}\,x_\xi\right)\right]}{\partial\eta} = 0 \tag{5.13}$$

The Jacobian is thus computed by a backward Euler difference in time based on the geometric quantities such as the radial coordinate and the metric as shown above. The methodology is an extension of the procedure described in Shyy et. al. (1996) to the cylindrical coordinate system.

5.4 Computational Methodology

5.4.1 Meshing Procedure

For moving boundary problems like the float–zone simulation, it is essential to maintain an adequate resolution in the liquid zone, even as the grid deforms to track the changing geometry. Adequate resolution in the liquid zone is necessary in order to (a) stabilize the calculation, (b) maximize the accuracy of the convective heat transfer and phase change computations, and (c) accurately capture the meniscus deformation and faithfully represent the curved geometry of the domain. At the same time, it is desirable that the grid generation process be fast and robust, i.e., ensure that the grid distribution is smooth, avoid excessive skewness, allow good control of the grid spacing and that the mapping between the physical domain and the computational domain is invertible.

In this work, a block structured approach with an algebraic grid generation procedure has been taken to enable fast grid generation. A typical float–zone domain can be divided into three logical subdomains: (a) the crystal, (b) the melt and (c) the feed rod, as illustrated in Fig. 5.1. Subdomains (a) and (c) are highly stretched to fit the long crystal and the feed rod. Thus, the material in subdomains (a) and (b) is entirely solid during the solution process. Subdomain (b), however, encloses the melt zone. Thus, phase change and convective heat transfer occur entirely in subdomain (b). It is also to be noted that subdomain (b) has an $\mathcal{O}(1)$ aspect ratio which dictates the choice of the interpolation and distribution functions chosen for the algebraic grid generation procedure.

Due to the varying and sometimes conflicting requirements listed above, the grid in each block or subdomain is generated separately and subsequently assembled together into a single grid system to continue the solution procedure. In each subdomain, the grid is generated algebraically by using appropriate interpolation functions and distribution parameters, checked for integrity and only then is the assembly procedure invoked to create a single grid system. The algebraic generation procedure is relatively inexpensive; as opposed to the solution of quasi–linear elliptic equations and has been found to be robust as

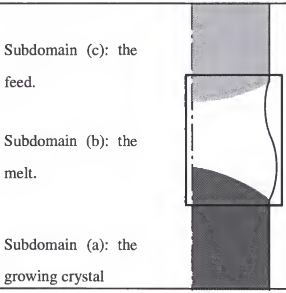

Figure 5.1 Illustration of the domain and its partition into three blocks for the purpose of grid generation. Block 2 enclosing the phase change region is boxed for illustration. The extent of block 2 into the solid regions can be adjusted to track the height variation of the zone.

well in the present problem. However, careful choice of the distribution parameters and interpolation functions is necessary to ensure smoothness and concentration of grid lines close to the interfaces.

The calculation domain is divided into contiguous, non–overlapping blocks and the meshing procedure is carried out separately in each block. For convenience, it is required that each block consist only of four sides. The sides may be specified either as straight lines or by sequence of (x,y) pairs describing a curve. The curve may be specified or computed; the only requirement is that it does not intersect itself. For instance, in the melt zone, the meniscus shape is computed by numerically integrating the dynamic form of the Young–Laplace equation. The detailed procedure is as follows:

(a) Divide the domain into contiguous blocks of four sides each. Each block is described by a non–intersecting curve. For the float–zone calculations, it is convenient to divide the domain into three blocks; the first block consisting of the crystal, the second block consisting of the feed rod and the third block enclosing the melt and the phase change region.

(b) For each side, compute the arclength from the sequence of (x,y) pairs describing the curve. The required number of grid points are then distributed along the arclength of each side as illustrated in Fig. 5.2. A variety of choices exist for the distributing function. In this study, it was found convenient to use cubic and exponential clustering functions depending on the geometry of the individual block. The cubic polynomial allows a fixed number of grid points to be distributed with specified end points as well as specified end spacings. The exponential clustering is suitable for highly stretched subdomains, allowing the end points to be matched alongwith the spacing at one end. The spacing at the other end is determined by the function. The exponential clustering is described by

$$\frac{s - s_1}{s_N - s_1} = \frac{\exp(\alpha\ \xi) - 1}{\exp(\alpha) - 1} \tag{5.14a}$$

where $\xi = \frac{i - 1}{N - 1}$, N being the number of grid points that need to be accommodated within $s_1 \leq s \leq s_N$. The coefficient, α, is determined by specifying the spacing at one end, i.e. as

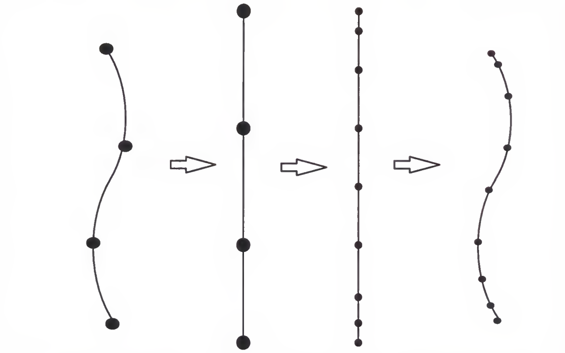

Figure 5.2 Illustration of the transformation procedure to achieve the desired distribution of grid points along the arclength of the boundary.

the root of

$$\frac{\Delta s_1}{s_N - s_1} = \frac{\exp(\alpha\,\Delta\xi) - 1}{\exp(\alpha) - 1} \tag{5.14b}$$

where the root is determined by an iterative procedure. The quantities ξ and η are the transformed and normalized coordinates in the computational plane and are defined as,

$$\xi = \frac{i - 1}{N_i - 1} \tag{514c}$$

and

$$\eta = \frac{j - 1}{N_j - 1} \tag{14d}$$

where N_i is the number of grid points along the ξ direction and N_j the number of grid points along the η direction. The ability to match the spacing at one end allows a smooth variation of the grid spacing between the different subdomains.

(c) The resulting boundary distribution is then verified by ensuring that all the newly formed arclength elements have a positive length. This step is necessary when using high order polynomials such as the cubic clustering because of potentially oscillatory behavior between the colocation points.

(d) The newly formed arclength distribution is mapped back to the x–y plane via cubic spline interpolation. This completes the generation of the boundary distribution for each subdomain.

(e) The internal grid distribution is generated for each block by transfinite interpolation. For transfinite interpolation, use of linear basis functions has been found to be robust and efficient. The quality of the grid is determined mostly by the boundary distribution since using low order interpolation polynomials does not give rise to oscillatory tendencies. The disadvantage is that it is does not provide additional control of the interior grid distribution which is necessary to ensure grid orthogonality.

$$\begin{aligned}\vec{r}(\xi,\eta) = {} & \xi\, \vec{r}(0,\eta) + (1-\xi)\, \vec{r}(1,\eta) + \\ & \eta\, \vec{r}(\xi,0) + (1-\eta)\, \vec{r}(\xi,1) - \xi\, \eta\, \vec{r}(0,0) - \\ & \xi\, (1-\eta)\, \vec{r}(0,1) - (1-\xi)\, \eta\, \vec{r}(1,0) - \\ & (1-\xi)\, (1-\eta)\, \vec{r}(1,1)\end{aligned} \tag{5.15}$$

where $\vec{r} = x\, \hat{i} + y\, \hat{j}$

(f) The grid is checked for zero Jacobians and convexity of the control volumes. Loss of convexity implies excessive distortion of the quadrilateral that constitutes the control volume. Loss of convexity is tested by taking the cross product of pairs of adjacent sides of the control volume and ensuring that the angle between them is not greater than π radians. Appropriate error recovery measures, described later, are taken if such situations are encountered.

(g) The various subdomains are combined together to form a single grid.

5.4.2 Deformable Meniscus

The meniscus shape is computed by integrating the dynamic Young–Laplace equation described earlier. As shown in Fig. 5.3, the meniscus is discretized into finite domains on the underlying grid points. The dynamic Young–Laplace equation is then integrated over the finite domains in a manner analogous to the discretization of the transport equations over the

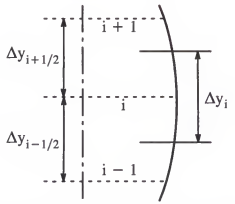

Figure 5.3 Illustration of the differencing procedure for the Young–Laplace equation.

control volume. The derivatives in the equation are approximated by piecewise linear interpolation functions effectively giving rise to a second order central difference scheme for all the terms in the dynamic Young–Laplace equation.

The discretized dynamic form of equation (5.7a) can now be written in the form

$$\mathrm{ap}\ r_i = \mathrm{as}\ r_{i-1} + \mathrm{an}\ r_{i+1} + b \tag{5.16a}$$

in the notation popularized by Patankar (1980), where

$$\mathrm{as} = \frac{\gamma}{\Delta y_{i-1/2} \left(1 + r'^2\right)^{3/2} \Big|_{y\,=\,y_{j-1/2}}} \tag{5.16b}$$

$$\mathrm{an} = \frac{\gamma}{\Delta y_{i+1/2} \left(1 + r'^2\right)^{3/2} \Big|_{y\,=\,y_{j+1/2}}} \tag{5.16c}$$

$$\mathrm{ap} = \mathrm{as} + \mathrm{an} \tag{5.16d}$$

and the source term is given by

$$b = \varrho_i\, g \left[\frac{y_{i+1}}{4} + \frac{y_{i-1}}{4} + \frac{y_i}{2} - y_{\mathrm{ref}}\right] - P_{d_i} - P_L + \frac{\gamma}{r_i \left(1 + r'^2\right)^{1/2} \Big|_{y=y_i}} \tag{5.16e}$$

where all the first derivative terms, r′, are evaluated using central differences over the nearest half grid points and the term P_{d_i} includes the contribution from the inertia and viscous stress effects due to melt convection.

The equation system (5.16) is conveniently solved using a tridiagonal solver. However, since the coefficients are non–linear, successive substitution is employed as the outer iteration. During the course of the iterations, underrelaxation is employed to ensure convergence. Underrelaxation is first applied to the non–linear first derivative terms,

$$r'^{k} = \omega_r \, \delta r^k + (1 - \omega_r) \, r'^{k-1} \tag{5.17a}$$

where k denotes the iteration number. Underrelaxation is also applied to the shape update as follows:

$$ap = ap/\omega_m \tag{5.17b}$$

$$b = b + (1 - \omega_m) \, ap \, r_i \tag{5.17c}$$

to ensure diagonal dominance before solving the tridiagonal system.

5.4.2.1 Convergence Criteria

Convergence criteria for terminating the non–linear iterations consists of examining the residuals summed over the entire field as well as the 1–norm of the solution variation with iterations. The residual is always scaled/normalized by the solution and is defined as,

$$\text{Res} = \sum_i \left[\frac{an \, r_{i+1} + as \, r_{i-1} - ap \, r_i + b}{ap} \right] \Big/ \sum_i | \, r_i \, | \tag{5.18}$$

The 1–norm is defined as,

$$\| \, r \, \| = \frac{\sum_i | \, r_i^k - r_i^{k-1} |}{\sum_i | \, r_i^{k-1} |} \tag{5.19}$$

and is an auxillary indicator of convergence. Both, the residual averaged over the total number of control volumes, as well as the L_1–norm are required to be less than 10^{-4}.

5.4.2.2 Global Mass Conservation

Meniscus shapes are determined by adjusting the value of P_L so as to satisfy the constraint of global mass conservation. In this study, a target domain mass is determined by considering the domain to be initially a solid cylinder. As melting progresses, a mass deficit builds up due to density differences between the melt and the solid. The meniscus shape is adjusted to reduce the mass deficit to zero via manipulation of P_L.

First, the mass deficit is determined,

$$\Delta M = M_{domain} - \int_{Vol} \varrho \, dV \tag{5.20}$$

The meniscus is then required to satisfy a volume constraint,

$$V_m = \pi \int r \, dy + \frac{\Delta M}{\varrho_l} \tag{5.21}$$

The required value of P_L is determined by finding the root of

$$\mathcal{F}(P_L) = V_m - \pi \int r \, dy = 0 \tag{5.22}$$

5.4.2.3 Root Finding Procedure

(i) The root is bracketed between two extreme values of P_L by a linear search for a zero crossing of $\mathcal{F}(P_L)$. It is helpful to carry out exploratory computations to arrive at reasonable guess values for the step size as well as the initial guess for P_L.

(ii) The secant method is used to locate the root. If a pathalogical situation is encountered where the secant method does not converge, the procedure automatically switches over to the bisection method.

5.4.2.4 Remeshing Procedure

Once a meniscus profile is obtained satisfying the dynamic form of the Young–Laplace equation and the global mass conservation constraint, the domain has to be remeshed as the grid moves to fit the meniscus. It is possible to underrelax the grid movement in order to stabilize the transport calculations. Again, an algebraic procedure is adopted whereby the x–coordinates of the control volumes are determined by using transfinite interpolation.

(i) Carry out linear transfinite interpolation to determine the x–coordinates of the grid points using the x–component of Eq. (15).

(ii) Check the grid for zero Jacobians and loss of convexity of the control volumes. The error recovery procedure is described next.

5.4.3 Error Recovery

It is possible to encounter zero Jacobians during the iterative process if the height of the zone decreases so that the grid gets excessively squashed. In such a case, the algorithm prints a warning message and continues the calculations without updating the grid. To prevent this from occurring it is possible to specify a minimum zone height below which the vertical component of grid motion is suppressed. Loss of convexity usually occurs if the meniscus computation diverges due lack of existence of solutions in the required parameter range – especially if the zone height becomes excessively large. An appropriate parameter range can be approximately determined by solving the static form of the Young–Laplace equation to generate an existence map over the desired parameter range and utilizing such a map to generate appropriate initial guesses. Such a procedure will be described in detail in the results section.

5.4.4 Grid Underrelaxation

It will be demostrated later that grid underrelaxation is necessary in order to ensure a smooth and oscillation free convergence history. The vertical and radial components of the grid deformation are underrelaxed separately and the corresponding underrelaxation parameters are denoted by ω_r and ω_y respectively. Typical values of ω_r range from 0.4 to 0.7 depending on the estimated height of the melt zone. The vertical component, however, needs to be underrelaxed substantially. The value of ω_y has been varied from 0 (no deformation in the y–direction) to 1 (no underrelaxation) in an attempt to quantify its effect on the solution history. Typical values used are in the range of 0.05 to 0.1 to ensure convergence of the solution. Care is taken to ensure that the melt zone is completely enclosed by the refined grid region comprising subdomain (b) as illustrated in Fig. 1 by tracking the location of the subdomain boundaries with respect to the phase boundaries during the iterative process and also by an a posteriori estimation after the solution has been obtained.

5.5 Results and Discussion

5.5.1 Test Problem

The test problem used to develop and test the algorithm is the float zone growth of Sodium Nitrate crystal ($NaNO_3$) crystals heated using a ring heater. The steady state solutions for pure heat conduction, meniscus shapes, natural and Marangoni convection are available in literature (Lan and Kou 1990a, 1991a) and Lan (1994). These solutions provide a reference point for comparison and assessment.

An initially cylindrical rod of $NaNO_3$ is heated at the center by radiation from a ring heater which causes it to start melting and form a float zone. The meniscus deformation depends on the length of the molten zone and also on the density change during melting as the meniscus deforms to conserve mass. The rod is then pulled downwards to simulate the crystal growth processes. Since the length of the rod is set to 40 times its radius, the melt zone occupies only a small fraction of the domain. The physical properties of $NaNO_3$ are shown in table 5.1. Other relevant geometrical and physical parameters are presented in table 5.2. In order to accommodate the enthalpy method, the melting temperature is distributed over a finite phase change interval given by

$$2\varepsilon = 0.2\,\mathrm{K} \tag{5.23}$$

5.5.2 Nondimensional Parameters

The material properties and the geometrical parameters presented in tables 5.1 and 5.2 above enable the estimation of important nondimensional parameters for the system. Based on an estimated temperature scale, $\Delta T = T_{max} - T_m = 20\mathrm{K}$, length scale, $r_b = 0.2\mathrm{cm}$, and the material properties given in table 5.1, the following nondimensional parameters can be obtained:

Prandtl number $\quad \mathrm{Pr} = \frac{\nu}{\alpha} = 9.2$

Grashof number $\quad \frac{g\beta\Delta T r_b^3}{\nu^2} = 411$

Rayleigh number $\quad \mathrm{Ra} = \mathrm{Gr}\,\mathrm{Pr} = 3781$

Table 5.1. Physical properties of $NaNO_3$	
Melting temperature, T_m	579.8 K
Latent heat, L	$182\ J\ g^{-1}$
Thermal conductivity (solid), k_s	$5.65 \times 10^{-3} + 33.5\ (T - 503) \times 10^{-7}\ W\ cm^{-1}\ K^{-1}$
Thermal conductivity (liquid), k_l	$5.65 \times 10^{-3} + 33.5\ (T - T_m) \times 10^{-7}\ W\ cm^{-1}\ K^{-1}$
Specific heat, $C_{ps} = C_{pl}$	$1.255 + 2.18\ (T - 373) \times 10^{-3}\ J\ g^{-1}\ K^{-1}$
Surface tension gradient, $\partial\gamma/\partial T$	$-0.056\ dyn\ cm^{-1}\ K^{-1}$
Surface tension, γ	$119.96 - 0.056\ (T - T_m)\ dyn\ cm^{-1}$
Dynamic viscosity, μ	$0.0302 - 1.533 \times 10^{-4}\ (T - T_m)\ g\ cm^{-1}\ s^{-1}$
Thermal expansion coefficient, β	$6.6 \times 10^{-4}\ K^{-1}$
Density (solid), ϱ_s	$2.118\ g\ cm^{-1}$
Density (liquid), ϱ_l	$1.904\ g\ cm^{-1}$

Table 5.2. Geometrical and physical parameters	
r_b (radius)	0.2 cm
y_p (heater location)	4.0 cm
a (width of heater profile)	0.3 cm
T_∞	298 K
T_p (heater temperature)	813 K, 913 K
ε (emissivity)	0.7
h (heat transfer coefficient)	$4.6 \times 10^{-4}\ W\ cm^{-2}\ K^{-1}$

Marangoni number $\quad Ma = 4752$

Stefan number $$St = \frac{C_p \Delta T}{\Delta H} = 0.3$$

Bond number $$Bo = \frac{\Delta \varrho g r_b^2}{\gamma_0} = 0.61$$

Capillary number $$Ca = \frac{2\mu\alpha}{\gamma_0 r_b} = 3.8 \times 10^{-6}$$

Weber number $$We = \frac{\varrho\alpha^2}{\gamma_0 r_b} = \ = 2.4 \times 10^{-7}$$

Biot number $\frac{h\ r_b}{k} = 0.02$

Radiation number $\frac{\varepsilon\,\sigma r_b \Delta T^3}{k} = 3.7 \times 10^{-6}$

5.5.3 Steady-State Calculations

A conduction–capillarity solution obtained by setting the heater temperature to 913 K has been chosen to present some of the features of the algorithm and its implementation, and to characterize the interaction between the grid movement, meniscus deformation and heat conduction terms in the discretized energy equation.

5.5.3.1 Estimation of Meniscus Shape and P_L

The meniscus calculations need a starting procedure to determine the initial guesses for the melt zone height and the corresponding guess value of P_L. The procedure is as follows:

(i) Determine an initial estimate of the melt zone height. This was done by computing a pure heat conduction solution for a cylindrical geometry, i.e., with the meniscus shape held fixed.

(ii) Using the guessed height, the static Young–Laplace equation is solved using an adaptive fifth order Runge–Kutta method and the shooting technique to generate all possible profiles over the entire range of P_L for which solutions exist. The relative local error (Shyy 1994) is maintained below 10^{-6} by comparing with the corresponding fourth order Runge–Kutta technique and varying the step size accordingly.

(iii) Figure 5.4(a) shows the map of melt volume, V_m, versus P_L over the entire range of available solutions. It is evident that over the range of interest, two solutions exist even for the static Young–Laplace equation. Figure 5.4(b) shows the meniscus profiles satisfying the volume constraint with a relative tolerance of 10^{-2}.

(iv) Figures 5.4(a) and (b) are used to guide the initial guesses for P_L and the limiting values for the meniscus volume for the float zone computations. Such a procedure ensures operation in the range where the solutions to the Young–Laplace equation exist.

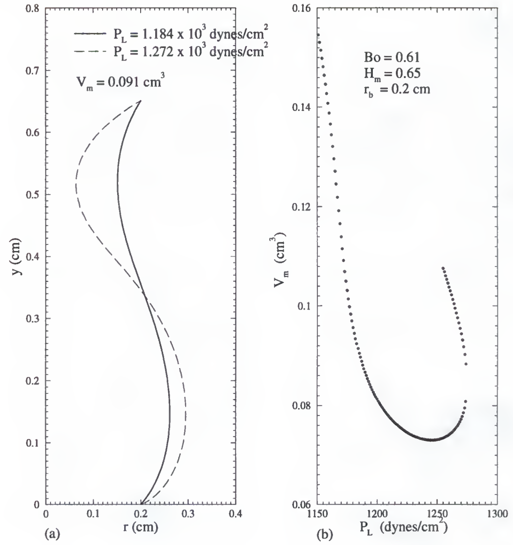

Figure 5.4. Determination of initial guesses for melt zone height and P_L using the shooting method with Runge–Kutta fifth order integration. (a) Profiles satisfying the static Young–Laplace equation and the given melt volume with a relative tolerance of 10^{-2} and local error less than 10^{-6}.
(b) A map of melt volume versus P_L over the entire range of P_L for which the static Young–Laplace equation can be integrated. It is seen that over a significant range of P_L, two solutions exist satisfying a given melt volume constraint.

5.5.3.2 Conduction–Capillarity Solution

Two sets of calculations with different initial guesses and grid underrelaxation parameters were carried out to investigate the coupling between the grid movement, boundary deformation and heat conduction. First, a conduction solution was obtained with the heater temperature set to 913 K and by imposing a cylindrical shape on the meniscus. This was then used as an initial guess for the conduction–capillarity problem which allowed the meniscus shape to deform in accordance with the Young–Laplace equation. No underrelaxation was used when updating the meniscus shape or the grid. Figure NO TAG shows the convergence characteristics of this procedure. Figure 5.5(a) shows the history of the monitored quantities, H_m – the zone height at the free surface, and H_c – the zone height at the centerline. Figures 5.5(b) and (c) show the history of P_L and the melt volume, V_m, respectively. The residual of the energy equation and the 1–norms of the temperature, x, and y components of the grid deformation are shown in Fig. 5.5(d–f). The highly oscillatory trend in the solution characteristics is evident and this procedure cannot yield a solution.

The second set of calculations used an initially solid rod at room temperature, 300 K, as the initial guess. Figure 5.6 shows the effect of various grid underrelaxation factors on the convergence characteristics. Figures 5.6(a–c) shows the history of H_m for grid underrelaxation factors over a range, $0 \leq \omega_y \leq 1$. $\omega_y = 1$ indicates that the vertical component of grid deformation was not underrelaxed and $\omega_y = 0$ indicates that the vertical component of grid deformation was completely suppressed. Figures 5.6(d–f) show the corresponding trends for the quantity H_c. It is evident that grid underrelaxation in the range, $0.1 \leq \omega_y \leq 0.05$ is sufficient to suppress the oscillatory behavior. Complete suppression of the vertical component of grid deformation yields the smoothest but the slowest convergence characteristics.

Figure 5.7 shows the solution features. It is observed that the meniscus profile and the zone height are very close to the profile shown in Fig. 5.4a. The hydrostatic pressure causes the melt to bulge outwards near its base and to 'neck' inwards near the top. Figure 5.7(a)

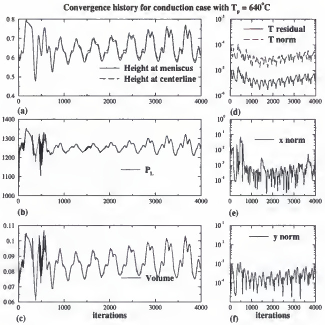

Figure 5.5. Convergence history for the conduction case with $T_p = 913$ K. Effect of initial guess and underrelaxation parameters on the convergence history. A conduction solution was obtained by imposing a cylindrical meniscus shape. The converged solution was then used as the initial guess for the conduction – capillary solution. The grid motion and boundary deformation were not underrelaxed, i.e., $\omega_y = \omega_r = 1$.

shows the computed grid and the free surface shape. Figure 5.7(b) shows the corresponding isotherms. The phase interfaces are illustrated by the thick lines in Fig. 5.7(b). The melt/crystal interface at the base of the zone is quite flat whereas the melt/feed interface at the top is slightly concave towards the melt. Figure 5.8 shows the temperature profiles along the entire height of the domain. The temperature profile at the surface is shown by the solid line and the profile at the centerline is shown by the dashed line. It is observed that the temperature distribution in the solid regions becomes essentially one dimensional away from the melt zone. This confirms the assumption made by Duranceau and Brown (1986) in their conduction–capillarity model which imposed a one dimensional temperature distribution in regions far from the melt zone in order to reduce the computational load. The present

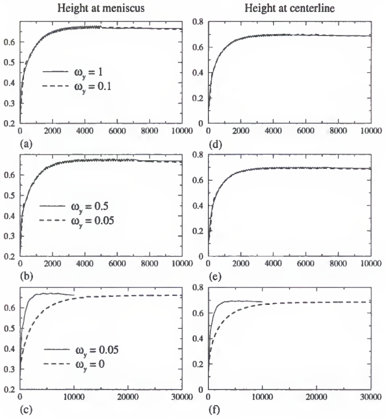

Figure 5.6. Convergence history for the conduction case with $T_p = 913$ K. Effect of initial guess and underrelaxation parameters on the convergence history.
$\omega_r = 0.7$.
(a) – (c) History for H_m for various ω_y.
(d) – (e) History for H_c for the corresponding ω_y.
In (d) and (e), $\omega_y = 0$ indicates that only the x component of grid deformation is permitted. The fixed grid solution is slower to converge, but the solution history is smoother. The initial guess was a solid cylindrical rod at 300 K. Calculations on grid of 41 × 101 points.

computations help to justify this assumption and also designate the regions in which a one dimensional distribution can be prescribed.

5.6 Grid Refinement Study and Assessment

A series of calculations have been conducted with parameters chosen so as to facillitate comparison with the solutions of Lan (1994). The heater temperature was set to 813 K. Starting with the conduction–capillarity solution, the effects of buoyancy induced

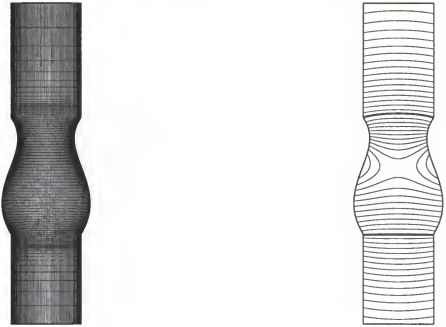

(a) $H_m = 0.665$ cm,
$H_c = 0.685$ cm,
$P_L = 1184$ dynes/cm^2

(b) $\Delta T = 9.98$ K, $T_{max} = 702.17$ K,
$T_{min} = 300.00$ K.

Figure 5.7. Heat conduction solutions with $T_p = 913$ K.
(a) Grid and boundary shape.
(b) Isotherm distribution showing the isotherm distribution on the grid of 41 × 101 points. The interfaces are denoted by the thick lines.

convection and thermocapillary convection have been successively incorporated. For all computations, the convergence history of important quantities such as the height of the zone at the free surface, H_m, the height of the zone at the centerline, H_c, and the heat flux balance has been monitored. These calculations employ the second order accurate central difference scheme for the convection and diffusion terms in the discretized form of the Navier–Stokes equations. These calculations were carried out to assess the present computations with those of Lan (1994) in terms of accuracy and numerical diffusion. The study by Lan (1994) and the other works cited, have used a first order upwind scheme to discretize the convection terms.

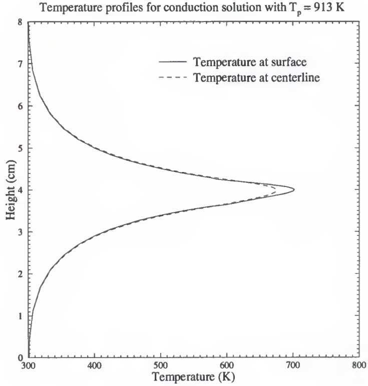

Figure 5.8. Temperature profiles along the height of the domain at the surface and at the centerline. The profiles show that a one dimensional temperature distribution is established in the feed and crystal regions away from the melt region. This confirms the one dimensional approximation used by Duranceau and Brown (1986) in the regions far from the melt.

5.6.1 Grid

Two grids have been used for the accuracy assessment, a grid of 41 × 101 points and a refined grid of 81 × 181 points.

(i) 41 × 101 grid: This grid has 41 points in the radial direction with a spacing of 0.002 cm at the meniscus and 0.008 cm at the symmetry boundary distributed by fitting a cubic polynomial. In the vertical direction, the phase change zone has 61 points distributed by a cubic polynomial with the spacings at each end set to 0.007 cm. The feed and crystal zones have 21 points each, distributed according to the exponential clustering by matching the spacings to the phase change zone. The grid in the phase change zone extends beyond the location of the trijunction points by 0.02 cm.

(ii) 81 × 181 grid: This grid has 81 points in the radial direction with a spacing of 0.001 cm at the meniscus and 0.004 cm at the symmetry boundary distributed by fitting a cubic polynomial. In the vertical direction, the phase change zone has 121 points distributed by a cubic polynomial with the spacings at each end set to 0.003 cm. The feed and crystal zones have 31 points each, distributed according to the exponential clustering by matching the spacings to the phase change zone. The grid in the phase change zone extends beyond the location of the trijunction points by 0.03 cm.

5.6.1.1 Heat Conduction Calculations

The initial guess was a solid cylindrical rod at 300 K. Initially, the meniscus deformation was not permitted and a cylindrical meniscus shape was imposed. A converged solution was obtained for this configuration when the zone height stopped varying and the residual for the energy equation, averaged over the control volumes, was less than 10^{-5}. This was used as the initial guess for the subsequent set of calculations with the meniscus shape computed by integrating the Young–Laplace equation. The zone height is a very sensitive indicator of solution convergence since it occupies a small fraction of the overall length of the domain. Calculations have been carried out with the meniscus shapes computed under both normal and under microgravity (0g) conditions to assess the impact of meniscus shape on the solution. Figure 5.9 shows the convergence history of the solution for the normal gravity case. Figure 5.9(a) and (b) show the history of the zone height – H_m (at the surface) and H_c (at the centerline) for the grid of 41 × 101 points and for the grid of 81 × 181 points, respectively. Figure 5.9(c) and (d) show the history of the heat flux balance in the domain. These plots establish the convergence of the solution.

Figure 5.10 (i) and (ii) show the computed shape and converged grid distribution obtained on the 41 × 101 grid and the 81 × 181 grid respectively. The zone heights and the

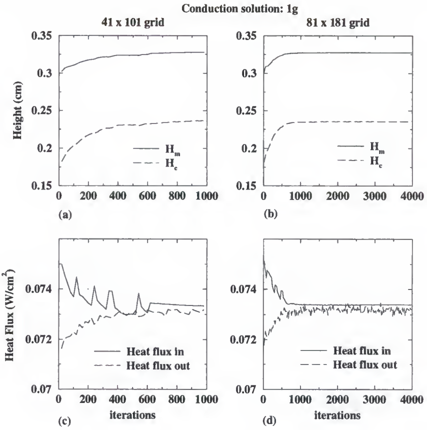

Figure 5.9 Convergence history for the conduction solution at 1g. (a) and (b) height of the zone at the surface and at the centerline for the grid of 41 × 101 points and 81 × 181 points respectively. (c) and (d) balance of the incoming and outgoing heat fluxes for the grid of 41 × 101 points and 81 × 181 points respectively.

maximum temperature, T_{max}, agree to within 0.6% and 0.2% respectively, establishing the grid independent nature of the converged solutions. Figure 5.11 shows the corresponding isotherms and the solid – liquid interfaces are shown by the thick lines. The menicus has a pronounced bulge at the base of the zone due to the combined action of gravity and the density change due to phase change. The solid liquid interfaces show mild convexity towards the melt. The solution on the 41 × 101 grid agrees with the solution of Lan (1994), the difference in T_{max} being less than 0.6%. Figure 5.12 (a) and (b) show that the temperature profiles obtained on the 41 × 101 grid and the 81 × 181 grid are identical. Figure 5.12(c)

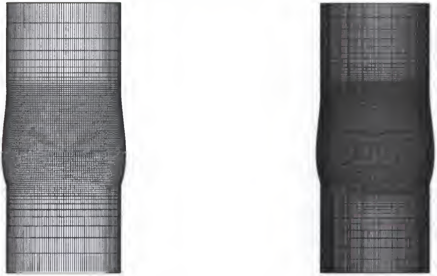

(i) $H_m = 0.328$ cm, $H_c = 0.236$ cm.

(ii) $H_m = 0.328$ cm, $H_c = 0.234$ cm.

Figure 5.10 Computed grid and boundary shape for the conduction solution at 1g. (i) Grid of 41 × 101 points. (ii) Refined grid of 81 × 181 points. Only the phase change region and its immediate vicinity is shown since the actual height of the rod is 40 times the radius. The zone heights agree to within 0.2% at the surface and 0.6% at the centerline.

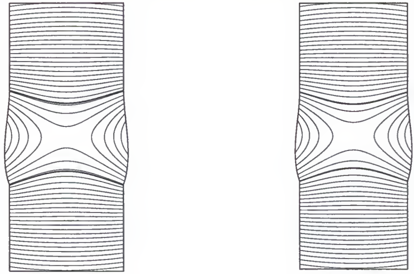

(i) $\Delta T = 4.53$ K, $T_{max} = 612.70$ K, $T_{min} = 298.00$ K, $P_L = 994.79$ dynes/cm^2

(ii) $\Delta T = 4.74$ K, $T_{max} = 612.59$ K, $T_{min} = 298.00$ K, $P_L = 988.37$ dynes/cm^2

Figure 5.11 Isotherms for the conduction solution at 1g. (i) Grid of 41 × 101 points and (ii) Refined grid of 81 × 181 points. The T_{max} agree to within 0.02%. The 41 × 101 grid solution differs with Lan (1994) by 0.6%.

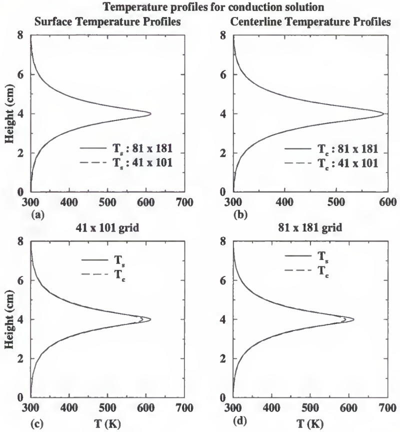

Figure 5.12 (a) and (b) Temperature profiles showing comparison between coarse grid of 41 × 101 points and fine grid of 81 × 181 points along the entire height of the domain. (a) Temperature profile along the surface. (b) Temperature profile along the centerline.
(c) and (d) Comparison of Temperatures along the surface and the centerline. (c) 41 × 101 grid, (d) 81 × 181 grid.

and (d) show that the temperature distribution in the feed and crystal regions becomes one–dimensional far away from the zone.

Figures 5.13 – 5.16 correspond to the microgravity condition. The most significant impact of microgravity on the conduction solution is on the meniscus shape. The meniscus shape now resembles a circular arc due to the absence of gravity and the solution displays symmetry about the heater location. Figure 5.13 establishes the convergence of the solutions on the 41 × 101 grid and the 81 × 181 grid. Figure 5.14 and 5.15 show the computed boundary shape, grid distribution and the isotherms. It is worth noting that the value of P_L

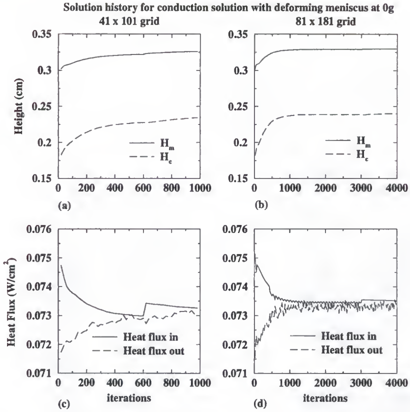

Figure 5.13 Convergence history for the conduction solution at 0g. (a) and (b) height of the zone at the surface and at the centerline for the grid of 41 × 101 points and 81 × 181 points respectively. (c) and (d) balance of the incoming and outgoing heat fluxes for the grid of 41 × 101 points and 81 × 181 points respectively.

required to maintain mass conservation in the molten zone decreases from the normal gravity case shown in Figure 5.11. Figure 5.16 compares the temperature profiles between the 41 × 101 and the 81 × 181 grids showing grid independence of the solution. It is also noted, from comparing Figures 5.9(c – d) and 5.13(c – d) that the microgravity situation causes a larger heat flux to be transported through the zone. This is due to the larger meniscus surface area in the vicinity of the heater.

5.6.1.2 Buoyancy Driven Convection

Figures 5.17 – 5.20 show the effect of buoyancy driven convection on the solution characteristics. Thermocapillary convection has been suppressed by imposing a zero shear

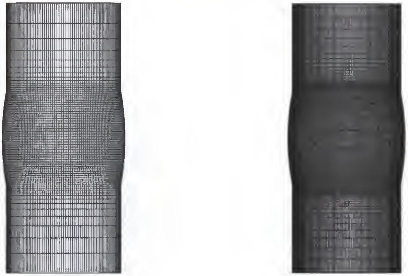

(i) $H_m = 0.327$ cm, $H_c = 0.234$ cm.

(ii) $H_m = 0.330$ cm, $H_c = 0.239$ cm.

Figure 5.14 Computed grid and boundary shape for the conduction solution at 0g. (i) Grid of 41 × 101 points. (ii) Refined grid of 81 × 181 points. Only the phase change region and its immediate vicinity is shown since the actual height of the rod is 40 times the radius. The zone heights agree to 1% at the surface and 2% at the centerline.

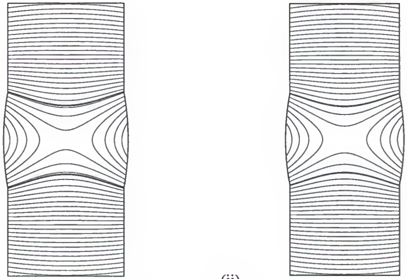

(i) $\Delta T = 4.50$ K, $T_{max} = 612.57$ K, $T_{min} = 298.00$ K, $P_L = 695.25$ dynes/cm^2

(ii) $\Delta T = 4.74$ K, $T_{max} = 613.25$ K, $T_{min} = 298.00$ K, $P_L = 704.61$ dynes/cm^2

Figure 5.15 Isotherms for the conduction solution at 0g. (i) Grid of 41 × 101 points and (ii) Refined grid of 81 × 181 points. The T_{max} agree to 0.1%.

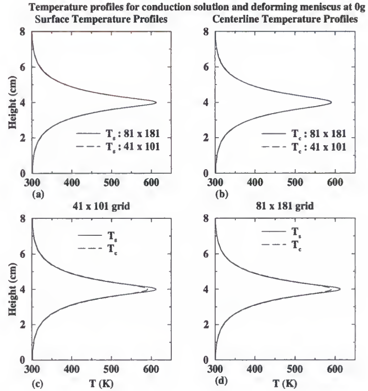

Figure 5.16 (a) and (b) Temperature profiles showing comparison between coarse grid of 41 × 101 points and fine grid of 81 × 181 points along the entire height of the domain. (a) Temperature profile along the surface. (b) Temperature profile along the centerline. (c) and (d) Comparison of Temperatures along the surface and the centerline. (c) 41 × 101 grid, (d) 81 × 181 grid.

stress condition on the free surface. Convergence was declared when the residuals were less than 10^{-5} for the momentum equations and 10^{-7} for the energy equation. The 1–norm of the solution was less than 10^{-5} for all the dependent variables. Figure 5.17 (a) and (b) show the convergence history of the zone lengths – H_m and H_c – on the 41 × 101 and 81 × 181 grids, respectively. Figure 5.17(c) and (d) show the history of the heat flux balance in the domain on the 41 × 101 and 81 × 181 grid systems, respectively. The heat flux balance on the 41 × 101 grid is satisfied to within 0.2% but on the 81 × 181 grid there is a 2% imbalance. However, this is adequate for the purpose of accuracy assessment and comparison with the solutions of Lan (1994). The streamfunction is shown in Figure 5.18. The maximum

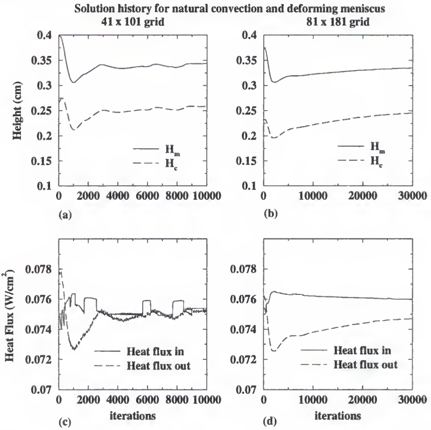

Figure 5.17 Convergence history for the natural convection solution. (a) and (b) height of the zone at the surface and at the centerline for the grid of 41 × 101 points and 81 × 181 points respectively. (c) and (d) balance of the incoming and outgoing heat fluxes for the grid of 41 × 101 points (0.2%) and 81 × 181 points (2%) respectively.

streamfunction, $\Psi_{\max}$, differs by less than 2%. The present solution on the 41 × 101 grid differs by 8% from the maximum streamfunction reported in Lan (1994). Figure 5.19 shows the corresponding isotherms. The maximum temperature, $T_{\max}$, occuring on the free surface differs by 0.05% between the solutions and 0.4% from the solution of Lan (1994). Figure 5.20 (a) and (b) show identical temperature profiles for the solutions on 41 × 101 and 81 × 181 grids indicating grid independence of the solution. Figures 5.20(c) and (d) may be contrasted with the conduction case illustrated in Figures 5.12(c) and (d) showing the decrease in $T_{\max}$ due to the effectiveness of convection in heat transport. The effect of natural

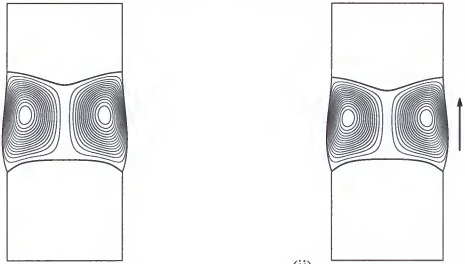

(i)
$\Psi_{max} = 2.706 \times 10^{-3}$ g/s,
$\Delta\Psi = 1.87 \times 10^{-4}$ g/s

(ii)
$\Psi_{max} = 2.654 \times 10^{-3}$ g/s
$\Delta\Psi = 1.84 \times 10^{-4}$ g/s

Figure 5.18. Streamfunction and phase interfaces on (i) 41 × 101 and (ii) 81 × 181 grids. (i) and (ii) differ by less than 2%. The arrow indicates the direction of the convection at the free surface. The 41 × 101 grid solution differs from Lan (1994) by 8%.

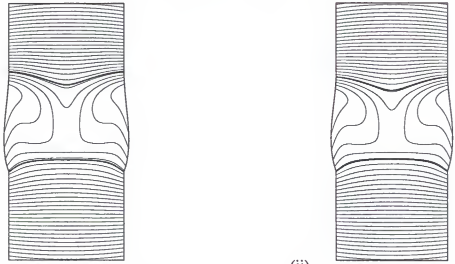

(i)
$\Delta T = 3.99$ K, $T_{max} = 601.03$ K,
$T_{min} = 301.23$ K
$H_m = 0.344$ cm, $H_c = 0.257$ cm
$P_L = 995.46$ dynes/cm^2

(ii)
$\Delta T = 4.07$ K, $T_{max} = 600.76$ K,
$T_{min} = 300.93$ K
$H_m = 0.335$ cm, $H_c = 0.244$ cm
$P_L = 995.31$ dynes/cm^2.

Figure 5.19 Isotherms on (i) 41 × 101 and (ii) 81 × 181 grids. T_{max} differs by 0.05%. The 41 × 101 grid solution differs from the solution of Lan (1994) by 0.4%.

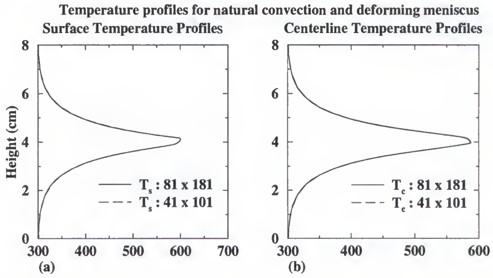

Figure 5.20 (a) and (b) Temperature profiles showing comparison between coarse grid of 41 × 101 points and fine grid of 81 × 181 points along the entire height of the domain. (a) Temperature profile along the surface. (b) Temperature profile along the centerline.

convection is to cause the heated melt to rise along the free surface, transfer heat to the melt–feed interface, and sink at the centerline towards the melt–crystal interface. This causes the melt–feed interface to acquire a more distorted shape compared with the conduction solution, and the melt–crystal interface to become flatter over most of the region except close to the meniscus. The distortion of the isotherms and the upward shift in the location of T_{max} is due to the convective action. Since the Prandtl number is high, even a modest Grashof number results in a significant impact on the temperature distribution. The higher temperature gradients evident at the base of the zone also indicate that the heating takes place close to the bottom of the zone. The zone is translated upward as compared with the conduction solution due to the enhancement of heat transfer through the upper half of the domain and its suppression throught the lower half.

5.7 Thermocapillary Convection

In the following set of calculations, the effect of thermocapillary convection is taken into account. As will be demonstrated, the Marangoni effect has a significant impact on the temperature distribution and the phase interfaces within the melt zone. The actual Marangoni numbers in this particular system are in the region of 5000, however, numerical stability constrained the calculations to a Marangoni number of 500. Grid independence and accuracy assessments have been carried out. Computations have been carried out to assess the impact of meniscus deformation on the solid – liquid interface shape and zone size. Calculations have also been conducted to simulate float zone growth under zero–gravity conditions to simulate float zone processing in orbit. In all subsequent calculations, the convergence criteria has been set to less than 10^{-4} for the momentum equations and to less than 10^{-6} for the energy equations while ensuring that the 1–norm of the solution was less than 10^{-5}. These criteria either meet or exceed the convergence criteria specified in the literature cited previously.

5.7.1 Normal Gravity

5.7.1.1 Cylindrical meniscus

A conduction calculation with the imposed cylindrical meniscus was used as the initial guess. Figure 5.21 shows the convergence history for calculations on the 41×101 grid as well as the 81×181 grid. Figure 5.21(a) and (b) show the history of the zone height and Figure 5.21(c) and (d) show the heat flux balance within the domain. Figure 5.22(a) shows the streamfunction and Figure 5.22(b) shows the computed isotherms. The streamfunction pattern shows the interaction between natural and thermocapillary convection. Two large convection rolls are apparent in the upper half of the domain where the thermocapillary convection aids natural convection. In the lower part of the zone, two small counter–rotating loops are formed where the thermocapillary effect opposes natural convection. The isotherm plots show that the location of T_{max} is displaced upwards and its value is less as compared with the conduction case. The distortion of the phase interfaces is clearly evident especially away from the centerline. Figure 5.23(a) and (b) provide a comparison of the temperature profiles on the two grid resolutions considered. The temperature distribution is almost identical on the two grids.

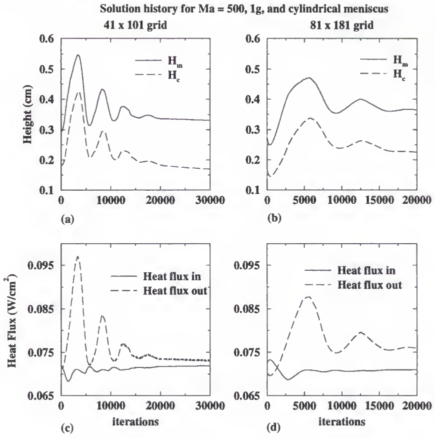

Figure 5.21 Convergence history for the thermocapillary convection solution Ma = 500, at 1g and with a fixed cylindrical meniscus. (a) and (b) height of the zone at the surface and at the centerline for the grid of 41 × 101 points and 81 × 181 points respectively. (c) and (d) balance of the incoming and outgoing heat fluxes for the grid of 41 × 101 points (1.7%) and 81 × 181 points (7%) respectively.

5.7.1.2 Deformed meniscus

The previous calculation is used as the starting guess and now the meniscus is allowed to deform according to the requirement of mass conservation and the Young–Laplace equation. Figure 5.24 shows the convergence history of the solution. Figure 5.24(a) and (b) show the convergence history of the zone height and an initially oscillatory convergence path can be observed which damps out as the iterations continue. Figure 5.24(c) and (d) show the heat flux balance for the solutions on the 41 × 101 grid and the 81 × 181 grid respectively. For the 41 × 101 grid, a heat flux imbalance of 4% is observed which reduces to 0.8% with

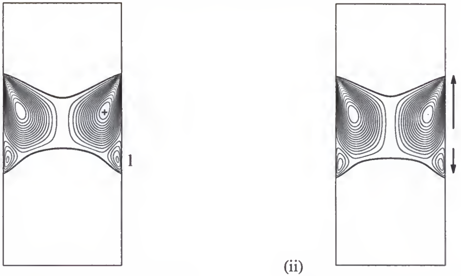

(i)
$\Psi_{max} = 1.733 \times 10^{-3}$ g/s, (+)
$\Delta\Psi = 1.20 \times 10^{-4}$ g/s
$\Psi_1 = -4.433 \times 10^{-4}$ g/s

(ii)
$\Psi_{max} = 2.242 \times 10^{-3}$ g/s
$\Delta\Psi = 1.55 \times 10^{-4}$ g/s
$\Psi_1 = -4.840 \times 10^{-4}$ g/s

(a) Streamfunction and phase interfaces on (i) 41 × 101 and (ii) 81 × 181 grids. Arrows show the direction of convection cells.

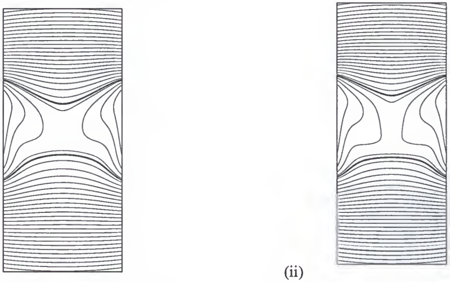

(i)
$\Delta T = 3.90$ K, $T_{max} = 596.97$ K,
$T_{min} = 300.85$ K
$H_m = 0.331$ cm, $H_c = 0.166$ cm

(ii)
$\Delta T = 4.04$ K, $T_{max} = 597.81$ K,
$T_{min} = 300.94$ K
$H_m = 0.365$ cm, $H_c = 0.223$ cm

(b) Isotherms on (i) 41 × 101 and (ii) 81 × 181 grids.

Figure 5.22 Solution for Ma = 500, 1g, and fixed cylindrical meniscus.

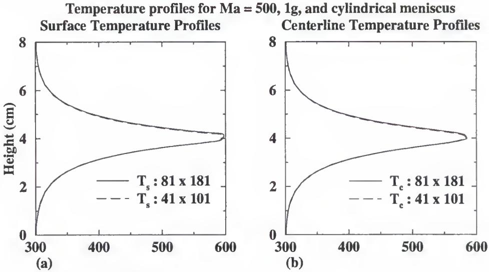

Figure 5.23 (a) and (b) Temperature profiles showing comparison between coarse grid of 41 × 101 points and fine grid of 81 × 181 points along the entire height of the domain. (a) Temperature profile along the surface. (b) Temperature profile along the centerline.

grid refinement. Figure 5.25(a) shows the streamfunction on the 41 × 101 grid and the 81 × 181 grid. Figure 5.25(b) shows the corresponding isotherms. Allowing the meniscus to deform increases the free surface area thereby increasing the convection strength of all the four convection cells in the domain. Since the maximum Temperature, T_{max}, is virtually unaffected, this implies a larger heat flux through the domain resulting in a taller melt zone. The increased strength of the upper convection rolls also causes the melt–crystal interface at the lower end of the melt zone to become flatter at the centerline, but acquire increased distortion close to the free surface. The maximum streamfunction differs by 9.7% between the solutions on the grid of 41 × 101 points and the grid of 81 × 181 points. Figure 5.26(a) and (b) compare the temperature profiles of the two solutions which are indistinguishable. Figure 5.26(c) and (d) show the upward displacement of the location of T_{max} as compared with the conduction solutions and the establishment of the one dimensional temperature distribution in the feed and crystal regions away from the melt zone.

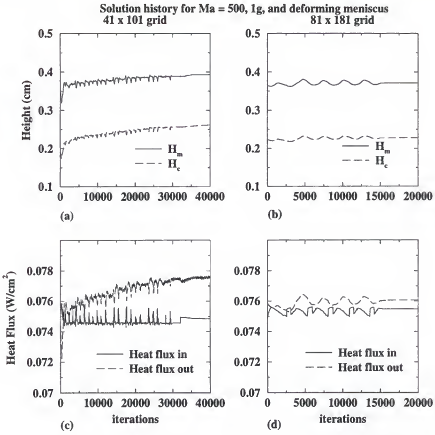

Figure 5.24 Convergence history for the thermocapillary convection solution Ma = 500, at 1g and with computed meniscus shape. (a) and (b) height of the zone at the surface and at the centerline for the grid of 41 × 101 points and 81 × 181 points respectively. (c) and (d) balance of the incoming and outgoing heat fluxes for the grid of 41 × 101 points (4%) and 81 × 181 points (0.8%) respectively.

5.7.1.3 Zero Gravity

5.7.1.4 Cylindrical meniscus

A conduction solution with an imposed cylindrical meniscus was used as the initial guess. Figure 5.27 shows the convergence history of the solution. Figure 5.27(a) and (b) show the history of the zone height for the solutions on the 41 × 101 grid and the 81 × 181 grid respectively. Figure 5.27(c) and (d) show the corresponding heat flux balance. Figure 5.28(a) shows the streamfunction and Figure 5.28(b) the isotherm distribution. It is immediately evident that the solution is symmetrical about y = 4 cm which is the heater

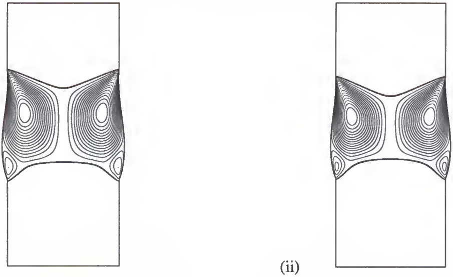

(i)
$\Psi_{max} = 2.880 \times 10^{-3}$ g/s,
$\Delta\Psi = 1.99 \times 10^{-4}$ g/s
$\Psi_1 = -4.975 \times 10^{-4}$ g/s

(ii)
$\Psi_{max} = 2.623 \times 10^{-3}$ g/s
$\Delta\Psi = 1.81 \times 10^{-4}$ g/s
$\Psi_1 = -5.160 \times 10^{-4}$ g/s

(a) Streamfunction and phase interfaces on (i) 41 × 101 and (ii) 81 × 181 grids.

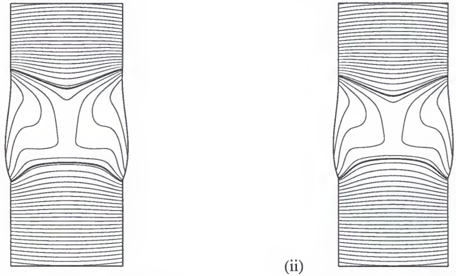

(i)
$\Delta T = 4.01$ K, $T_{max} = 598.66$ K,
$T_{min} = 301.33$ K
$H_m = 0.394$ cm, $H_c = 0.260$ cm.
$P_L = 1011.47$ dynes/cm^2.

(ii)
$\Delta T = 4.07$ K, $T_{max} = 597.87$ K,
$T_{min} = 300.94$K
$H_m = 0.372$ cm, $H_c = 0.227$ cm
$P_L = 1011.52$ dynes/cm^2.

(b) Isotherms on (i) 41 × 101 and (ii) 81 × 181 grids.

Figure 5.25 Solution for Ma = 500, 1g, and computed meniscus.

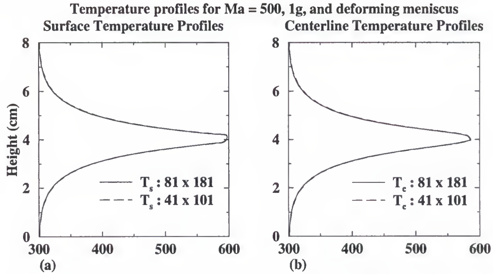

(a) (b)

Figure 5.26 (a) and (b) Temperature profiles showing comparison between coarse grid of 41 × 101 points and fine grid of 81 × 181 points along the entire height of the domain. (a) Temperature profile along the surface. (b) Temperature profile along the centerline.

location. Four counter–rotating flow loops are evident in the melt zone and these convection rolls cause the isotherm distribution to be pulled towards the free surface. Convection suppresses heat transfer to the centerline causing the characteristic convexity of the phase interfaces towards the melt. The maximum streamfunction is lower than that in the normal gravity case, but the flattening effect of natural convection on the melt–crystal interface is absent. Figure 5.29(a) and (b) compare the temperature profiles on the two grids and it may be observed that the two solutions are nearly identical.

5.7.1.5 Deformed meniscus

The previously computed solution was used as the initial guess and the meniscus was allowed to deform in response to the needs of global mass conservation and the Young–Laplace equation. For this case, momentum residuals of less than 5×10^{-4} could not be achieved on the grid of 41 × 101 points. Figure 5.30 shows the convegence history of the solution. Figure 5.31(a) shows the streamfunction and Figure 5.31(b) shows the isotherm distribution on the grid of 41 × 101 and 81 × 181 points. It is observed that the

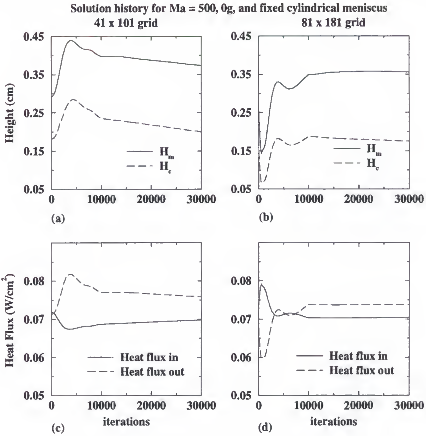

Figure 5.27. Convergence history for the thermocapillary convection solution Ma = 500, at 0g and with fixed cylindrical meniscus. (a) and (b) height of the zone at the surface and at the centerline for the grid of 41 × 101 points and 81 × 181 points respectively. (c) and (d) balance of the incoming and outgoing heat fluxes for the grid of 41 × 101 points (8.6%) and 81 × 181 points (4.6%) respectively.

convection rolls increase in strength since the meniscus deformation results in a larger surface area over which the surface tension gradients can act. These factors also result in a larger heat flux being transported through the domain and the height of the melt zone to increase. The maximum streamfunction differs by 6.6% between the solution on the 41 × 101 grid and 81 × 181 grid. Figure 5.32(a) and (b) show that the temperature profiles obtained on the two grids are identical.

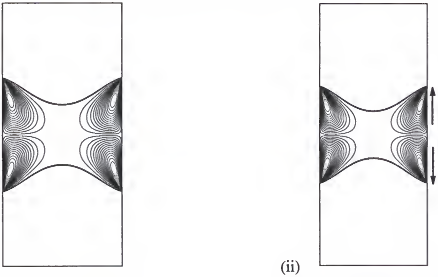

(i)
$\Psi_{max} = 1.013 \times 10^{-3}$ g/s,
$\Delta\Psi = 7.00 \times 10^{-5}$ g/s

(ii)
$\Psi_{max} = 0.954 \times 10^{-3}$ g/s
$\Delta\Psi = 6.58 \times 10^{-5}$ g/s

(a) Streamfunction and phase interfaces on (i) 41 × 101 and (ii) 81 × 181 grids. Arrows show the direction of convection on the free surface.

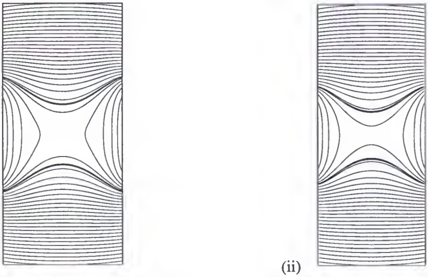

(i)
$\Delta T = 3.65$ K, $T_{max} = 600.18$ K,
$T_{min} = 298.00$ K
$H_m = 0.374$ cm, $H_c = 0.199$ cm

(ii)
$\Delta T = 4.14$ K, $T_{max} = 599.50$ K,
$T_{min} = 298.00$ K
$H_m = 0.356$ cm, $H_c = 0.173$ cm

(b) Isotherms on (i) 41 × 101 and (ii) 81 × 181 grids.

Figure 5.28 Solution for Ma = 500, 0g, and fixed cylindrical meniscus.

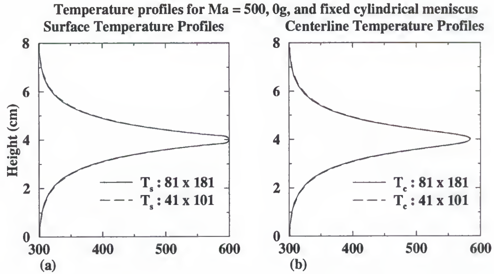

Figure 5.29 (a) and (b) Temperature profiles showing comparison between coarse grid of 41 × 101 points and fine grid of 81 × 181 points along the entire height of the domain. (a) Temperature profile along the surface. (b) Temperature profile along the centerline.

5.8 Conclusion

A moving boundary technique has been developed in the context of the SIMPLE algorithm and the enthalpy method for the computation of convective heat transfer and solidification in the float zone. A general multi–block technique for algebraic grid generation has been developed to fit curved free surfaces and adaptively enclose the phase change regions in solidification processes. Underrelaxation procedures have been developed to ensure the stability of the numerical procedure. Care has been taken to ensure that grid quality is maintained after the grid generation procedure with appropriate error recovery in case of failure of the grid generation procedure.

Computations have been carried out to assess the robustness, stability and accuracy of the convective heat transfer and phase change computations via grid refinement and comparison with the solutions of Lan (1994). The solutions of Lan (1994) were based on front tracking rather than the enthalpy method, used the streamfunction–vorticity

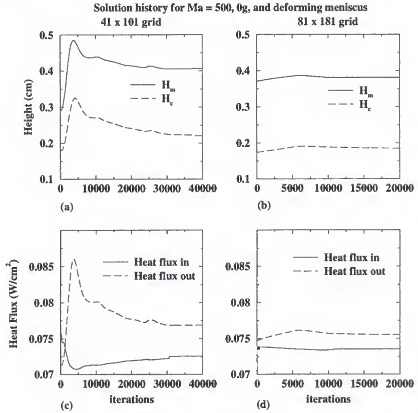

Figure 5.30 Convergence history for the thermocapillary convection solution Ma = 500, at 0g and with computed meniscus shape. (a) and (b) height of the zone at the surface and at the centerline for the grid of 41 × 101 points and 81 × 181 points respectively. (c) and (d) balance of the incoming and outgoing heat fluxes for the grid of 41 × 101 points (6%) and 81 × 181 points (2.7%) respectively.

formulation of the Navier–Stokes equations as opposed to the primitive variables formulation used in the present work, and employed first order upwind schemes for the convection schemes rather than the second order central difference scheme employed in this study. It is found that for the conduction–capillarity and buoyancy driven convection calculations, grid independent solutions can be obtained even on 41 × 101 grids. However, when thermocapillary convection is taken into account, grid refinement from the 41 × 101 grid to the 81 × 181 grid exhibits quantitative differences although not qualitative differences. Good comparison has been obtained with the solutions of Lan (1994) for the

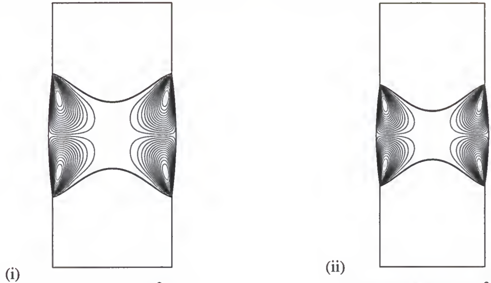

$\Psi_{max} = 1.170 \times 10^{-3}$ g/s,
$\Delta\Psi = 8.07 \times 10^{-5}$ g/s

$\Psi_{max} = 1.097 \times 10^{-3}$ g/s
$\Delta\Psi = 7.57 \times 10^{-5}$ g/s

(a) Streamfunction and phase interfaces on (i) 41 × 101 and (ii) 81 × 181 grids.

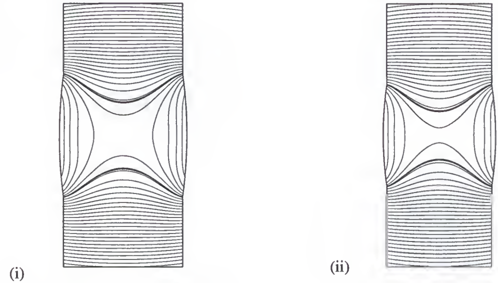

$\Delta T = 3.63$ K, $T_{max} = 600.89$ K,
$T_{min} = 298.00$ K
$H_m = 0.406$ cm, $H_c = 0.219$ cm
$P_L = 642.25$ dynes/cm^2

$\Delta T = 4.23$ K, $T_{max} = 599.95$ K,
$T_{min} = 300.91$K
$H_m = 0.381$ cm, $H_c = 0.183$ cm
$P_L = 654.94$ dynes/cm^2.

(b) Isotherms on (i) 41 × 101 and (ii) 81 × 181 grids.

Figure 5.31 Solution for Ma = 500, 0g, and computed meniscus.

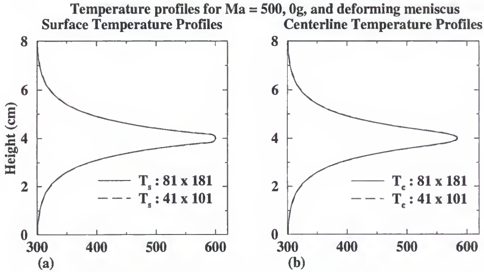

Figure 5.32 (a) and (b) Temperature profiles showing comparison between coarse grid of 41 × 101 points and fine grid of 81 × 181 points along the entire height of the domain. (a) Temperature profile along the surface. (b) Temperature profile along the centerline.

conduction–capillarity and natural convection solutions with similar boundary shapes and grid distributions.

Computations have been carried out to assess the impact of free surface deformation as well as microgravity environment on the float zone. The free surface deformation results in a larger surface area at the meniscus resulting in a higher strength of thermocapillary convection as well as an increase in the heat flux through the system. Thus, for the parameters and regimes considered in this study, the free surface deformation has a quantitative but not qualitative impact on the melt zone. The microgravity environment, on the other hand, results in a suppression of buoyancy induced convection as well as a significant impact on the meniscus shape. However, at the operating parameters considered in this study, the microgravity environment does not offer any significantly reduced convection since the surface tension gradient is always present due to the thermal inhomogeneties along the meniscus.

The difference between the present study and the previous studies lies in the use of the enthalpy method as opposed to interface tracking and the use of a flexible, multi–block grid generation procedure that, in conjunction with the use of the enthalpy method, can adapt to a wide range of zone lengths including the fully solid case. The procedure has been designed to accommodate unsteady computations, to be presented in a subsequent study, which can use a fully solid rod as the initial condition. A front tracking procedure as employed by Lan (1994) or Lan and Kou (1991) cannot handle the small zone sizes that will be present initially. The use of the enthalpy method in this study makes it unnecessary to fit the solid–liquid interfaces giving additional flexibility. This study also uses higher order convection schemes – the second order central difference scheme as opposed to the first order upwind scheme used in the previous studies. Also, grid refinement studies have been carried out employing substantially higher grid resolutions than the previous studies. The study indicates that higher grid resolutions, such as those considered in this study, are needed as the strength of thermocapillary convection increases in the present float zone system.

CHAPTER 6
CONCLUSION

6.1 Summary and Conclusions

A computational tool has been developed to simulate fluid flow, heat transfer, moving free surfaces, and phase change dynamics in the context of problems involving solidification and single crystal growth.

(1) The SIMPLE algorithm in body fitted coordinates has been used as a starting point for algorithm development.

(2) A previously developed free energy minimization model has been used to compute meniscus shapes based on the static Young–Laplace equation for problem of float zone growth of NiAl. The free energy criterion has been verified with available experimental data and good agreement obtained. The free energy criterion has then been used to generate meniscus shapes for the float zone problem. When dynamical effects of melt convection are taken into account, it is found that the Capillary numbers are very small compared to the Bond number and the viscous normal stress is too small to have any significant impact on the meniscus shape thus justifying the static meniscus shape used in the solidification calculations.

(3) A moving boundary computational procedure has been formulated in order to couple the free surface computation with the solid/liquid interface dynamics and melt convection. An algebraic grid generation procedure using transfinite interpolation has been used to regenerate the grid at every iteration following the update of the meniscus shape from the normal stress balance implied by the dynamic Young–Laplace equation.

(4) A variety of accurate convection schemes, the second order central difference scheme, the second order upwind scheme, and a 'mixed' formulation consisting of the second order upwind scheme for the momentum equations and the lower order hybrid scheme for the energy equation have been tested against the benchmark problem of natural convection of air in a square cavity. It has been found that the 'mixed' formulation suffered no degradation of accuracy in spite of the formal lower order of accuracy even for high Rayleigh numbers.

(5) Time dependent simulations, using the second order central difference scheme for the convection terms and the first order backward Euler method for the transient terms, have been conducted for the problem of transient natural convection around an enclosed vertical channel, with application to electronics cooling. Care has been taken to maintain good accuracy in space and time by means of grid and time step refinement.

(6) Steady, thermocapillary convection in an idealized model for float zone growth of NiAl single crystals has been simulated. In the simplified model, the liquid bridge has been considered to be suspended between two fixed flat plates and the meniscus shape satisfies the static Young–Laplace equation. Consequently, the meniscus shape is imposed in this static model and is not computed as part of the solution. It is found that the isotherm distribution for high Marangoni number convection differs considerably from the heat conduction solution obtained by neglecting convective effects altogether. It is also determined that thermocapillary convection dominates over natural convection even at 1–g conditions.

(7) A single region enthalpy formulation has been developed for the numerical computation of phase change processes on a fixed grid. Two alternative implementations of the enthalpy method have been developed – the T–based method and the H–based method. The one dimensional Stefan problem has been used to test the accuracy and efficiency of the two methods. It has been found that while both

methods are equally accurate, the T–based method is faster and computationally efficient over a range of Stefan numbers and mushy zone thickness. The H–based method is more robust over a wide range of parameters and works even when the size of the mushy zone shrinks to zero.

(8) The enthalpy porosity model has also been tested on a two dimensional melting problem where the heat transfer is dominated by natural convection in the melt. Qualitative agreement has been obtained with available experimental data.

(9) The simplified float zone model developed for single crystal growth of NiAl has been improved by relaxing the restriction of flat solid/liquid interfaces and employing a moving grid procedure to track the deforming free surface of the float zone. The enthalpy porosity method has been used to couple the phase change computations with thermocapillary and natural convection. Computations have been carried out to assess the interaction between thermocapillary convection and buoyancy induced convection and the impact of free surface deformation by considering normal gravity as well as microgravity conditions.

6.2 Future Work

6.2.1 Node Jumping

The enthalpy method is prone to the node jumping problem even for the unsteady one dimensional conduction problem as is observed in Fig. 4.5 – 4.7. Different researchers have attempted to deal with this problem by diagnosing that the node jumping is due to the nodal temperature of the phase change control volume being held constant at T_m even when the interface has moved away from the nodal point. Voller and Cross (1981) iteratively adjust the time step so that the interface is always located at the nodal points. Date (1992) has attempted to correct the nodal temperatures by estimating the location of the interface in a one dimensional context to obtain a smooth motion of the interface. However, such corrections are not straightforward to obtain in a multidimensional problem and can be implemented in many different ways. In the current study of the enthalpy method shown in

Fig. 4.5 – 4.7 it is observed that the node jumping problem decreases as the thickness of the mushy zone increases; nevertheless, it is worthwhile to cure the node jumping problem in a multidimensional context to obtain better time accuracy.

6.2.2 Multi–Block Approach

A multi–block approach (Wright and Shyy 1992, Shyy et. al. 1994) to the float zone problem would result in better accuracy and computational economy. For instance, the single region formulation implies that all the field equations are solved in both the phases which is wasteful of computer time and storage. In a multi–block approach, only the heat conduction equation needs to be solved in the crystal and the feed regions; also, fewer grid points in the radial direction can be used in these regions since the temperature profiles vary slowly and are predominantly one dimensional in these regions. This, coupled with grid adaptation towards the mushy zone and regions of high velocity gradients (Shyy 1987), will allow more grid points to be located in the phase change and moving boundary region, resulting better accuracy and economy.

6.2.3 Feed/Crystal Rotation

Some researchers (Lan and Kou 1991c, 1992b, 1993b, Mühlbauer et. al. 1995) have determined that rotation/counterrotation of the feed and/or the crystal can result improved heat transfer to the centerline of an otherwise axisymmetric melt due to the swirl induced in the melt resulting in shorter zones and enabling larger diameter crystals to be grown.

6.2.4 Dopant Transport

Dopant transport and concentration play an important role in determining the solid/liquid interface shape and stability. Inclusion of solute transport and segregation models will make it more complete and useful.

6.2.5 Electromagnetic Heating

A more complete model of the float zone process can be constructed by including electromagnetic effects. For electrically conducting materials, induction heating is a common means of heating the zone. Associated electromagnetic levitation forces also help to stabilize the meniscus against gravity enabling bigger zone sizes under 1–g conditions.

REFERENCES

Atthey, D.R. 1975, "A Finite Difference Scheme for Melting Problems based on the Method of Weak Solutions." in Moving Boundary Problems in Heat Flow and Diffusion, J.R.Ockendon and W.R.Hodgekins (eds), Clarendon Press, 182 – 191.

Aung, W. 1972, "Fully Developed Laminar Free Convection between Vertical Plates Heated Asymmetrically," Intl. J. Heat Mass Transfer, vol. 15, 1577 – 1580.

Aung, W., Fletcher, L.S. and Sernas, V. 1972, "Developing Laminar Free Convection between Vertical Plates and Asymmetric Heating," Intl. J. Heat Mass Transfer, vol. 16, 2293 –2308.

Bennon, W.D. and Incropera, F. P. 1987 "A Continuum Method for Momentum, Heat and Species Transport in Binary Solid–Liquid Phase Change Systems–I." Model Formulation," Int. J. Heat Mass Transf., vol. 30, 2161–2170.

Bodoia, J.R. and Osterle, J.F. 1962, "The Development of Free Convection between Heated Vertical Plates," J. Heat Transfer, vol. 84, 40 – 43.

Braaten, M.E. and Shyy, W. 1986 "A Study of Recirculating Flow Computation using Body–Fitted Coordinates: Consistency Aspects and Mesh Skewness," Numer. Heat Transf. vol. 9, 559–574.

Brown, R. A. 1988 "Theory of Transport Processes in Single Crystal Growth from the Melt," AIChE J., vol. 34, 881 – 911.

Carpenter, B.M. and Homsy, G.M. 1989 "Combined Buoyant–Thermocapillary Flow in a Cavity," J. Fluid Mech., vol. 207, 121–132.

Carpenter, B.M. and Homsy, G.M. 1990 "High Marangoni Number Convection in a Square Cavity: Part II," Phys. Fluids A, vol. 2, 137–149.

Chan, Y. T. 1995 "Crystal Growth," in Computational Modeling in Semiconductor Processing, M. Meyyappan (editor), Artech House, Boston.

Chan, Y. T. and Choi, S. K. 1992 "Numerical Simulations of Inductive–Heated Float–Zone Growth," J. Appl. Phys., vol. 72, 3741 – 3749.

Chandra, U. 1990 "Benchmark Problems and Testing of a Finite Element Code for Solidification in Investment Castings." Int. J. Numer. Methods Engrg. Vol. 30, 1301 – 1320.

Chang, T. S. and Lin, T. F. 1989, "Transient Buoyancy–Induced Flow Through a Heated, Vertical Channel of Finite Height," Numer. Heat Transfer, vol. 16A, 15 – 35.

Chen, H., Saghir, M. Z., Quon, D. H. H. and Chehab, S. 1994 "Numerical Study on Transient Convection in Float Zone Induced by g–jitters," J. Crystal Growth, vol. 142, 362 – 372.

Chu, C.–F. and Chen, J.–C. 1995 "Numerical Computation of Fluid Flow of Floating-Zone Crystal Growth of Molybdenum," Intl. J. Heat Mass Transf., vol. 38, 1841 – 1853.

Concus, P. 1990 "Capillary Surfaces in Microgravity," in Low–Gravity Fluid Dynamics and Transport Phenomena, J. N. Koster and R. L. Sani (ed.) vol. 130, Progress in Astronautics and Aeronautics, AIAA, Washington D.C., 183–206.

Coriell, S.R., Hardy, S.C. and Cordes, M.R. 1977 "Stability of Liquid Zones," J. Colloid. Interface. Sci., vol. 60, 126–136.

Crank, J. 1984 Free and Moving Boundary Problems, Oxford University Press. Oxford, UK.

Davis, 1990 "Hydrodynamic Interactions in Directional Solidification," J. Fluid Mech., vol. 212, 241 – 262.

Darolia, R., 1991 "NiAl Alloys for High–Temperature Structural Applications," JOM, March Issue, 44–49.

Date, A. W. 1992 "Novel Strongly Implicit Enthalpy Formulation for Multidimensional Stefan Problems," Numer. Heat Transf., vol. 21B, 231 – 251.

de Vahl Davis, G. 1983, "Natural Convection of Air in a Square Cavity: a benchmark numerical solution," Intl. J. numer. meth. fluids., vol. 3, 249 – 264.

Duranceau, J. L. and Brown, R. A. 1986 "Thermal-Capillary Analysis of Small-Scale Floating Zones," J. Crystal Growth, vol. 75, 367 – 389.

Dreeben, A.B., Kim, K.M. and Schulko, A. 1980 "Measurement of Meniscus Angle in Laser Heated Float Zone Growth of Constant Diameter Sapphire Crystals," J. Crystal Growth, vol. 50, 126–132.

Elenbaas, W. 1942 "Heat Dissipation of Parallel Plates by Free Convection," Physica, Amsterdam, vol. ix, 1 – 28.

Finn, R. (1986) Equilibrium Capillary Surfaces, Springer–Verlag, New York.

Gau, C. and Viskanta, R. 1986 "Melting and Solidification of a Pure Metal on a Vertical Wall," ASME J. Heat Transfer, vol. 108, 174 – 181.

Gebhart, B., Jaluria, Y., Mahajan, R.L. and Sammakia, B. 1988, Buoyancy Induced Flows and Transport, Hemisphere.

Gingrich, W.K., Cho, Y.I. and Shyy, W. 1992 "Effect of Shear Thinning on Laminar Heat Transfer Behavior in a Rectangular Duct," Intl. J. Heat Mass Transf., vol. 35, 2823–2836.

Glicksman, M.E., Coriell, S. R. and McFadden, G. B. 1986 "Interaction of Flows with the Crystal-Melt Interface," Ann. Rev. Fluid Mech., vol. 18, 307–336.

Grugel, R. N., Shen, X. F., Anilkumar, A. V. and Wang, T. G. 1994 "The Influence of Vibration on Microstructural Uniformity during Floating–Zone Crystal Growth," J. Crystal Growth, vol. 142, 209 – 214.

Hortmann, M., Peric, M. and Scheurer, G. 1990, "Finite Volume Multigrid Prediction of Laminar Natural Convection: Benchmark Solutions," Intl J. Numer. Methods Fluids., vol. 11, 189 – 207.

Hou, T.Y., Lowengrub, J.S. and Shelley, M.J. 1994 "Removing the Stiffness from Interfacial Flows with Surface Tension," J. Comp. Phys., vol. 114, 312–338.

Hu, W. R., Shu, J. Z., Zhou, R. and Tang, Z. M. 1994 "Influence of Liquid Bridge Volume on the Onset of Oscillation in Floating Zone Convection. I. Experiments," J. Crystal Growth, vol. 142, 379 – 384.

Huh, C. and Mason, S.G. 1977 "Effects of Surface Roughness on Wetting," J. Colloid. Interface. Sci., vol. 60, 11–38.

Huppert, 1990 "The Fluid Mechanics of Solidification," J. Fluid Mech. vol. 212, 209 – 240.

Hurle, D. T. J. 1993, Crystal Pulling from the Melt, Springer–Verlag, Berlin.

Kanouff, M. and Greif, R. 1994 "Oscillations in Thermocapillary Convection in a Square Cavity," Int. J. Heat Mass Transf., vol. 37, 885–892.

Keene, B.J. 1993 "Review of Data for the Surface Tension of Pure Metals," Int. Metals Reviews, vol. 38, 157–192.

Kettleborough, C.F. 1972 "Transient Laminar Free Convection between Heated Vertical Plates including Entrance Effects," Intl J. Heat Mass Transfer, vol. 15, 883 – 896.

Kimura, S. and Bejan, A. 1983 "The 'Heatline' Visualization of Convective Heat Transfer," J. Heat Transf., vol. 105, 916 – 919.

Kobayashi, N. 1984 "Computer Simulation of the Steady Flow in a Cylindrical Floating Zone under Low Gravity," J. Crystal Growth, vol. 66, 63–72.

Kobayashi, N. 1988 "Steady Convection Caused by the Temperature Inhomogeneity in a Cylindrical Floating Zone," Japanese. J. Appl. Phys., vol. 27, 20–24.

Koschmieder, E.L. 1993 Benard Cells and Taylor Vortices, Cambridge University Press, Cambridge, U.K.

Lacroix, M. 1989 "Computation of Heat Transfer during Melting of a Pure Substance from an Isothermal Wall," Numer. Heat Transfer, Part B, vol. 15, 391 – 210.

Lacroix, M. and Voller, V. R. 1990 "Finite Difference Solutions of Solidification Phase Change Problems: Transformed versus Fixed Grids," Numer. Heat Transf., vol. 17B, 25–41.

Lan, C. W. 1994 "Newton's Method for Solving Heat Transfer, Fluid Flow and Interface Shapes in a Floating Molten Zone," Intl. J. Numer. methods Fluids, vol. 19, 41 – 65.

Lan, C. W. and Kou, S. 1990a "Thermocapillary Flow and Melt/Solid Interfaces in Floating-Zone Crystal Growth under Microgravity," J. Crystal Growth, vol. 102, 1043 – 1058.

Lan, C. W. and Kou, S. 1990b "Heat transfer, Fluid Flow and Interface Shapes in Floating-Zone Crystal Growth under Microgravity," J. Crystal Growth, vol. 108, 351 – 366.

Lan, C. W. and Kou, S. 1991a "Floating-Zone Crystal Growth with a Heated Ring Covering the Melt Surface," J. Crystal Growth, vol. 108, 1 – 7.

Lan, C. W. and Kou, S. 1991b "Floating-Zone Crystal Growth with a Heated and Immersed Shaper – Computer Simulation," J. Crystal Growth, vol 108, 340 – 350.

Lan, C. W. and Kou, S. 1991c "Effects of Rotation on Heat Transfer, Fluid Flow and Interfaces in Normal Gravity Floating-Zone Crystal Growth," J. Crystal Growth, vol. 114, 517 – 535.

Lan, C. W. and Kou, S. 1992a "Heat Transfer and Fluid Flow in Floating-Zone Crystal Growth with a Mostly Covered Melt Surface," Intl. J. Heat Mass Transf., vol. 35, 433 – 442.

Lan, C. W. and Kou, S. 1992b "Shortened Floating Zone Crystal Growth under Normal Gravity," J. Crystal Growth, vol. 119, 281 – 291.

Lan, C. W. and Kou, S. 1993a "Radial Dopant Segregation in Zero-Gravity Floating-Zone Crystal Growth," J. Crystal Growth, vol. 132, 578 – 591.

Lan, C. W. and Kou, S. 1993b "Effect of Rotation on Radial Dopant Segregation in Microgravity Floating-Zone Crystal Growth," J. Crystal Growth, vol. 133, 309 – 321.

Langbein, D. 1992 "Oscillations of Finite Liquid Columns," Microgravity. Sci. Technol., V/2, 73–85.

Langlois, 1985 "Buoyancy Driven Flows in Crystal Growth Melts," Ann. Rev. Fluid Mech., vol. 17, 191 – 215.

Lee, J., Lee, D.–J. and Lee, J. H. 1995 "On the Mechanism of Oscillation in a Simulated Floating Zone," J. Crystal Growth, vol. 152, 341 – 346.

Levenstam, M., Amberg, G., Carlberg, T. and Andersson, M. 1996 "Experimental and Numerical Studies of Thermocapillary Convection in a Floating Zone like Configuration," J. Crystal Growth, vol. 158, 224 – 230.

Li, J. and Saghir, M. Z. 1994 "Coupled Buoyant and Surface Tension Driven Convection in Liquid Encapsulation Floating Zone under 1–g and 0–g with Defromable Interfaces," AIAA Paper No. AIAA–94–0793.

Li, J., Sun, J., and Saghir, Z. 1993 "Buoyant and Thermocapillary Flow in Liquid Encapsulated Floating Zone," J. Crystal Growth, vol. 131, 83–96.

Lie, K.H., Riahi, D.N. and Walker, J.S. 1989 "Buoyancy and Surface Tension Driven Flows in Float Zone Crystal Growth with a Strong Axial Magnetic Field," Int. J. Heat Mass. Transfer, vol. 32, 2409–2420.

Martin, L., Raithby, G.D. and Yovanovich, M.M. 1991 "On the Low Rayleigh Number Asymptote for Natural Convection Through an Isothermal Parallel – Plate Channel," J. Heat Transfer, vol. 113, 899 – 905.

McNeil, T.J., Cole, R. and Subramanian, R.S. 1985 "Surface Tension Driven Flow in a Glass Melt," J. Am. Cer. Soc., vol. 68, 254–259.

Monti, R. 1990 "Gravity Jitters: Effects on Typical Fluid Science Experiments" in Low Gravity Fluid Dynamics and Transport Phenomena, J.N. Koster and R.L. Sani (eds), Progress in Astronautics and Aeronautics, vol. 130, AIAA, Washington, D. C.

Mühlbauer, A., Muiznieks, A., Virbulis, J., Lüdge, A., and Riemann, H. 1995 "Interface Shape, Heat Transfer and Fluid Flow in the Floating Zone Growth of Large Silicon Crystals with the Needle–eye Technique," J. Crystal Growth, vol. 151, 66 – 79.

Mullins, W. W. and Sekerka, R. F. 1964 "Stability of a Planar Interface during Solidification of a Dilute Binary Alloy," J. Appl. Phys., vol. 3, 444–451.

Mundrane, M. and Zebib, A. 1994 "Oscillatory Buoyant Thermocapillary Flow," Phys. Fluids, vol. 6, 3294–3305.

Murthy, J.Y. 1987 "A Numerical Simulation of Flow, Heat and Mass Transfer in a Floating Zone at High Rotational Reynolds Numbers," J. Crystal Growth, vol. 83, 23–34.

Myshkis, A.D., Babskii, V.G., Kopachevskii, N.D., Slobozhanin, L.A. and Tyuptsov, A.D. (1987) Low Gravity Fluid Mechanics, translated by R.S. Wadhwa, Springer–Verlag, New York.

Nakamura, H., Asako, Y. and Naitou, T. 1982, "Heat Transfer by Free Convection Between Two Parallel Plates," Numer. Heat Transfer, vol. 5, 95 – 106.

Naylor, D., Floryan, J.M. and Tarasuk, J.D. 1991 "A Numerical Study of Developing Free Convection between Isothermal Vertical Plates," J. Heat Transfer, vol. 113, 620 – 626.

Neitzel, G.P., Hyer, J.R. and Jankowski, D.F. 1990 "Thermocapillary Convection in a Model Float Zone," AIAA Paper No. AIAA–90–0406.

Patankar, S.V. 1980, Numerical Heat Transfer and Fluid Flow, Hemisphere.

Poirier, D. and Saleudean, M. 1988 "On Numerical Methods used in Mathematical Modelling of Phase Change in Liquid Metals," ASME J. Heat Transfer, vol. 110, 562 – 590.

Prakash, C. 1990 "Two–Phase Model for Binary Solid-Liquid Phase Change, Part I: Governing Equations," Numer. Heat Transf., vol. 18B, 131–145.

Prakash, C. and Voller, V.R. 1989 "On the Numerical Solutions of Continuum Mixture Model Equations Describing Binary Solid–Liquid Phase Change.", Numer. Heat Transfer, part B, vol. 15, 171 – 189.

Prakash, C., Samonds, M. and Singhal, A.K. 1987 "A Fixed Grid Numerical Modeling Methodology for Phase Change Problems Involving a Moving Heat Source.", Int. J. Heat Mass Transfer, vol. 30, 2690 – 2694.

Quon, D.H.H., Chehab, S., Aota, J., Kurikose, A.K., Wang, S.S.B., Saghir, M.Z., and Chen, H.L. 1993 "Float–zone Crystal Growth of Bismuth Germanate and Numerical Simulation," J. Crystal Growth, vol. 134, 266 – 274.

Raithby, G.D. and Hollands, K.G.T. 1985 "Natural Convection" in Handbook of Heat Transfer, (eds) W.M. Rohsenow, J.P. Hartnett, E.N. Ganic, 6.1 – 6.93, McGraw–Hill, New York.

Ramanathan, S and Kumar, R. 1991 "Correlations for Natural Convection between Heated Vertical Plates," J. Heat Transfer, vol. 113, 97 – 107.

Riahi, D.N. and Walker, J.S. 1989 "Float Zone Shape and Stability with the Electromagnetic Body Force due to a Radio–Frequency Induction Coil," J. Crystal Growth, vol. 94, 635–642.

Sen, S. and Stefanescu, D. M., 1991 "Melting and Casting Processes for High–Temperature Intermetallics," JOM, May Issue, 30–32.

Shyy, W. 1987 An Adaptive Grid Method for Navier-Stokes Flow Computation, Appl. Math. Comp., vol. 21, 201–219.

Shyy, W. 1994 Computational Modeling for Fluid Flow and Interfacial Transport, Elsevier, Amsterdam, The Netherlands.

Shyy, W. and Chen, M.–H. 1991 "Interaction of Thermocapillary and Natural Convection Flows during Solidification: Normal and Reduced Gravity Conditions.", J. Crystal Growth, vol. 108, 247 – 261.

Shyy, W. and Chen, M.–H. 1993 "A Study of Buoyancy Induced and Thermocapillary Flow of Molten Alloy," Comput. Meths. Appl. Mech. Engrg., vol. 105, 333–358.

Shyy, W, Gingrich, W.K. and Gebhart, B. 1992 "Adaptive Grid Solution for Buoyancy Induced Flow in Vertical Slots," Numer. Heat Transf., vol. 22A, 51–70.

Shyy, W., Liu, J. and Wright, J. 1994 "Pressure–Based Viscous Flow Computation using Multiblock Curvilinear Grids," Numer. Heat Transf., vol. 25, 39 – 59.

Shyy, W., Thakur, S. and Wright, J. 1992 "Second Order and Central Difference Schemes for Recirculating Flow Computation," AIAA J., vol. 30, 923 – 932.

Shyy, W., Tong, S.S. and Correa, S.M. 1985 "Numerical Recirculating Flow Calculation Using a Body–Fitted Coordinate System," Numer. Heat Transf., vol. 8, 99–113.

Shyy, W., Udaykumar, H.S. and Liang, S.–J. 1992 "An Interface Tracking Method Applied to Morphological Evolution during Phase Change." Intl. J. Heat Mass Transfer., vol. 36, 2610 – 2623.

Shyy, W., Udaykumar, H.S. and Liang, S.–J. 1993 "Quasiequilibrium Meniscus Formation with Hysterisis Effects," Phys. Fluids A, vol. 5, 2610–2623.

Shyy, W., Udaykumar, H. S., Rao, M. M. and Smith, R. W. 1995 Computational Fluid Dynamics with Moving Boundaries, Taylor and Francis, Washington, D. C.

Shyy, W. and Vu, T.C. 1991 "On the Adoption of Velocity Variable and Grid System for Fluid Flow Computation in Curvilinear Coordinates," J. Comput. Phys., vol. 92, 82–105.

Sparrow, E.M. and Gregg, J.L. 1956 "Laminar Free Flow Convection from a Vertical Plate with Uniform Surface Heat Flux," ASME Transaction C, vol. 78, 435 – 440.

Sparrow, E.M. and Bahrami, P.A. 1980 "Experiments on Natural Convection from Heated Vertical Parallel Plates with Either Open or Closed Edges," J. Heat Transfer, vol. 102, 221 – 227.

Sparrow, E.M., Chrysler, G.M. and Azevedo, L.F. 1984 "Observed Flow Reversals and Measured – Predicted Nusselt Numbers for Natural Convection in a One – Sided Heated Vertical Channel," J. Heat Transfer, vol. 106, 325 – 332.

Sparrow, E.M. and Azevedo, L.F. 1985 "Vertical – Channel Natural Convection Spanning between the Fully Developed Limit and the Single – Plate Boundary – Layer – Limit," Intl. J. Heat Mass Transfer, vol. 28, 1847 – 1857.

Tang, Z. M. and Hu, W. R. 1994 "Influence of Liquid Bridge Volume on the Onset of Oscillation in Floating Zone Convection. II. Numerical Simulation," J. Crystal Growth, vol. 142, 385 – 391.

Tao, Y., Sakidja, R. and Kou, S. 1995 "Computer Simulation and Flow Visualization of Thermocapillary Flow in a Silicone Oil Floating Zone," Int. J. Heat Mass Transf., vol. 38, 503–510.

Tsamopoulos, J.A., Poslinski, A.J. and Ryan, M.E. 1988 "Equilibrium Shapes and Stability of Captive Annular Menisci," J. Fluid Mech., vol. 197, 523–549.

Tsamopoulos, J.A., Chen, T.–Y. and Borkar, A. 1992 ‘"Viscous Oscillations of Capillary Bridges," J. Fluid Mech., vol. 235, 579–609.

Vanka, S. P. 1987 "Second Order Upwind Differencing in a Recirculating Flow," AIAA J., vol. 25, 1435 – 1441.

Viskanta, R. 1990 "Mathematical Modeling of Transport Processes during Solidification of Binary Systems," JSME Intl. J., series II, vol. 33, 409 – 423.

Voller, V.R. and Cross, M. 1981 "Accurate Solutions of Moving Boundary Problems using the Enthalpy Method," Int. J. Heat Mass Transf., vol. 24, pp. 545–556.

Voller, V.R. and Prakash, C. 1987 "A Fixed Grid Numerical Modeling Methodology for Convection–Diffusion Mushy Region Phase Change Problems," Int. J. Heat Mass Transfer, vol. 30, 1709 – 1719.

Webb, B.W. and Hill, D.P. 1989 "High Rayleigh Number Laminar Natural Convection in an Asymmetrically Heated Vertical Channel," J. Heat Transfer, vol. 111, 649 – 656.

Wirth, R.A. and Stutzman, R.A. 1982 "Experiments on Free Convection between Vertical Plates with Symmetric Heating," J. Heat Transfer, vol. 104, 501 – 507.

Wright, J.A. and Shyy, W. 1992 "A Pressure-Based Composite Grid Method for the Incompressible Navier–Stokes Equations," J. Comp. Phys., vol. 107, 225–238.

Yeckel, A., Salinger, A. G. and Derby, J. J. 1995 "Theoretical Analysis and Design Considerations for Float–Zone Refinement of Electronic Grade Silicon Sheets," J. Crystal Growth, vol. 152, 51 – 64.

Young, G. W. 1990 "Float Zone Modeling: Transport Phenomena and Morphological Stability," Appl. Mech. Rev., vol. 43, 63 – 69.

Zebib, A., Homsy, G.M. and Meiburg, E. 1985 "High Marangoni Number Convection in a Square Cavity," Phys. Fluids A, vol. 28, 3467–3476.

Zhang, Y. and Alexander, J.I.D. 1992 "Surface Tension and Buoyancy Driven Flow in A Non–isothermal Liquid Bridge," Int. J. Numer. Meth. Engrg., vol. 14, 197–215.

BIOGRAPHICAL SKETCH

Madhukar M. Rao was born in Madras, India on October 12, 1966. He obtained his bachelor's degree in aerospace engineering at the Indian Institute of Technology, Madras, India in May 1988 and his master's degree in aerospace engineering at the University of Florida in May 1990. Since then he has been pursuing his Ph.D. in aerospace engineering, specializing in computational fluid dynamics, at the University of Florida.

I certify that I have read this study and that in my opinion it conforms to acceptable standards of scholarly presentation and is fully adequate, in scope and quality, as a dissertation for the degree of Doctor of Philosophy.

Wei Shyy

Wei Shyy, Chairperson
Professor of Aerospace Engineering,
Mechanics and Engineering Science

I certify that I have read this study and that in my opinion it conforms to acceptable standards of scholarly presentation and is fully adequate, in scope and quality, as a dissertation for the degree of Doctor of Philosophy.

Richard L. Fearn

Richard L. Fearn
Professor of Aerospace Engineering,
Mechanics and Engineering Science

I certify that I have read this study and that in my opinion it conforms to acceptable standards of scholarly presentation and is fully adequate, in scope and quality, as a dissertation for the degree of Doctor of Philosophy.

Ulrich Kurzweg

Ulrich H. Kurzweg
Professor of Aerospace Engineering,
Mechanics and Engineering Science

I certify that I have read this study and that in my opinion it conforms to acceptable standards of scholarly presentation and is fully adequate, in scope and quality, as a dissertation for the degree of Doctor of Philosophy.

E. Rune Lindgren
Professor of Aerospace Engineering,
Mechanics and Engineering Science

I certify that I have read this study and that in my opinion it conforms to acceptable standards of scholarly presentation and is fully adequate, in scope and quality, as a dissertation for the degree of Doctor of Philosophy.

Yogi Goswami
Professor of Mechanical Engineering

This dissertation was submitted to the Graduate Faculty of the College of Engineering and to the Graduate School and was accepted as partial fulfillment of the requirements for the degree of Doctor of Philosophy.

May 1996

fr

Winfred M. Phillips
Dean, College of Engineering

Karen A. Holbrook
Dean, Graduate School